Force chains, friction, and flow: Behavior of granular media across length scales

Thesis by

Ryan C. Hurley

In Partial Fulfillment of the Requirements

for the Degree of

Doctor of Philosophy

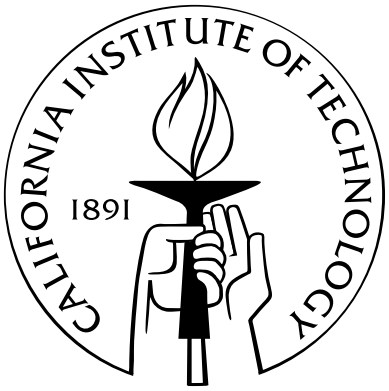

California Institute of Technology

Pasadena, California

2016

(Defended September 8, 2015)

Acknowledgements

I would like to thank my advisor, José Andrade, for the many lessons I have learned from him about being a successful faculty member. His excitement for science has motivated me throughout my time at Caltech. I hope to put his many lessons to use in the future. I would also like to thank the other members of my thesis committee – Kaushik Bhattacharya, Guruswami Ravichandran, and Michael Lamb – for invaluable conversations, feedback, and professional advice.

I would like to thank my fiancée, Margaret. Without her, I would be a different person today and this thesis would likely not exist.

I would like to thank all past and present members of the Computational Geomechanics Group at Caltech with whom I have shared the ups and downs of research: Keng-Wit Lim, Utkarsh Mital, Reid Kawamoto, Alex Jerves, Eloise Marteau, Daniel Arthur, Ivan Vlahinic, and Jason Marshall. I would also like to thank Stephen Hall of Lund University for allowing me to collaborate with him now and in the future. I consider this a great honor.

Finally, I would like to acknowledge the various funding agencies and projects that I have had the pleasure of providing research for: AFOSR (# FA9550-12-1-0091), DTRA (HDTRA1-12-1-0041), JPL ("Technologies for Increased Landing Accuracy, Payload Mass Fraction, and Landing Site Elevation"), and KISS ("xTerramechanics: Characterization and Modeling of Spacecraft-Regolith Interactions"). These projects and the great teams I have worked with have opened my eyes to new and exciting frontiers in science and engineering.

Abstract

We study the behavior of granular materials at three length scales. At the smallest length scale, the grain-scale, we study inter-particle forces and "force chains". Inter-particle forces are the natural building blocks of constitutive laws for granular materials. Force chains are a key signature of the heterogeneity of granular systems. Despite their fundamental importance for calibrating grain-scale numerical models and elucidating constitutive laws, inter-particle forces have not been fully quantified in natural granular materials. We present a numerical force inference technique for determining inter-particle forces from experimental data and apply the technique to two-dimensional and three-dimensional systems under quasi-static and dynamic load. These experiments validate the technique and provide insight into the quasi-static and dynamic behavior of granular materials.

At a larger length scale, the mesoscale, we study the emergent frictional behavior of a collection of grains. Properties of granular materials at this intermediate scale are crucial inputs for macro-scale continuum models. We derive friction laws for granular materials at the mesoscale by applying averaging techniques to grain-scale quantities. These laws portray the nature of steady-state frictional strength as a competition between steady-state dilation and grain-scale dissipation rates. The laws also directly link the rate of dilation to the non-steady-state frictional strength.

At the macro-scale, we investigate continuum modeling techniques capable of simulating the distinct solid-like, liquid-like, and gas-like behaviors exhibited by granular materials in a single computational domain. We propose a Smoothed Particle Hydrodynamics (SPH) approach for granular materials with a viscoplastic constitutive law. The constitutive law uses a rate-dependent and dilation-dependent friction law. We

provide a theoretical basis for a dilation-dependent friction law using similar analysis to that performed at the mesoscale. We provide several qualitative and quantitative validations of the technique and discuss ongoing work aiming to couple the granular flow with gas and fluid flows.

Contents

Acknowledgements **iii**

Abstract **iv**

1 Introduction **1**

1.1 Granular materials 1

1.2 Overview of thesis 3

1.3 Background on inter-particle forces 5

2 Extracting inter-particle forces in opaque granular materials: Beyond photoelasticity[1] **9**

2.1 Experimental validation and application of GEM 11

2.1.1 Experimental setup and procedure 11

2.1.2 Strain fields and force results 13

2.2 Governing equations 17

2.2.1 Equilibrium 18

2.2.2 Average particle stress 19

2.2.3 Cohesionless and tangential forces 20

2.2.4 Structure of equations and connection to experiments 22

2.3 Mathematical framework 23

2.3.1 Inverse problem formulation 23

2.3.2 Measurement noise and alternative formulation 25

[1] Adapted from R. Hurley, E. Marteau, G. Ravichandran, and J.E. Andrade. Extracting inter-particle forces in opaque granular materials: Beyond photoelasticity. *Journal of the Mechanics and Physics of Solids*, 63:154-166, 2014. DOI: 10.1016/j.jmps.2013.09.013

2.3.3 Implementation 26
2.4 Numerical example 26
2.4.1 Global force inference 27
2.4.2 Noise reduction 27
2.4.3 Local force inference 30
2.5 Conclusion 31

3 Dynamic inter-particle force inference in granular materials: Method and application[2] 32
3.1 Introduction 32
3.2 The method 33
3.2.1 Experimental measurements 33
3.2.2 Numerical optimization 34
3.3 Example 1: Validation 42
3.3.1 Experiment setup 42
3.3.2 Experiment analysis 44
3.3.3 Experiment results and FEM comparison 46
3.4 Example 2: Application 49
3.4.1 Experimental setup 49
3.4.2 Experiment analysis 50
3.4.3 Experimental results 50
3.5 Discussion 54
3.6 Conclusion 56

4 Friction in inertial granular flows: Competition between dilation and grain-scale dissipation rates[3] 58
4.1 Introduction 58

[2]Adapted from R.C. Hurley, K.W. Lim, G. Ravichandran, J.E. Andrade. Dynamic inter-particle force inference in granular materials: Method and application. *Experimental Mechanics*, 2015. DOI: 10.1007/s11340-015-0063-8

[3]Adapted from R.C. Hurley and J.E. Andrade. Friction in inertial granular flows: Competition between dilation and grain-scale dissipation rates. *Granular Matter*, 17(3)287-295, 2015. DOI: 10.1007/s10035-015-0564-2

4.2 The friction law for simple shear 61
4.3 Numerical simulations of simple shear 63
4.3.1 Description of code 64
4.3.2 Results: Validity of friction law 67
4.3.3 Results: Grain-scale dissipation mechanisms 68
4.3.4 Influence of material properties 69
4.3.5 Results: Dilation and dissipation rates 71
4.3.6 Results: Rate-dependent friction 73
4.4 Discussion 75
4.5 Conclusion 76

5 Modeling dilative viscoplastic granular flows using SPH[4] 77
5.1 Introduction 77
5.2 Balance and constitutive Laws 80
5.2.1 Balance law 80
5.2.2 Constitutive law 80
5.2.3 Theoretical link between friction and dilation rate 82
5.3 SPH formulation and algorithm 84
5.3.1 Kernel function and basic equations 84
5.3.2 Density 85
5.3.3 Equation of state 86
5.3.4 Equation of motion 87
5.3.5 Boundary conditions 88
5.3.6 Time integration 90
5.4 Examples 92
5.4.1 Example 1: Angle of repose 92
5.4.2 Example 2: Infinite inclined plane flow 96
5.4.3 Example 3: Granular column collapse 102
5.4.3.1 Scaling laws 102

[4]Adapted from R.C. Hurley and J.E. Andrade. Modeling dilative viscoplastic granular flows using SPH. *Under review.*

5.4.3.2 Reduced bulk modulus, friction angle, and resolution studies . . . 107
5.4.4 Example 4: Column collapse down inclined planes . . . 108
5.5 Discussion and conclusion . . . 115

6 Discussion and conclusion **117**
6.1 Summary . . . 117
6.2 Ongoing and future work . . . 118
6.2.1 Inter-particle force inference . . . 118
6.2.2 SPH modeling of coupled granular media and fluid flows . . . 119

Bibliography **124**

List of Figures

1.1 The three length scales studied in this thesis: the microscale, the mesoscale, and the macroscale. The respective quantities of interest at each scale include force chains, friction, and flow. 2

2.1 The GEM methodology for inter-particle force-inference presented in this paper. Experimental imaging techniques provide rich data sets for extracting intra-particle strain fields and material fabric. These ingredients are input into a mathematical framework which yields inter-particle forces by solving an appropriate inverse problem. Variables and equations in panel 3 are described in section 2.2. 10

2.2 Experimental setup: 1. CMOS camera ; 2. Canon lens ; 3. Digimeter ; 4. Loading device. 12

2.3 (a) Sample under macroscopic loading. Top face (red) was prescribed a vertical load of 215 N using a smooth, rigid wall. Bottom and lateral faces (blue) were smooth, stationary walls. (b) Results of segmentation process. 14

2.4 Sample dimensions in millimeters and information on the fabric: particle numbers, position of contact points and centroids. 15

2.5 Strain components ϵ_{xx}, ϵ_{yy} and ϵ_{xy} obtained from DIC. 16

2.6 Resulting inter-particle forces (in N) from application of GEM. 17

2.7 Illustration of particle-particle and particle-boundary contacts. 18

2.8 Unit vectors for contact i. 21

2.9 (a) Numerical odometric test setup. (b) Inter-particle forces computed with DEM and (2.13). Length scale in meters, forces in Newtons. Line thickness proportional to force magnitude. 28

2.10 (a) Solution to (2.13) with artificial noise, $\|\delta \boldsymbol{f}\| = 0.154$. (b) Solution to (2.14) with same noise, $\|\delta \boldsymbol{f}\| = 0.053$ (right). 29

2.11 Solution to (2.13) performed locally within granular material. 30

3.1 Illustration of various terms used in the governing equations. 35

3.2 Pareto front. 40

3.3 Experimental materials and setup. (a) Table setup with air duct connected to fan, rigid blocks fastened to table, camera and light source vertically over the area of interest. (b) Close-up view of table top and the top surface of a polyurethane disk with speckle pattern. (c) The underside of a polyurethane disk, showing plenum chamber for compressed air. (d) Experimental setup with 6 polyurethane disks and rigid impactor propelled at initial conditions $v_x = -1.141$m/s and $v_y = -0.66$m/s. Particle labels will be used later and are in no meaningful order. . . . 44

3.4 The ϵ_{xy} component of strain from (a) DIC and (b) FEM at four times during the impact event. All figures share a common scale. Strain values above and below the extreme values of the scale occur in small areas. 46

3.5 (a) Forces found using Eq. (3.18). Length and width of lines are proportional to force magnitude. (b) Forces found from the FEM model. (c) Eight contact point locations, chosen to include the major force chain and otherwise at random. (d) A comparison of force evolutions using Eq. (3.18) and the FEM model. 48

3.6 Experimental setup. (a) A window featuring a piece of Plexiglas and a sheet of PVC plastic holding the 2D granular bed in place. A high speed camera is used to view the granular bed as it is impacted by a steel intruder. (b) A close-up of the steel intruder about to impact the granular bed at -2.4m/s. 51

3.7 Inter-particle forces in the granular bed at six times during an impact event. 52

3.8 Inter-particle forces in the granular bed at six times during an impact event with an initial packing of the bed different from the experiment shown in Fig. 3.7. 53

3.9 The vertical force felt by the intruder for the experiments shown in Figs. 3.7 and 3.8. 54

3.10 Maximum inter-particle force as a function of distance from the surface of the intruder for three experiments with distinct initial packings. Exp. 1 refers to Fig. 3.7. Exp. 2 refers to Fig. 3.8. An inter-particle force is considered to be a distance $nd_{\min}$ from the surface of the intruder if the contact point that it belongs to falls within a range of $nd_{\min}$ and $(n+1)d_{\min}$ away from the surface of the intruder, where $d_{\min}$ is the minimum particle diameter in the granular bed, 2.54cm. 55

4.1 Friction encodes contact-scale and grain-scale information in a single parameter for continuum analysis. 59

4.2 The two timescales associated with the inertial number, $I = T_c/T_{\dot{\gamma}}$. . . 59

4.3 (a) A rendering of the simple shear flows featured in this paper. The top-most and bottom-most particles are used as rough boundaries. Colors indicate the magnitude of velocity, where v_x is the imposed wall velocity. (b) Coefficient of restitution e in a two-particle collision with normal velocity $v_c\sqrt{\rho_g/k_n}$ for data set 1 (- -) and data set 2 (-). 65

4.4 A comparison of (a) effective friction and (b) solid fraction from our simulations and available data sets taken from the literature. Blue squares are from contact dynamics simulations [1]. Black triangles are from 3D annular shear cell experiments [2, 3]. Error bars indicate standard deviations in time of measured quantities. The dashed line shows the fit $\mu = \mu_0 + (\mu_1 - \mu_0)/(1 + I_0/I)$ from [4]. 67

4.5 A comparison of the effective friction coefficient calculated from proposed friction relationship in Eq. (4.6) and the stress formula in Eq. (4.7). 68

4.6 (a) The two terms $\mu_n = Z\phi\langle\Gamma_n\rangle/(I\tilde{\Gamma})$ and $\mu_s = Z\phi\langle\Gamma_s\rangle/(I\tilde{\Gamma})$ in the additive decomposition of effective friction given in Eq. (4.9) for the primary data set (- -) labeled DS1 and the secondary data set (-) labeled DS2. (b) The total effective friction for the two data sets as a function of I. Error bars are omitted from inset plots for clarity. 70

4.7 (a) The coordination number Z as a function of inertial number. The dashed line is the fit from Eq. (4.10). (b) The solid fraction ϕ as a function of inertial number. The dashed line is the fit from Eq. (4.11). (c) The average grain-scale dissipation rates $\langle\Gamma_n\rangle/\tilde{\Gamma}$ and $\langle\Gamma_s\rangle/\tilde{\Gamma}$ as a function of inertial number. The dashed lines are power-law fits, with $\langle\Gamma_n\rangle/\tilde{\Gamma} \propto I^{2.4}$ and $\langle\Gamma_s\rangle/\tilde{\Gamma} \propto I^{1.87}$ (d) The quantity $Z\phi/I$ as a function of inertial number. The dashed lines represent the two regimes of behavior in which $Z\phi/I \propto I^{-1}$ and $Z\phi/I \propto I^{-2}$. Error bars in (d) are negligibly small. 72

4.8 The inset of Fig. 4.7c, showing the average grain-scale dissipation rates as a function of inertial number on a log-log scale. The dashed lines illustrate the scaling of each dissipation rate discussed in the text, as well as the scaling proportional to I at the transition to quasi-static flow. 74

5.1 (a) Illustration of the smoothing kernel W with compact support of radius $2h$ about particle a. (b) Interior particles interacting with boundary particles, which are given artificial velocity. 86

5.2 (a) Initial conditions of the slump test through an orifice. In color, blue represents internal SPH particles and red represents boundary particles. Length $l = 60$ cm, $h = 50$ cm, and the size of the simulated material in the z dimension is 6 cm. (b) Final collapsed side profile of the slump test through an orifice for $\phi = 30°$. The repose angle θ is measured in the middle 75% of the domain between the left wall and the orifice. (c) Results of the simulations with and without including β in the calculation of friction. The dashed line and circles represents the curve $\theta = \phi$. Results without β are blue squares which provide a lower bound to the $\theta = \phi$ curve. Results with β are red inverted triangles which nearly match the $\theta = \phi$ curve. (d) Pressure in the collapsed granular pile for $\phi = 30°$ showing a slight pressure drop in the layer of SPH particles directly above the bottom surface of the container. 94

5.3 (a) Initial conditions of a typical inclined plane flow experiment showing internal SPH particles above $y = 0$ and boundary particles at or below $y = 0$. (b) A typical velocity profile of an inclined plane flow. (c) Velocitiy profiles in the x direction as a function of height y in the granular material for simulations that do not include β in the calculation of friction. Symbols represent simulation results and dashed lines represent the best fit of the Bagnold profile (Eq. (5.30)) to the simulation data. (d) Same as (c) but for simulations that include β in the calculation of friction. 98

5.4 (a) Bulk acceleration $\dot{\bar{a}}$ of the granular material in the inclined plane simulations, without the use of β in the calculation of friction, as a function of time. The highest curve represents $\theta = 33°$ and each lower curve represents a reduction in θ by 3°. All accelerations appear to asymptote to zero except for $\theta = 33°$. The inset shows raw data overlaid with the same fits. (b) Same as (a) except for simulations that include β in the calculation of friction. (c) Slip velocity in simulations not including β in the calculation of friction, found by averaging the v_x velocity of the bottom-most layer of interior SPH particles. All slip velocities appear to asymptote to finite values except for $\theta = 33°$. (d) Same as (c) but for simulations that include β in the calculation of friction. 101

5.5 Typical initial conditions of the column collapse simulations for (a) grit and (b) fine glass. The right-most vertical wall in each figure is the containing wall that is deleted at $t = 0$. In the color figure, blue particles represent internal particles and red particles represent boundary particles. 104

5.6 (a) Scaling laws for collapsed height in simulations not using β in the calculation of friction. Symbols are SPH simulations and dashed lines are linear best-fit lines in logarithmic space for all data with x coordinate above 1.7. (b) Scaling laws for collapsed runout distance in simulations not using β in the calculation of friction. (c) Same as (a) but for simulations using β in the calculation of friction. (d) Same as (b) but for simulations using β in the calculation of friction. 106

5.7 Results of parametric studies of various model parameters on numerical results. (a) Result of varying the bulk modulus over two orders of magnitude does not indicate any significant change in results. This also justifies our use of $\kappa = 10^5$ in most simulations in this chapter to eliminate the shorter time step that may otherwise be needed to ensure stability. (b) Result of varying bulk and basal friction coefficients within the experimental error bars of [5] illustrates the expected changes, but only minor changes. (d) Results of mesh-refinement study illustrate the coarse mesh used throughout the chapter produces results that are nearly the same as the finest mesh. 109

5.8 (a) Initial and (b) final configurations for simulations of column collapse down inclined planes. The right-most near-vertical wall in (a) represents the containing wall that is lifted in the y direction with $v_x = 2$ m/s at $t = 0$. In the color figure, blue particles represent interior particles and red particles represent boundary particles. 110

5.9 Time-dependent collapse profiles down inclined planes for four inclination angles: $\theta = 0°, 10°, 16°$, and $22°$. Symbols represent SPH profiles and lines represent experimental profiles from [6]. (a) and (b) illustrate results with periodic boundary conditions in the z direction and no sidewalls. (c) and (d) illustrate results with sidewalls. (a) and (c) show results for simulations not including β in the calculation of friction. (b) and (d) show results for simulations including β in the calculation of friction. 113

5.10 Snapshots of simulations shown in Fig. 5.9d for (a) $\theta = 0°$, (b) $\theta = 10°$, (c) $\theta = 16°$ and (d) $\theta = 22°$. These simulations employ β in the calculation of friction. In the color figure, the color of each particle corresponds to the magnitude of the strain rate tensor $\boldsymbol{D}$. We clearly see the influence of sidewalls (not rendered) at the first nonzero time for each inclination angle. At these times, particles appear to undergo a higher strain rate in the foreground and background than in the center of the flow. 114

6.1 (a) Macroscopic load curve for oedeometric compression of single-crystal quartz grains. (b) Sample volumetric image of the assembly obtained with XRCT during the load cycle. (c) Preliminary results of force inference using Eq. (3.19) applied to a single load step. Lines connect contacting grain centroids and are darkened and thickened linearly with force magnitude. 120

6.2 Qualitative example of gas-driven soil erosion modeled using the SPH framework. The left column of figures illustrates the sand response only in the first 75 ms of the gas impingement event. The right column of images illustrates the gas response only. 123

Chapter 1

Introduction

1.1 Granular materials

Granular materials are materials composed of discrete macroscopic particles with size greater than 1 micron [7]. Snow flakes, sand, soil, rice, pharmaceutical pills, and even asteroids can be considered granular. These materials are ubiquitous in our universe and their behavior plays a crucial role in natural and engineered processes such as erosion, mining, pharmaceutical processing, material transport, and food production [8]. Unlike gases and liquids, the mechanical behavior of granular materials is governed by nonlinear inter-particle interactions rather than thermal fluctuations [7]. Furthermore, the lack of scale separation in these materials for many problems of interest prohibits development of a single governing mathematical framework (e.g., Naiver-Stokes) [7, 8, 9]. Thus, despite their ubiquity, granular materials possess a complexity that necessitates a unique multi-scale approach.

This thesis examines the behavior of granular materials at three length scales: the grain-scale, the mesoscale, and the macro-scale. These three scales and the behaviors of interest that will be studied are illustrated graphically in Fig. 1.1. At the grain-scale, we study inter-particle forces and "force chains". These unique features are natural building blocks of constitutive laws for granular materials and frequently manifest themselves in macroscopically observable phenomena. At the mesoscale, we study emergent frictional behavior of a collection of flowing grains. The effective frictional strength of granular materials plays a governing role in mechanical and

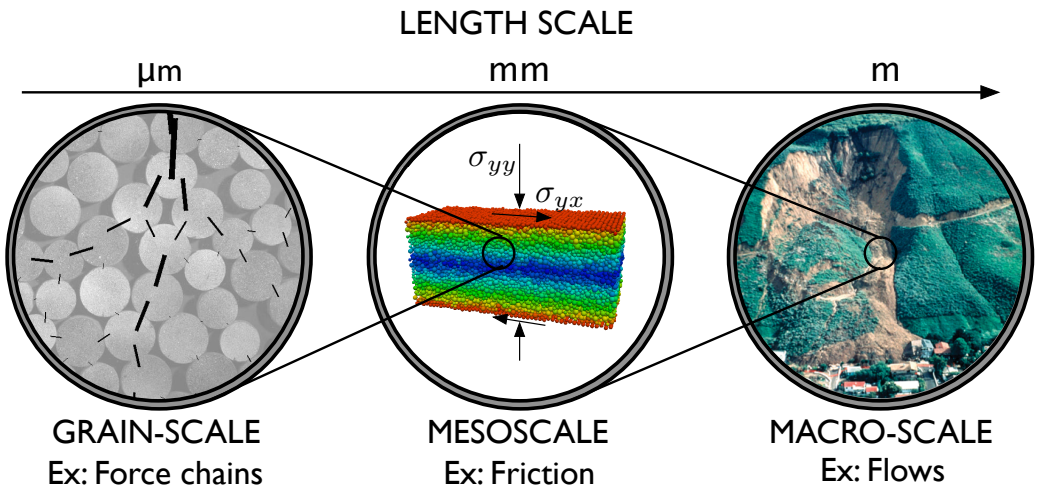

Figure 1.1: The three length scales studied in this thesis: the microscale, the mesoscale, and the macroscale. The respective quantities of interest at each scale include force chains, friction, and flow.

dynamical behavior, both in quasi-static and dynamic events. At the macro-scale, we investigate continuum modeling techniques for capturing the distinct solid-like, fluid-like, and gas-like behaviors exhibited by granular materials. Full-field numerical methods capable of capturing these phases are essential for predicting and understanding the processes underlying the behavior of granular media in nature and industry.

The three scales and topics discussed in this thesis are connected in a manner that highlights the multi-scale nature of granular materials. For instance, the mesoscale effective friction coefficient and the macro-scale stress tensor can be derived from inter-particle forces and grain kinematics (e.g., see [1,10,11,12]). Force chains arising from grain-scale interactions may also induce nonlocal behavior that is widely observed at meso- and macro-scales in number of flow configuration (e.g., see [90]). An improved understanding of force chain dynamics and nonlocal constitutive theories like those discussed in [90] may therefore provide new insight into the multi-scale physics of granular media. Furthermore, mesoscale properties such as effective friction play an important role in solid-like, fluid-like, and gas-like behavior and transitions at the macro-scale. An improved understanding of these properties and new full-field

modeling tools may help elucidate macro-scale behavior in insightful ways.

Despite the stated connections between the scales studied in this thesis, we do not focus heavily on investigating these connections. Rather, we primarily develop technologies for studying each scale and leave extensive investigation of connections for future work. The lack of rigorous theories connecting scales is an ongoing challenge in the field of granular materials. We hope that the technologies advanced in the present work aid researchers in overcoming this challenge in the future.

Throughout this thesis, we do not focus on a particular type of granular material. Instead, many of the results are generally applicable to any conglomeration of particulates. This practice of seeking results generalizable to many particulate systems when studying granular media has a history of elucidating the behavior of many similar systems: foams, colloids, emulsions, and suspensions [9]. However, we often make reference to sands and cohesionless soils in an attempt to understand these most basic yet fundamental examples of granular media.

1.2 Overview of thesis

The layout of this thesis is as follows. Chapters 2, 3, and 4 are adapted from published journal articles. Chapter 5 is adapted from a journal article currently undergoing peer-review. Most of the content of these four chapters is reproduced directly (with permission of the publishers) in order to preserve their stand-alone quality. The titles for these chapters are also the same as the journal articles they represent. However, the introduction sections of chapters 2 and 3 are modified heavily. Rather than presenting the original article introductions in those chapters, we consolidate background information in section 1.3 to eliminate redundancies. We then dedicate the introduction sections of these chapters to briefly outlining the research they will describe. The introduction sections of chapters 4 and 5 are mostly unmodified to provide a more seamless reading experience. However, we provide a brief overview of these chapters, as well as chapters 2 and 3, in the remainder of section 1.2.

Chapter 2, adapted from a paper appearing in the Journal of the Mechanics and

Physics of Solids [13], describes a technique for inferring inter-particle forces in quasi-static experiments on granular materials. The force inference technique involves numerically solving an optimization problem using experimental measurements of grain positions, grain contact points, and volume-averaged grain stresses as input. The technique is applicable to opaque, arbitrarily shaped grains, and makes no assumption of contact or constitutive law for the grain material. However, the technique requires that grains are deformable and that deformations can be measured experimentally. We present the numerical framework, discuss its solution space, and provide two examples of application to real and synthetic experimental data.

Chapter 3, adapted from a paper appearing in Experimental Mechanics [14], extends the force inference technique introduced in chapter 2 to dynamic experiments. The extended technique involves augmented governing equations to accommodate dynamic effects and a modified multi-objective optimization problem. We validate this dynamic technique by comparing results of force inference applied to an impact experiment with an Abaqus/Explicit simulation of the same boundary value problem. We also present a study of force chains in impacted granular beds that illustrates the link between force chains and intruder dynamics. The study also highlights an apparent limit to force chain length that occurs at identical impact velocities for different initial bed packings.

Chapter 4, adapted from a paper appearing in Granular Matter [10], provides a derivation of a new friction law for steady-state granular flows. This friction law analytically relates friction to shear rate, coordination number, porosity, and average grain-scale dissipation rates. The friction law illustrates that rate-dependent friction in steady-state flows arises from a delicate competition between material dilation and grain-scale dissipation rates. We perform numerical simulations to investigate this competition and illustrate how different grain-scale dissipation mechanisms are responsible for the macroscopic friction coefficient in granular shear flows. The reader is directed to an additional paper appearing in Procedia Engineering [15] that extends this friction law to the non-steady-state regime and briefly discusses numerical simulations.

Chapter 5, adapted from a journal manuscript currently undergoing peer-review, discusses a continuum modeling technique for granular flows. The technique combines a mesh-free Smoothed Particle Hydrodynamics (SPH) framework with a viscoplastic constitutive law that contains a rate- and dilation-dependent friction law. The friction law is derived in a similar manner to those found in chapter 4, but from the governing equations of continuum mechanics. Several examples illustrate the ability of this method to reproduce realistic angles of repose in slump tests, to match the Bagnold velocity profile in infinite inclined plane flows, to produce accurate scaling laws for runout and final height of granular column collapses on flat surfaces, and to generate time-dependent profiles of granular columns collapsing down inclined planes that agree with experimental results.

Chapter 6 offers concluding remarks and briefly highlights ongoing and future work related to the topics covered in each chapter. In particular, we briefly discuss ongoing force inference experiments on single-crystal quartz grains imaged using x-ray computed tomography and x-ray diffraction. These experiments are a continuation of the work in chapters 2 and 3 and represent an important step toward understanding force transmission in real materials and calibrating more complex grain-scale models. We also discuss an ongoing effort to extend the SPH framework discussed in chapter 5 to modeling granular materials coupled with gas and fluid flows.

1.3 Background on inter-particle forces

Many studies have investigated analytical or empirical links between grain-scale and macro-scale properties of granular media. For instance, researchers have experimentally linked the so-called "fabric" of granular materials (i.e. the directional distribution of grain contact points) to the mobilized stress ratio and secant modulus [16]. Other researchers have developed methods of coarse-graining inter-particle forces and contact point locations for the macro-scale stress tensor [17]. Several researchers have derived analytical relationships between the mobilized angle of friction of a granular material and the radial distribution of inter-particle contacts and forces [1, 12, 18].

The length and dynamics of force chains has been shown to play an important role in macro-scale behaviors such as intruder penetration [43]. Force chains may also play an important role in inducing long-range communication in granular media, a behavior captured by recent nonlocal constitutive laws (e.g., see [90]). Several studies have examined the collective statistical properties and heterogeneity of inter-particle forces in quasi-static and dynamic settings [11,19,20,21,22,23,24,24,25,26,27,28,29,30,31,32]). These studies have proven useful in unlocking the tools of statistical physics for granular media, although significant progress remains to be made before a unifying framework exists for granular materials as it does for gases. One important milestone in developing this framework and understanding granular media has been the advent of grain-scale numerical techniques.

Grain-scale numerical models provide a platform for simulating the behavior of individual particles in a granular material. The Discrete Element Method (DEM) represents the seminal work on grain-scale numerical modeling [33]. DEM uses Newton's second law and linear or Hertzian contact laws to explicitly integrate the equations of motion of individual particles. Contact dynamics has also been introduced as an alternative implicit approach [34,35]. In the past two decades, numerous studies have employed these modeling techniques to further investigate links between grain-scale features such as forces and macro-scale behavior (e.g., see [27,36,37]). As these techniques evolve to handle complex grain shapes (e.g., see [38,39]) and are increasingly exploited to study inter-particle forces and other grain-scale behavior, it is important to validate their results using experimental data.

Experimental measurements of inter-particle forces in model granular materials has historically been accomplished using photoelasticity [21,40,41]). While photoelasticity has proven immensely useful, it has several restrictions. First, photoelasticity is limited to quasi-two-dimensional experiments on birefringent grains. Second, inversion techniques used to determine inter-particle forces from photoelasticity data require grains to remain elastic. Finally, photoelasticity poorly resolves the dynamic evolution of inter-particle forces at the grain-scale, instead providing forces averaged over tens or hundreds of grains (e.g., see [42,43]).

To overcome the elasticity restriction of photoelasticity, some researchers have laboriously reconstructed individual contact forces by matching experimentally observed fringe patterns to those generated from explicit simulations (see [44]). However, this technique is cumbersome and unrealistic for packings of more than a few grains. To overcome the two-dimensional restriction of photoelasticity, several researchers have studied force transmission in liquid droplets and gel packings (e.g., see [45, 46, 47]). However, these studies assume a Hertz contact law *a priori* and therefore cannot validate inter-particle forces found in grain-scale numerical models that also employ a Hertz contact formulation.

In chapters 2 and 3 of this thesis, we discuss a new force inference technique that overcomes the limitations of methods employed in the past. In particular, the new force inference technique is applicable to two- and three-dimensional particle packings, is not restricted to material linearity or elasticity, makes no assumption of contact law, and provides individual inter-particle forces during both quasi-static and dynamic events. The basic equations for this force inference technique were originally derived for quasi-static particle packings in [48]. However, [48] employed an incorrect numerical technique for obtaining inter-particle forces and did not provide experimental examples. Chapter 2 (adapted from [13]) provides a new presentation of the governing equations and a new numerical inverse problem relying on a constrained optimization approach for obtaining inter-particle forces. This chapter also includes the first experimental example of applying the force inference technique to an indeterminate packing of rubber cylinders. Chapter 3 (adapted from [14]) provides a new derivation of the governing equations for dynamic events and a modified multi-objective optimization approach for obtaining inter-particle forces. The dynamic form is validated experimentally and used to study inter-particle forces beneath an intruder impacting a granular bed. Chapters 4 and 5 address different topics, as discussed above and in their respective introduction sections.

In chapter 6, we provide a brief discussion of ongoing and future work on the force inference technique. The ongoing work includes inferring forces in opaque three-dimensional single-crystal quartz grains imaged using combined x-ray computed to-

mography and x-ray diffraction. This work represents the first time inter-particle forces have been inferred within the bulk of an opaque indeterminately-packed sand-like granular material.

Chapter 2

Extracting inter-particle forces in opaque granular materials: Beyond photoelasticity[1]

This chapter presents the first example of inter-particle force inference in real granular materials using an improved version of the methodology known as the Granular Element Method (GEM). GEM combines experimental imaging techniques with equations governing particle behavior to allow force inference in cohesionless materials with grains of arbitrary shape, texture, and opacity. This novel capability serves as a useful tool for experimentally characterizing granular materials, and provides a new means for investigating force networks. In addition to an experimental example, this chapter presents a precise mathematical formulation of the inverse problem involving the governing equations and illustrates solution strategies.

The Granular Element Method (GEM) presented in this chapter is an extended form of the method originally proposed in [48]. The contribution of this chapter is to present an experimental validation of GEM and a precise mathematical formulation of the proposed inverse problem involving the governing equations for particle mechanics. This paper also provides an additional inverse problem formulation that may help practitioners reduce solution error when experimental noise is present.

The GEM methodology can be visualized in Figure 2.1. Experimental imaging

[1]Adapted from R. Hurley, E. Marteau, G. Ravichandran, and J.E. Andrade. Extracting inter-particle forces in opaque granular materials: Beyond photoelasticity. *Journal of the Mechanics and Physics of Solids*, 63:154-166, 2014. DOI: 10.1016/j.jmps.2013.09.013

techniques such as high-resolution photography, 3D X-ray diffraction [49, 50, 51], and X-ray computed tomography (XRCT) [52, 53, 54] provide rich data sets from which Digital Image Correction (DIC) [55], level-set methods [56], and other techniques can extract intra-particle strain fields and material fabric (contact locations and normals). Intra-particle strains fields and material fabric are used as input into a mathematical framework which yields intra-particle stress fields using an appropriate constitutive relation and numerically solves an inverse problem using the governing equations of particle statics. The result of the inverse problem is inter-particle forces, a key component in the development of theories regarding granular material behavior. Because GEM can be coupled with any experimental techniques capable of extracting strain fields and fabric, recent advances in imaging (e.g., [49, 50]) will soon allow inference of inter-particle forces in natural materials with small grains, such as sands.

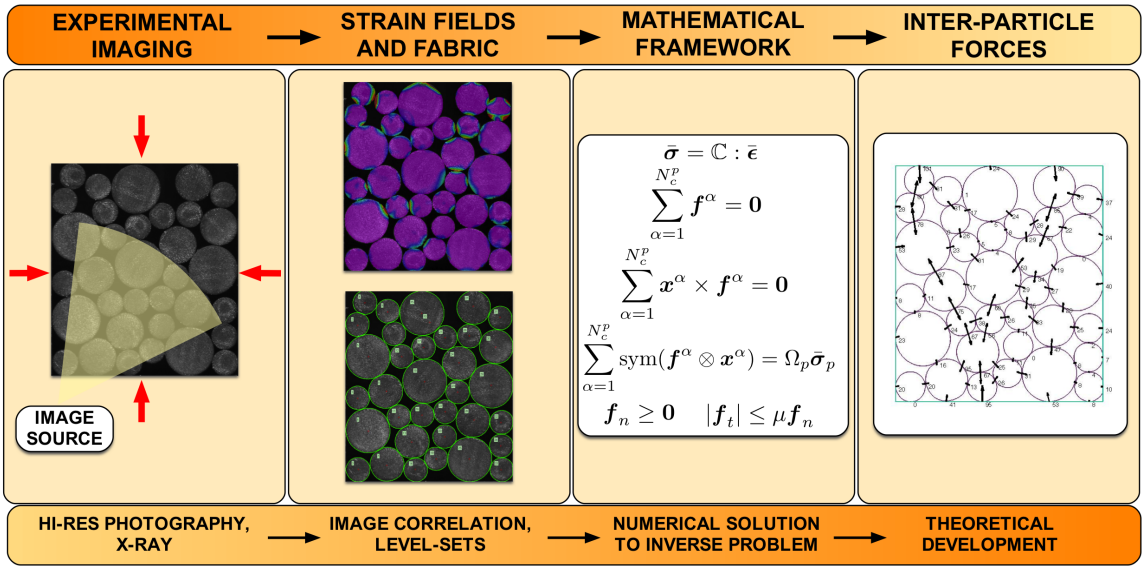

Figure 2.1: The GEM methodology for inter-particle force-inference presented in this paper. Experimental imaging techniques provide rich data sets for extracting intra-particle strain fields and material fabric. These ingredients are input into a mathematical framework which yields inter-particle forces by solving an appropriate inverse problem. Variables and equations in panel 3 are described in section 2.2.

The layout of this chapter is as follows. Section 2.1 presents an example of the

methodology applied to a real experiment involving rubber particles, showcasing the applicability of the method to real materials of any texture and its adaptability to a number of experimental imaging and algorithmic data analysis techniques. Sections 2.2 and 2.3 detail the ingredients of the mathematical framework of GEM. Section 2.4 illustrates additional features of GEM with a numerical example. Finally, section 2.5 offers concluding remarks.

The notation and terminology used in this chapter are defined as follows: $\mathbb{R}^{m\times n}$ denotes the set of real matrices with m rows and n columns, "$\cdot$" denotes an inner product (e.g., $\boldsymbol{a}\cdot\boldsymbol{b} = a_i b_i$; $\boldsymbol{c}\cdot\boldsymbol{d} = c_{ij}d_{jk}$), "$\otimes$" denotes a dyadic product (e.g., $\boldsymbol{a}\otimes\boldsymbol{b} = a_i b_j$), $\|\cdot\|_2$ denotes the Euclidian norm of a vector (e.g., $\|\boldsymbol{a}\|_2 = \sqrt{a_1^2 + ... + a_n^2}$), and "sym" is the symmetric operator defined as $\text{sym}(\cdot) = 1/2((\cdot) + (\cdot)^T)$. $\mathcal{R}(\boldsymbol{A})$ refers to the range of $\boldsymbol{A}$, the set of all possible linear combinations of the columns of $\boldsymbol{A}$. $\mathcal{N}(\boldsymbol{A})$ refers to the nullspace of $\boldsymbol{A}$, the set of all vectors $\boldsymbol{z}$ such that $\boldsymbol{A}\boldsymbol{z} = \boldsymbol{0}$.

2.1 Experimental validation and application of GEM

This section presents an example of GEM applied to a real experiment. The current experiment uses Digital Image Correlation (DIC) to measure full-field particle strains from which stresses are deduced. Information about the location of contact points and particle shapes is obtained from digital images using segmentation algorithms. This data is then passed to the GEM algorithm, which reconstructs the force distribution. The results of this experiment showcase the applicability of GEM to real materials and its potential to be combined with advanced experimental techniques.

2.1.1 Experimental setup and procedure

The experimental setup is shown in Figure 2.2. A CMOS camera with a 3.0 megapixel sensor (PL-B623, PixeLINK, Ottawa, Canada) and a Canon lens was used at a working distance of 20 cm to image the assembly. A specifically designed loading device is used to apply axial compression on the specimen, as shown in Figure 2.2. The specimen is placed between four faces: the bottom and lateral faces are stationary

and the top face can move vertically. The applied force was carefully measured with a 500 g load cell (LCFA-50G, Omega, Stamford, CT) and monitored with a digimeter (MD-40, Newport, Irvine, CA).

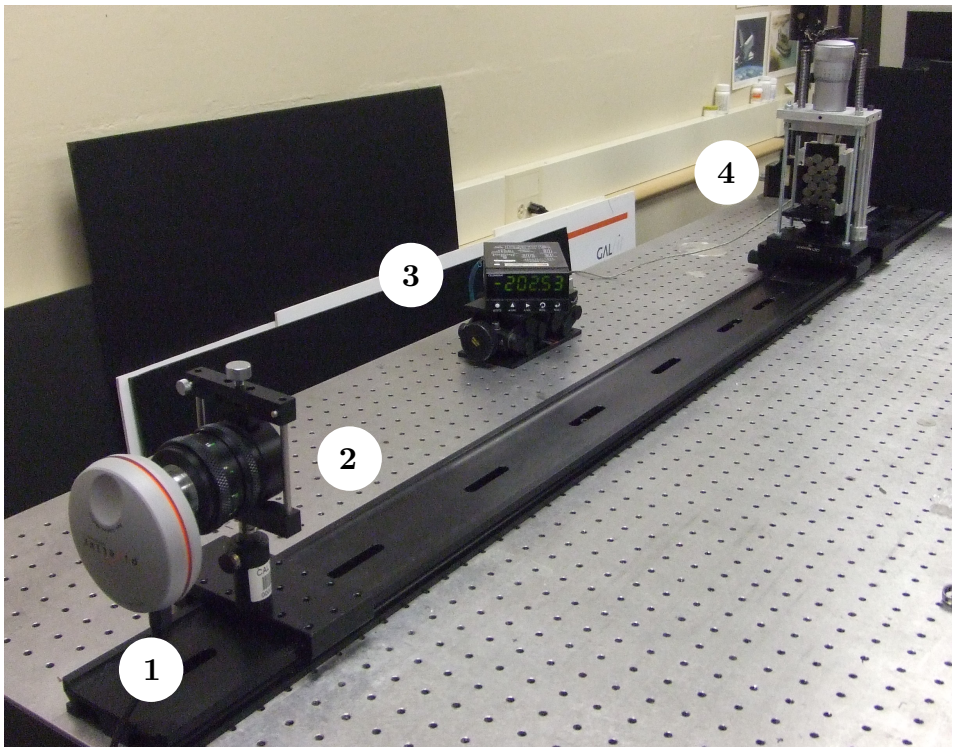

Figure 2.2: Experimental setup: 1. CMOS camera ; 2. Canon lens ; 3. Digimeter ; 4. Loading device.

The specimen used in the experiment was composed of rubber cylindrical grains. Grain diameters were 7 mm, 10 mm, or 14 mm, and the grains' out-of-plane length was 20 mm. The grains' Young's modulus was 5.5 MPa and Poisson's ratio was approximately 0.5. The specimen shown in Figure 2.3 was compressed with a 215 N vertical load on the top wall, while the side walls were held rigid.

The software VIC-2D was used to perform Digital Image Correlation (DIC) on the images in order to determine in plane full-field strain [57, 58]. Digital Image Correlation (DIC) is an optical tool based on digital image processing and numerical computing which provides full-field displacements and strains by comparing the gray intensity changes of the object surface before and after deformation [55, 59]. The DIC

procedure consists of tracking the same pixels between reference and deformed images. To perform this tracking, a correlation window, or subset, is chosen and deformed until the pattern in the deformed image matches the pattern in the reference image as closely as possible. To determine an adequate subset size, a compromise between resolution and measurement error needs to be found. The measurement error is evaluated by correlating two subsequent images of the specimen without applying any deformation. The values of the resulting strain components ($\epsilon_{xx}, \epsilon_{yy}$ and ϵ_{xy}) for different subset sizes are then compared in order to identify suitable configurations. The degree of similarity between the reference and deformed subsets is computed using a correlation coefficient and the best fit is achieved when the correlation coefficient reaches its maximum. The position of the deformed subset is determined and the in-plane displacement is obtained by calculating the difference between the position of each point in the reference subset and the position of the corresponding point in the deformed subset. The strain field is then computed by numerical differentiation of the displacement field.

Segmentation algorithms were used to extract the material's fabric: particle contact points, centroids and areas. In particular, a circular Hough transform [60,61] was first performed to determine the number of particles N_p and approximate positions of centroids and maximum radii, followed by a snake, or active contour model algorithm [62,63] to determine the true contours of the grain. The different parameters of the Hough transform and active contour model algorithm are manually adjusted by visual inspection of the resulting segmentation of the grains. Segmentation is finally achieved by partitioning the digital images into sets of pixels, each set constituting different particles. The result of this segmentation procedure is shown in Figure 2.3.

2.1.2 Strain fields and force results

The contact locations, particle areas, and average particle strain were used as input into GEM's mathematical framework to be described in Sections 2.2 and 2.2.

A simple algorithm was used to determine the position of the contact points.

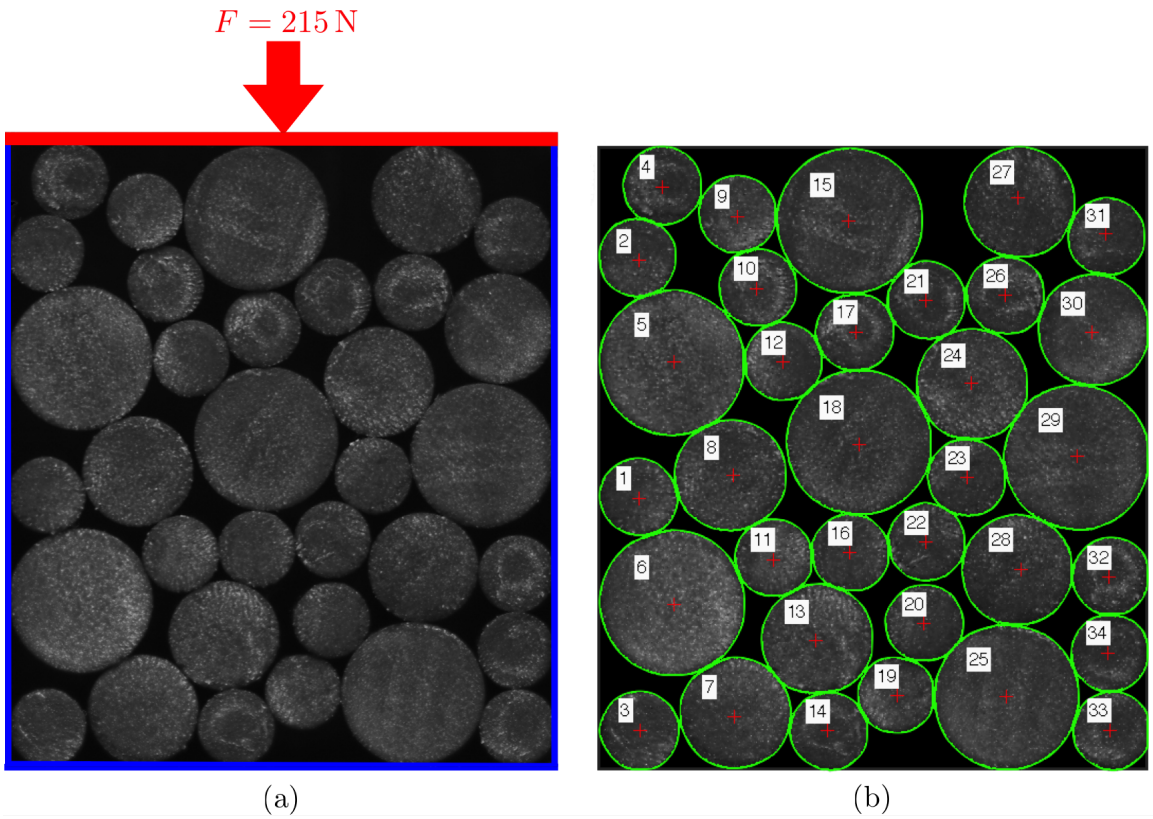

(a) (b)

Figure 2.3: (a) Sample under macroscopic loading. Top face (red) was prescribed a vertical load of 215 N using a smooth, rigid wall. Bottom and lateral faces (blue) were smooth, stationary walls. (b) Results of segmentation process.

First, grain boundaries were delineated as shown in Figure 2.3. Next, the euclidean distance between pixels on two adjacent boundaries was calculated and the two pixels were considered to belong to a contact surface if this distance was less than or equal to a certain pixel threshold L_{pix}. Finally, the average value of positions of all pixels belonging to a contact surface was used to determine a single coordinate (x, y) of the true contact point. The results of this algorithm are shown in Figure 2.4, where it can be seen that the 34 particles share a total of 78 contact points.

Figure 2.5 shows the full-field strain distribution obtained from DIC. The DIC procedure was applied grain by grain. For each grain, the subset size was manually chosen in order to achieve a reliable correlation analysis. The full-field strain distribution was obtained by calculating values of ϵ_{xx}, ϵ_{yy} and ϵ_{xy} inside of each particle

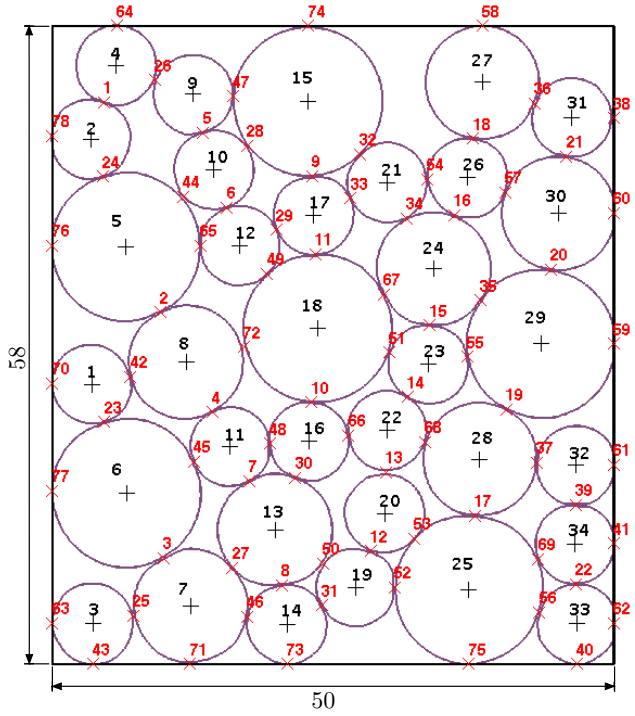

Figure 2.4: Sample dimensions in millimeters and information on the fabric: particle numbers, position of contact points and centroids.

using numerical differentiation of the displacement field. The average strain tensor, $\bar{\epsilon}^p$, was obtained by taking the arithmetic average of each tensor computed within a given particle. The average stress $\bar{\sigma}^p$ of a particle was deduced from the average strain $\bar{\epsilon}^p$ using generalized Hooke's law, $\bar{\sigma}^p = \mathbf{c} : \bar{\epsilon}^p$, where $\bar{\sigma}^p$ is the average elastic stress tensor at a particle and $\mathbf{c}$ is the elastic stiffness tensor of the particle. The Young's modulus and Poisson's ratio used in the elastic stiffness tensor were determined using a separate experiment on a single grain.

Using average particle strain and and fabric information, the regularized inverse problem in equation (2.14) was solved with a regularization parameter of $\lambda = 0.0024$. The resulting inter-particle forces are shown in Figure 2.6. It should be emphasized that the presented forces are forces distributed over the length of the cylinder. Figure 2.6 offers the first look at inter-particle forces inferred in a real, opaque material using GEM. The forces form expected patterns of force chains throughout the material. The particle-boundary forces along the top platen were measured by the load

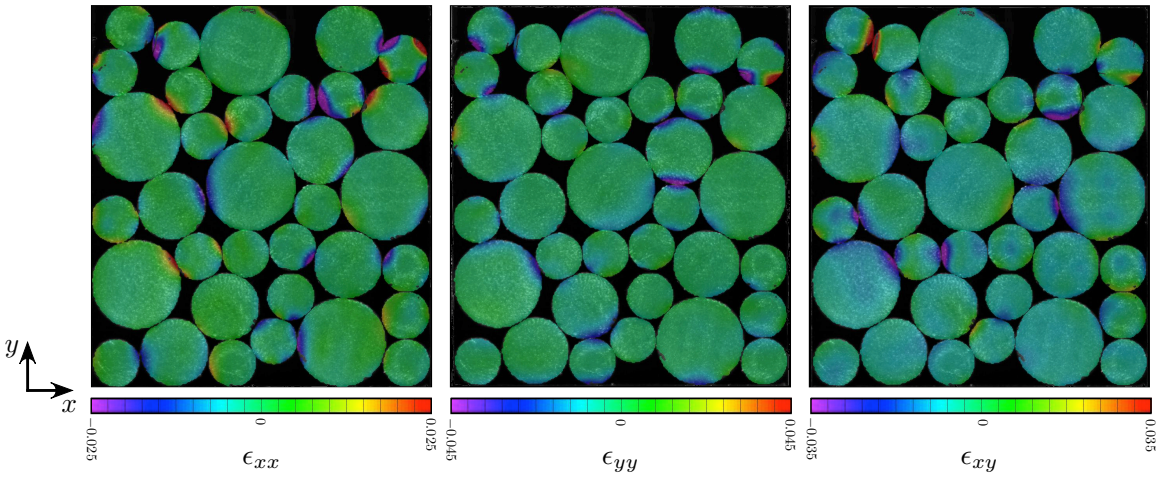

Figure 2.5: Strain components ϵ_{xx}, ϵ_{yy} and ϵ_{xy} obtained from DIC.

cell to be 215 N and the calculated resultant forces sum to 215 N.

The average macroscopic stress in the array was also computed using the expression [17]:

$$\langle \boldsymbol{\sigma} \rangle = \frac{1}{\Omega} \sum_{\alpha=1}^{N_c} \mathrm{sym}(\boldsymbol{f}^\alpha \otimes \boldsymbol{d}^\alpha) \tag{2.1}$$

where Ω is the volume of the assembly, N_c is the number of inter-particle contacts in the assembly, $\langle \boldsymbol{\sigma} \rangle$ is the macroscopic average stress, $\boldsymbol{f}^\alpha$ is the inter-particle contact force, and $\boldsymbol{d}^\alpha$ is the branch vector between particles. The resulting macroscopic stress was computed to be:

$$\langle \boldsymbol{\sigma} \rangle = \begin{bmatrix} -2.56 & 0.26 \\ 0.26 & -4.42 \end{bmatrix} \text{(kPa)} \tag{2.2}$$

where compressional stresses are negative. The $\langle \boldsymbol{\sigma} \rangle_{22}$ component of this result corresponds well with the applied stress of $-215\text{N}/0.05\text{m} = -4.3\,\text{kPa}$, a motivational result considering that equation (2.1) is approximate since branch vectors between particles and walls were not included.

The result of this experiment underscores the power of GEM for inferring inter-particle forces in real opaque materials. The experiment also illustrates the versatility of GEM: it is adaptable to any experimental technique able to furnish the required

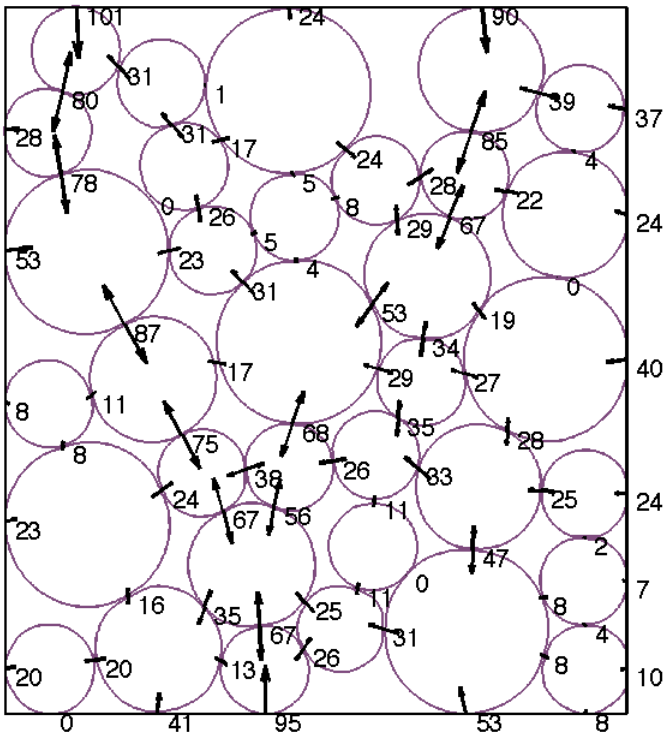

Figure 2.6: Resulting inter-particle forces (in N) from application of GEM.

input. The following sections describe GEM's mathematical framework in more detail and describe precisely how the required ingredients are used to produce inter-particle force estimates.

2.2 Governing equations

This section describes the equations governing particle behavior in cohesionless granular materials in static equilibrium. Underlying the formulation of all governing equations is the assumption of point contact. This assumption is valid for many stiff particles of interest in granular physics, including, for instance, sands, powders, and many pharmaceuticals. In the case of more compliant particles, this approximation may remain accurate for moderate load levels.

2.2.1 Equilibrium

Consider the p^{th} particle in a static granular material, interacting with other particles through N_c^p contact points labeled with index α (see Figure 2.7). Balance of forces and moments yields the two equilibrium equations:

$$\sum_{\alpha=1}^{N_c^p} \boldsymbol{f}^\alpha = \mathbf{0} \tag{2.3}$$

$$\sum_{\alpha=1}^{N_c^p} \boldsymbol{x}^\alpha \times \boldsymbol{f}^\alpha = \mathbf{0} \tag{2.4}$$

where $\boldsymbol{x}^\alpha$ is a vector from a conveniently chosen origin to the contact point α, and $\boldsymbol{f}^\alpha$ is a force vector acting at α.

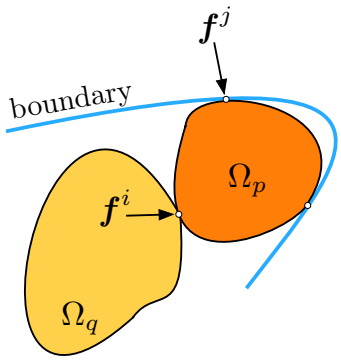

Figure 2.7: Illustration of particle-particle and particle-boundary contacts.

Equations (2.3) and (2.4) can be combined into a single matrix expression for an entire assembly of particles: $\boldsymbol{K}_{eq}\boldsymbol{f} = \mathbf{0}$. In two dimensions, the system takes the

form:

$$\underbrace{\begin{array}{c} \\ p \\ \\ q \\ \\ \end{array}\begin{array}{c} \begin{array}{ccccc} & i & & j & \end{array} \\ \begin{pmatrix} \ddots & \mathbf{0} & \cdots & \mathbf{0} & \cdots \\ \mathbf{0} & \boldsymbol{K}^i_{eq} & \mathbf{0} & \boldsymbol{K}^j_{eq} & \mathbf{0} \\ \vdots & \mathbf{0} & \ddots & \mathbf{0} & \vdots \\ \mathbf{0} & -\boldsymbol{K}^i_{eq} & \mathbf{0} & \mathbf{0} & \mathbf{0} \\ \vdots & \mathbf{0} & \vdots & \mathbf{0} & \ddots \end{pmatrix} \end{array}}_{\boldsymbol{K}_{eq}} \underbrace{\begin{pmatrix} \vdots \\ \boldsymbol{f}^i \\ \vdots \\ \boldsymbol{f}^j \\ \vdots \end{pmatrix}}_{\boldsymbol{f}} = \underbrace{\begin{pmatrix} \vdots \\ \mathbf{0} \\ \vdots \\ \mathbf{0} \\ \vdots \end{pmatrix}}_{\boldsymbol{b}_{eq}} \tag{2.5}$$

where

$$\boldsymbol{K}^i_{eq} = \begin{bmatrix} 1 & 0 \\ 0 & 1 \\ -x^i_2 & x^i_1 \end{bmatrix}; \quad \boldsymbol{f}^i = \begin{pmatrix} f^i_1 \\ f^i_2 \end{pmatrix}$$

and where p and q represent particles, i and j represent particle-particle and particle-boundary contacts as shown in Figure 2.7.

The extension to three dimensions is straightforward and omitted for brevity. In general, $\boldsymbol{K}_{eq}$ will have $dN_p(d+1)/2$ rows and dN_c columns where d is the dimension (e.g., $d = 2$ for 2D), N_p is the total number of particles in the assembly, and N_c is the total number of contact points in the assembly.

2.2.2 Average particle stress

The average Cauchy stress for a particle in equilibrium under the action of discrete boundary forces can be derived by considering the volume averaged stress equation for a particle p:

$$\bar{\boldsymbol{\sigma}}^p = \frac{1}{\Omega_p} \int_{\Omega_p} \boldsymbol{\sigma}^{\boldsymbol{p}} \, \mathrm{d}v \tag{2.6}$$

where Ω_p indicates integration over the deformed volume (in 3D) or area (in 2D) of the particle p. By considering balance of linear momentum, the divergence theorem, and the symmetry of the Cauchy stress tensor, this expression takes the form (see [48]

for more details):

$$\bar{\boldsymbol{\sigma}}^p = \frac{1}{\Omega_p} \sum_{\alpha=1}^{N_c^p} \mathrm{sym}(\boldsymbol{f}^\alpha \otimes \boldsymbol{x}^\alpha) \tag{2.7}$$

Equation (2.7) can be written in matrix form for an entire assembly of particles as $\boldsymbol{K}_{st}\boldsymbol{f} = \boldsymbol{b}_{st}$. In two dimensions, the system takes the form:

$$\underbrace{\begin{array}{c} \\ p \\ \\ q \\ \\ \end{array}\!\!\begin{array}{c} \begin{array}{ccccc} & i & & j & \end{array} \\ \begin{pmatrix} \ddots & \mathbf{0} & \cdots & \mathbf{0} & \cdots \\ \mathbf{0} & \boldsymbol{K}^i_{st} & \mathbf{0} & \boldsymbol{K}^j_{st} & \mathbf{0} \\ \vdots & \mathbf{0} & \ddots & \mathbf{0} & \vdots \\ \mathbf{0} & -\boldsymbol{K}^i_{st} & \mathbf{0} & \mathbf{0} & \mathbf{0} \\ \vdots & \mathbf{0} & \vdots & \mathbf{0} & \ddots \end{pmatrix} \end{array}}_{\boldsymbol{K}_{st}} \underbrace{\begin{pmatrix} \vdots \\ \boldsymbol{f}^i \\ \vdots \\ \boldsymbol{f}^j \\ \vdots \end{pmatrix}}_{\boldsymbol{f}} = \underbrace{\begin{pmatrix} \vdots \\ \boldsymbol{b}^p_{st} \\ \vdots \\ \boldsymbol{b}^q_{st} \\ \vdots \end{pmatrix}}_{\boldsymbol{b}_{st}} \tag{2.8}$$

where

$$\boldsymbol{K}^i_{st} = \begin{bmatrix} x^i_1 & 0 \\ 0 & x^i_2 \\ x^i_2 & x^i_1 \end{bmatrix}; \quad \boldsymbol{b}^p_{st} = \begin{bmatrix} \Omega_p \bar{\sigma}^p_{11} \\ \Omega_p \bar{\sigma}^p_{22} \\ 2\Omega_p \bar{\sigma}^p_{12} \end{bmatrix}$$

Extension to 3D is again straightforward and is omitted for brevity. Similar to $\boldsymbol{K}_{eq}$, the matrix $\boldsymbol{K}_{st}$ has $dN_p(d+1)/2$ rows and dN_c columns, where d is the dimension (e.g., $d = 2$ for 2D), N_p is the total number of particles in the assembly and N_c is the total number of contact points in the assembly.

2.2.3 Cohesionless and tangential forces

Cohesion-less granular materials in equilibrium obey two additional laws: normal forces are repulsive and tangential forces are governed by a Coulomb type friction law. The latter constraint requires that $|f_t| \leq \mu |f_n|$, where f_t is a tangential force magnitude, f_n is a corresponding normal force magnitude, and μ is the inter-particle coefficient of friction. These two constraints can be written for any contact point

acting on the p^{th} particle as:

$$-\boldsymbol{e}^i \cdot \boldsymbol{f}^i \geq 0 \tag{2.9}$$

$$-(\boldsymbol{e}^i + \frac{1}{\mu}\boldsymbol{t}^i) \cdot \boldsymbol{f}^i \geq 0 \tag{2.10}$$

$$-(\boldsymbol{e}^i - \frac{1}{\mu}\boldsymbol{t}^i) \cdot \boldsymbol{f}^i \geq 0 \tag{2.11}$$

where $\boldsymbol{e}^i$ and $\boldsymbol{t}^i$ represent normal and tangential unit vectors at the contact point i for a particular particle Ω_p, as shown in Figure 2.8.

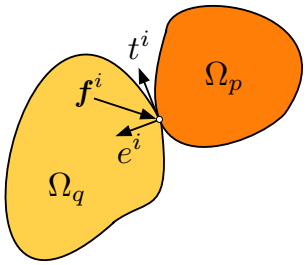

Figure 2.8: Unit vectors for contact i.

Equations (2.9), (2.10), and (2.11) can be combined into a single matrix expression for an entire assembly of particles: $\boldsymbol{B}\boldsymbol{f} \geq \boldsymbol{0}$. In 2D, the system takes the form:

$$\begin{array}{c} \\ i \\ \vdots \\ j \\ i \\ \vdots \\ j \\ i \\ \vdots \\ j \end{array}
\begin{array}{c}
\begin{array}{ccccc} i & i & & j & j \end{array} \\
\begin{bmatrix}
-e_1^i & -e_2^i & 0 & 0 & 0 \\
0 & 0 & \ddots & 0 & 0 \\
0 & 0 & 0 & -e_1^j & -e_2^j \\
-e_1^i - \frac{1}{\mu}t_1^i & -e_2^i - \frac{1}{\mu}t_2^i & 0 & 0 & 0 \\
0 & 0 & \ddots & 0 & 0 \\
0 & 0 & 0 & -e_1^j - \frac{1}{\mu}t_1^j & -e_2^j - \frac{1}{\mu}t_2^j \\
-e_1^i + \frac{1}{\mu}t_1^i & -e_2^i + \frac{1}{\mu}t_2^i & 0 & 0 & 0 \\
0 & 0 & \ddots & 0 & 0 \\
0 & 0 & 0 & -e_1^j + \frac{1}{\mu}t_1^j & -e_2^j + \frac{1}{\mu}t_2^j
\end{bmatrix}
\end{array}
\begin{pmatrix} f_1^i \\ f_2^i \\ \vdots \\ f_1^j \\ f_2^j \end{pmatrix}
\geq
\begin{bmatrix} 0 \\ \vdots \\ \vdots \\ \vdots \\ 0 \end{bmatrix} \tag{2.12}$$

where subscripts refer to vector components and superscripts refer to particular con-

tact points. Extension to 3D is straightforward and is omitted for brevity. In general, $\boldsymbol{B} \in \mathbb{R}^{3N_c \times dN_c}$.

2.2.4 Structure of equations and connection to experiments

The three matrix equations detailed in this section encapsulate equilibrium relations, constitutive relations, and contact laws for each particle in a granular material in terms of the unknown force components. When the sum of the number of linearly independent rows in both $\boldsymbol{K}_{st}$ and $\boldsymbol{K}_{eq}$ exceeds the number of columns in one of these matrices, there are more equations than unknown force components. Furthermore, when $\boldsymbol{K}_{eq}$ has more linearly independent columns than rows, $\boldsymbol{K}_{eq}\boldsymbol{f} = \boldsymbol{0}$ has an infinite number of solutions and forces can be inferred using the inverse problem formulation detailed in Section 2.3. In many practical examples of interest, these conditions will be met as indicated by observed coordination numbers in stable static granular packings [64].

Experimentally measured quantities are required input to the three matrix equations (2.5), (2.8), (2.12). These quantities can be measured with any suitable procedure and the structure of the equations will remain unchanged. In particular, the matrices $\boldsymbol{K}_{st}$, $\boldsymbol{K}_{eq}$, and $\boldsymbol{B}$ contain contact locations and normal and tangent vectors to each contact plane, which can be extracted from experiments using high-resolution photography or X-ray techniques in connection with DIC or level-set methods. Friction coefficients in $\boldsymbol{B}$ can be estimated using existing literature or experiments. Finally, the vector $\boldsymbol{b}_{st}$ contains particle areas (or volumes) and average particle stresses. Particle areas (or volumes) can be extracted using image (or data) processing techniques. Particle stresses can be determined by first extracting strain fields using DIC or other algorithms, and then by applying a suitable constitutive relation. Because the mathematical framework incorporates only a single dataset corresponding to one instant in time, it does not currently allow for history dependent constitutive relations and therefore requires a linear or nonlinear elastic relation.

2.3 Mathematical framework

This section presents the inverse problem formulation for inferring inter-particle forces using the equations $\boldsymbol{K}_{eq}\boldsymbol{f} = \boldsymbol{0}$, $\boldsymbol{B}\boldsymbol{f} \geq \boldsymbol{0}$, and $\boldsymbol{K}_{st}\boldsymbol{f} = \boldsymbol{b}_{st}$.

2.3.1 Inverse problem formulation

When the conditions discussed in section 2.2 are satisfied, the unknown force components can be inferred by satisfying equilibrium precisely, and minimizing an L_2-norm cost function involving forces and average particle stresses:

$$\boldsymbol{f} = \arg\min_{\boldsymbol{f}} \|\boldsymbol{K}_{st}\boldsymbol{f} - \boldsymbol{b}_{st}\|_2 \tag{2.13a}$$

$$\text{subject to: } \boldsymbol{K}_{eq}\boldsymbol{f} = \boldsymbol{0} \tag{2.13b}$$

$$\boldsymbol{B}\boldsymbol{f} \geq \boldsymbol{0} \tag{2.13c}$$

The L_2-norm cost function (2.13a) is typical in inverse problems and represents only one possible cost function for force-inference. In theory, the mathematical framework may be extended to incorporate other cost functions when the structure of noise in $\boldsymbol{b}_{st}$ (or in other variables) is well known. In general, however, this noise cannot be easily characterized for all possible experimental techniques adaptable to GEM, and in fact is very difficult to characterize even for a single procedure such as DIC (e.g., see [65]). Therefore, use of the L_2-norm cost function is retained in the present chapter as an example of a method with simple interpretation and implementation, and simple conditions for existence and uniqueness, but not as the only possible method. The inverse problem formulation in equation (2.13) has been reliable in all practical implementations by the authors.

It is important to note that the constraint in equation (2.13c) is not needed in most cases to obtain an accurate solution. In fact, this constraint is unnecessary and does not influence the solution obtained using equation (2.13) except when significant noise is present in experimental measurements. In the case when such noise is present, the constraint (2.13c) plays the role of ensuring that the selected solution

is physically admissible since noise may bias the result towards a force distribution with unrealistically high tangential to normal force ratios or attractive contact forces. The constraint (2.13c) can also be modified to eliminate the dependence on Coulomb friction when a Coulomb friction law is unjustified or when the friction coefficient cannot be estimated. When Coulomb friction is abandoned, the restriction will only require that normal forces be repulsive.

Conditions for the existence and uniqueness of a solution to equation (2.13) are easy to understand. It must be emphasized, however, that existence and uniqueness of a solution to equation (2.13) does not imply that the solution corresponds to the true inter-particle forces but rather to a solution that minimizes the error between experimental observations and calculations made with the governing equations of the problem in an L_2-norm sense.

Let $\mathcal{S} = \{\boldsymbol{f} | \boldsymbol{K}_{eq}\boldsymbol{f} = \boldsymbol{0}, \boldsymbol{B}\boldsymbol{f} \geq \boldsymbol{0}\}$, the set of force vectors that satisfy the constraints (2.13b) and (2.13c). A solution to (2.13) exists when $\mathcal{S}$ is nonempty since the cost function in (2.13a) is bounded below by 0, e.g., when $\boldsymbol{K}_{st}$ is positive semi-definite. Furthermore, $\mathcal{S}$ is nonempty when $\boldsymbol{K}_{eq}$ has more columns than rows, and when $\boldsymbol{B}\boldsymbol{f} \geq \boldsymbol{0}$ is solvable, which can be ensured in practice by choosing μ conservatively. The solution is unique if there is no $\boldsymbol{w} \neq \boldsymbol{0}$ such that $\boldsymbol{w} \in \mathcal{N}(\boldsymbol{K}_{st}) \cap \mathcal{N}(\boldsymbol{K}_{eq})$ (see proof and other conditions in Theorem 1 of [66]); such a $\boldsymbol{w}$ could be added to any existing solution without changing the value of the cost function in (2.13a) or violating the equality (2.13b).

From a physical perspective, such a $\boldsymbol{w}$ is unlikely to exist: nonzero forces in $\mathcal{N}(\boldsymbol{K}_{st})$ satisfy $\boldsymbol{K}_{st}\boldsymbol{f} = \boldsymbol{0}$ and must cause rigid body particle motion while forces in $\mathcal{N}(\boldsymbol{K}_{eq})$ satisfy $\boldsymbol{K}_{eq}\boldsymbol{f} = \boldsymbol{0}$ and must result in equilibrium. When $\boldsymbol{K}_{eq}$ and $\boldsymbol{K}_{st}$ are rank deficient, such a $\boldsymbol{w}$ may exist and additional criteria must be satisfied to ensure uniqueness; namely, the $\boldsymbol{w} \in \mathcal{N}(\boldsymbol{K}_{st}) \cap \mathcal{N}(\boldsymbol{K}_{eq})$ must violate the restrictions of constraint (2.13c) to ensure that the solution to (2.13) remains unique. It is merely stated here that the authors have never found such a $\boldsymbol{w}$ to exist in both numerical simulations and experiments, ensuring the uniqueness of solution to (2.13).

2.3.2 Measurement noise and alternative formulation

Experimental imaging techniques contain error, or measurement noise. In addition, algorithms used to extract strain fields, contact locations, contact planes, and constitutive law parameters introduce noise. This noise manifests itself in the matrices $\boldsymbol{K}_{eq}$, $\boldsymbol{K}_{st}$, and $\boldsymbol{B}$ and in the vector $\boldsymbol{b}_{st}$. While high-fidelity imaging can typically ensure negligibly small error in the point-wise quantities used to populate $\boldsymbol{K}_{eq}$, $\boldsymbol{K}_{st}$, and $\boldsymbol{B}$, the vector $\boldsymbol{b}_{st}$ requires accurate estimation of the particle constitutive model and associated parameters, and involves a sum over all point-wise measured stresses in a particle, potentially introducing significant error.

To account for the possibility of significant measurement error in $\boldsymbol{b}_{st}$ a simple alternative to the inverse problem (2.13) is proposed which incorporates knowledge of boundary forces, quantities that are typically found by using load cells in experiments. The alternative method is motivated by the experience that when the solution to (2.13) is affected by measurement error in the constitutive law, the relative sizes of forces remains relatively unchanged (i.e., all forces are generally over- or underestimated). The alternative inverse problem is given by:

$$\boldsymbol{f} = \arg\min_{\boldsymbol{f}} \|\boldsymbol{K}_{st}\boldsymbol{f} - \boldsymbol{b}_{st}\|_2 + \lambda^2\|\boldsymbol{f}\|_2 \tag{2.14a}$$

$$\text{subject to: } \boldsymbol{K}_{eq}\boldsymbol{f} = \boldsymbol{0} \tag{2.14b}$$

$$\boldsymbol{B}\boldsymbol{f} \geq \boldsymbol{0} \tag{2.14c}$$

where λ is a regularization parameter, to be discussed.

Problem (2.14) employs Tikhonov regularization, a common technique in the solution of ill-posed or rank-deficient inverse problems (e.g., [67, 68]). Tikhonov regularization can be interpreted as a method for incorporating prior knowledge of the magnitude of $\boldsymbol{f}$ and as a technique for selecting a "smoother" solution. This can be seen intuitively: as λ is increased, the solution will decrease until each value of $\boldsymbol{f}$ approaches 0. Furthermore, the solution will typically decrease with some uniformity in that each value of $\boldsymbol{f}$ will approach 0 at a rate proportional to its size. It is im-

portant to note, however, that the solution to problem (2.14) will still satisfy particle equilibrium.

The primary challenge in using the alternative form (2.14) is selecting λ to find a tradeoff between noise reduction and loss of information [68]. When the structure of noise in $\boldsymbol{b}_{st}$ is well known, many methods exist to select λ, although all methods have known issues and limitations [69]. The technique used in this chapter to select λ is simple and has been proven effective by experience: gradually increase λ until a solution $\boldsymbol{f}$ to (2.14) minimizes the difference between known and calculated boundary forces. Example of implementing this procedure are presented in the next section and the experimental example in section 2.1. In general, the mathematical framework presented in this section may be extended to incorporate penalty functions other than Tikhonov regularization, but it is beyond the scope of this chapter to address all of these possibilities. It is important to note that solution of equation (2.14), as with the solution of equation (2.13), will produce forces that satisfy particle equilibrium.

2.3.3 Implementation

Many solvers and optimization packages exist to solve the minimization problem (2.13) or (2.14). In particular, implementations of SeDuMi [70] such as CVX [71] and Yalmip [72] provide efficient ways to solve the problem in Matlab. In addition, any numerical optimization package capable of solving quadratic programming problems can be used to solve (2.13) and (2.14) when the cost functions in these problems are expanded to quadratic form (e.g.: $\min\{\boldsymbol{f}^T\boldsymbol{K}_{st}^T\boldsymbol{K}_{st}\boldsymbol{f} - 2\boldsymbol{b}^T\boldsymbol{K}_{st}\boldsymbol{f}\}$). Since the matrices $\boldsymbol{K}_{eq}$ and $\boldsymbol{K}_{st}$ may not be full rank in practice, solvers capable of handling rank deficient matrices may be preferred.

2.4 Numerical example

This section presents a numerical example of implementing GEM. This example is used to demonstrate the salient features of the method in an environment where the exact solution, or exact inter-particle forces, is known. A metric used throughout this

example is relative error, $\|\delta \boldsymbol{f}\|$, defined as:

$$\|\delta \boldsymbol{f}\| = \frac{\|\boldsymbol{f}^{\text{Calculated}} - \boldsymbol{f}^{\text{Actual}}\|}{\|\boldsymbol{f}^{\text{Actual}}\|} \tag{2.15}$$

To generate a suitable data set for demonstrating the features of GEM, an odometric compression test was performed on a rectangular sample of 58 particles using the Discrete Element Method (DEM) [33]. The particle radii were uniformly distributed between 2.5 mm and 4 mm. The particle-particle and particle-wall coefficients of friction were 0.5 and zero, respectively. No gravity acted on the particles. The normal and tangential stiffnesses were 67.5 KN/mm. The applied compressive stress was 30 kPa on the top face, as shown in Figure 2.9.

2.4.1 Global force inference

After the DEM simulation neared an equilibrium state, contact forces, normal and tangential contact vectors, and average particle stresses determined by equation (2.7) were used to form the matrices $\boldsymbol{K}_{st}$, $\boldsymbol{K}_{eq}$, $\boldsymbol{B}$, and the vector $\boldsymbol{b}_{st}$. The inter-particle friction coefficient for all contacts was assumed to be 0.5. The problem (2.13) was solved and the exact inter-particle forces were recovered with relative error, $\|\delta \boldsymbol{f}\| \approx 0$. Since forces from DEM exactly matched those found using (2.13), the forces are plotted only once in Figure 2.9. Only forces with magnitude over 300 N are labeled.

2.4.2 Noise reduction

To demonstrate the application of the modified inverse problem (2.14), noise was added to each element of $\boldsymbol{b}_{st}$ as follows: each element was first increased by 15% to simulate overestimating the Young's modulus in a linearly elastic constitutive model, and then each element was added to the product of its original value with a unique number generated from a Gaussian distribution with mean 0 and standard deviation 0.1 to simulate noise generated from image resolution and strain field calculation

algorithms. Each element of the new $\boldsymbol{b}_{st}$ therefore took the form:

$$(\boldsymbol{b}_{st})_i = (\boldsymbol{b}_{st})_i + (0.15 + N(0, 0.1))(\boldsymbol{b}_{st})_i \tag{2.16}$$

where $N(0, 0.1)$ represents a number generated from a Gaussian distribution with mean 0 and standard deviation 0.1.

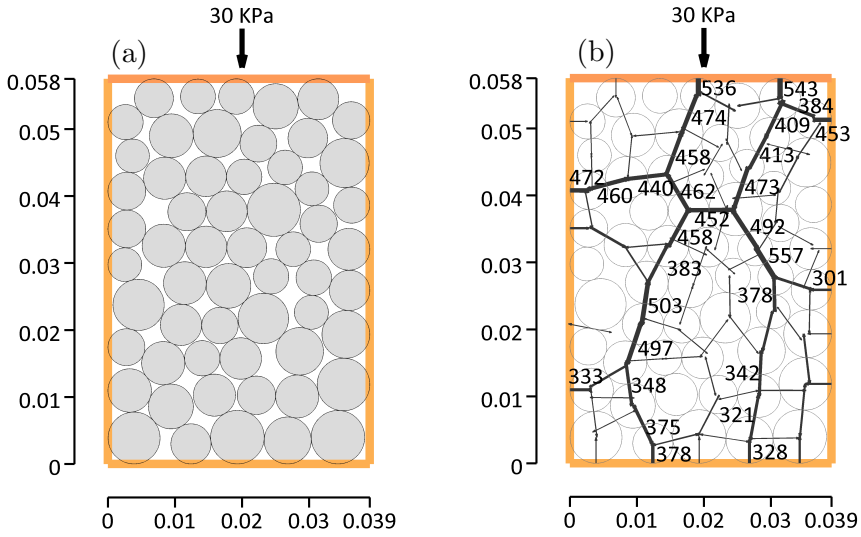

Figure 2.9: (a) Numerical odometric test setup. (b) Inter-particle forces computed with DEM and (2.13). Length scale in meters, forces in Newtons. Line thickness proportional to force magnitude.

Problem (2.13) was first solved, yielding results with $\|\delta \boldsymbol{f}\| = 0.154$ as shown in Figure 2.10. Despite the noticeable differences between the forces in Figure 2.10 and the exact forces, the solution in Figure 2.10 does not violate Coulomb friction by virtue of the inequality constraints used in the optimization problem (2.13).

Next, problem (2.14) was solved, yielding results with $\|\delta \boldsymbol{f}\| = 0.053$ as shown in Figure 2.10. The total force on the top boundary measured from the DEM simulation was approximately 1170 N. The regularization parameter λ was chosen to minimize the difference between this value and the sum of the particle-boundary reaction forces

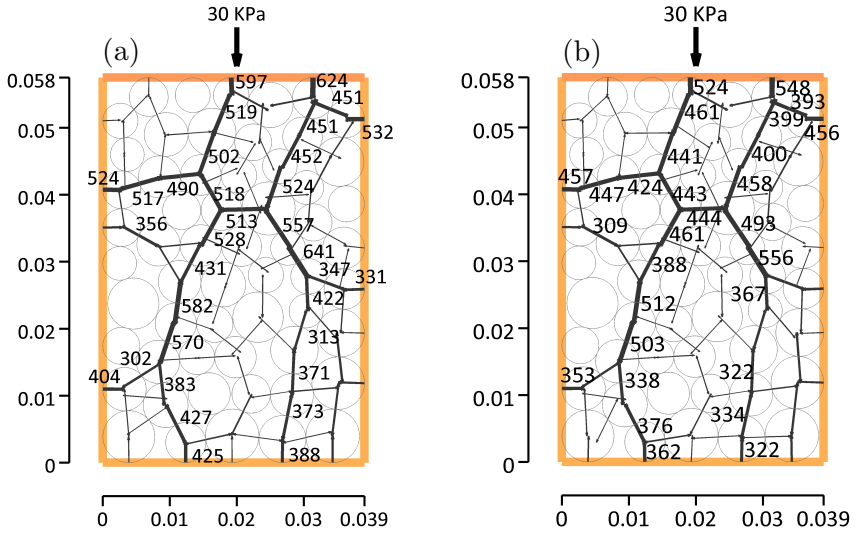

Figure 2.10: (a) Solution to (2.13) with artificial noise, $\|\delta \boldsymbol{f}\| = 0.154$. (b) Solution to (2.14) with same noise, $\|\delta \boldsymbol{f}\| = 0.053$ (right).

on the top boundary:

$$\text{Total Difference} = |1170 + \sum_{\alpha}^{N_c^b} f_2^{\alpha}| \tag{2.17}$$

where N_c^b is the number of contact points on the top boundary and f_2^{α} is the vertical component of force acting at contact points along the top boundary. A value of $\lambda = 0.0714$ was found to minimize this total difference by solving (2.14) with a variety of values over an interval between 0.06 and 0.075.

From the reduced relative error and a qualitative comparison of Figures 2.9 and 2.10, it is clear that the formulation in equation (2.14) significantly improved the accuracy of the solution to the inverse problem. The effect of overestimating Young's modulus was nearly eliminated and the relative error was reduced to levels more representative of the Gaussian noise alone. Other numerical examples not presented here demonstrate the same capability with other forms of artificial measurement noise. This alternative formulation of the inverse problem represents an important extension of GEM for practitioners, providing a means for obtaining solutions with higher accuracy. It is important to note, however, that this method is largely based on judg-

ment: selection of λ is an interactive process, particularly when using the method of minimizing a non-convex function like the total difference in (2.17).

2.4.3 Local force inference

The proposed formulation in equation (2.13) has the capability of extracting forces locally within a material. To demonstrate this capability, force inference was performed on six particles, as shown in Figure 2.11. The contact points, corresponding normal and tangent vectors, and average particle stresses for these particles only were used to form the quantities $\boldsymbol{K}_{st}$, $\boldsymbol{K}_{eq}$, $\boldsymbol{b}_{st}$, and $\boldsymbol{B}$. The contact forces were inferred using (2.13). Comparison with Figure 2.9 shows that the inferred local contact forces exactly match those from the DEM simulation.

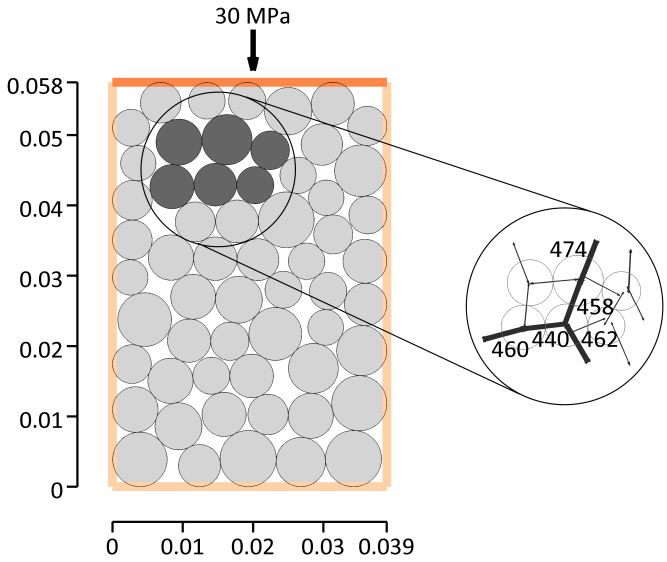

Figure 2.11: Solution to (2.13) performed locally within granular material.

The capability of the proposed method to infer contact forces locally represents an important feature of GEM. This feature allows force inference in regions of interest (e.g., shear bands) without the necessity of solving an inverse problem for the entire assembly. Furthermore, this feature may allow GEM to be used in connection with

larger experiments since only a small portion of the material's fabric needs to be imaged and processed.

2.5 Conclusion

The improved formulation of GEM presented in this chapter provides a powerful methodology for investigating inter-particle forces in granular materials. The first experimental example using GEM has been showcased to demonstrate that the method can and has been applied to real materials. The presentation of the mathematical framework illustrates its simplicity and versatility, and offers many possibilities of extending the framework to incorporate additional experimental measurements such as boundary forces. With progress in experimental imaging and intra-particle strain field extraction (e.g., [49, 50]), GEM will soon be able to extract inter-particle forces in materials with smaller grains like sands, providing the first chance to validate many theories regarding force networks in natural granular media. GEM will also advance the boundaries of the micro-mechanical understanding of granular materials by offering a characterization tool for a new class of opaque complex assemblies.

Chapter 3

Dynamic inter-particle force inference in granular materials: Method and application[1]

3.1 Introduction

In this chapter, we extend GEM to the dynamic regime, providing a new tool for quantitative inter-particle force measurements in granular media. The method currently is restricted only by the limitation of experimental techniques to supply measurements of particle positions, contact points, and volume-averaged grain stresses in the material of interest. However, the mathematical foundation and inverse problem formulation that the method employs is independent of particle properties or contact law.

In section 3.2 we discuss the necessary experimental measurements, image processing techniques, and theory behind the numerical optimization problem used in the method. Section 3.3 illustrates an experimental example in which the method is used to infer forces between a group of two-dimensional rubber grains impacted by a foreign intruder. A comparison of the experimental results with a finite-element simulation is provided to validate the results of the method. Section 3.4 will feature results from a preliminary application of the method to force inference during impact

[1] Adapted from R.C. Hurley, K.W. Lim, G. Ravichandran, J.E. Andrade. Dynamic inter-particle force inference in granular materials: Method and application. *Experimental Mechanics*, 2015. DOI: 10.1007/s11340-015-0063-8

of an intruder on a model granular bed. Section 3.5 will discuss the current challenges faced during application of the method and provide insight into the new physics the tool can unravel. Finally, section 3.6 will offer concluding remarks.

3.2 The method

The method for inferring inter-particle forces involves two steps: (1) experimental measurements, and (2) solving a numerical optimization problem. Item (1) is briefly discussed to highlight the required measurements and some techniques capable of providing them. Item (2) is discussed in more detail since the numerical optimization problem is the cornerstone of the method.

3.2.1 Experimental measurements

The first step of the method involves performing a dynamic experiment of interest and extracting the evolution of particle positions, inter-particle contact points, inter-particle contact surface normals, and the evolution of volume-averaged grain stresses. These measurements are required as input for the numerical optimization problem and, once measured, provide enough information to accurately infer inter-particle forces. No restrictions are inherently placed on the particle shape or dimensionality of the experiment and no prior assumption is needed of the contact law between grains.

Particle positions and contact points can be found in 2D experiments using high-speed photography and particle segmentation algorithms. In 3D, XRCT provides a suitable method for extracting particle positions and contact points. As stated in the introduction, XRCT is still an area of active research and has not yet been applied to large dynamic experiments [52,53,54]. The proposed force inference method is therefore not yet suitable for application to 3D experiments. Nevertheless, we will elaborate on the 3D formulation of the inverse problem for completeness. Once particle positions and contact points have been obtained, normal and tangent vectors can be found for each contact point using the local edge features.

Volume-averaged grain stresses can be found from volume-averaging the full-field grain stress computed point-wise. For linear elastic materials volume-averaged grain stresses can also be computed directly from volume-averaged grain strains using $\bar{\boldsymbol{\sigma}}_p = \boldsymbol{C} : \bar{\boldsymbol{\epsilon}}_p$, where $\boldsymbol{C}$ is the stiffness tensor. In either case, a constitutive law is required to obtain volume-averaged grain stresses. Such constitutive laws - linear elastic, hyperelastic, plastic, etc. - can be determined using experiments not discussed here. Full-field grain strains are needed to obtain volume-averaged grain stresses when experiments involve non-linear elastic grain materials or grains undergoing plastic deformation. Full-field grain strains can be found using digital image correlation (DIC) [55] in 2D or a combination of 3D X-ray diffraction (3DXRD) and XRCT in 3D [49, 50, 51, 73]. Digital volume correlation (DVC) can also be used with XRCT or similar methods to obtain full-field strains in 3D. The methods for obtaining full-field grain strains (DIC, DVC, XRCT, 3DXRD) typically rely on internal grain contrast (e.g., see [55]). Like XRCT, 3DXRD is a field of active research and has not yet been applied to dynamic experiments.

3.2.2 Numerical optimization

The numerical optimization problem used to infer inter-particle forces from experimental measurements requires three sets of governing equations: momentum balance, stress-force relations, and constraint equations.

The momentum balance equations for a deformable body are derived as follows. The balance of linear momentum arises from noting that the total force on a deformable particle equals the time derivative of its linear momentum:

$$\frac{\mathrm{d}}{\mathrm{d}t}\left(\int_{V_p} \rho \boldsymbol{v}\,\mathrm{d}v\right) = \int_{V_p} \rho \boldsymbol{b}\,\mathrm{d}v + \int_{\partial V_p} \boldsymbol{t}\,\mathrm{d}s \tag{3.1}$$

where ρ is the particle density, $\boldsymbol{b}$ is the body force, $\boldsymbol{t}$ are surface tractions, $\boldsymbol{v}$ is velocity, and V_p and ∂V_p represent deformed grain volumes and edges, respectively. Taking

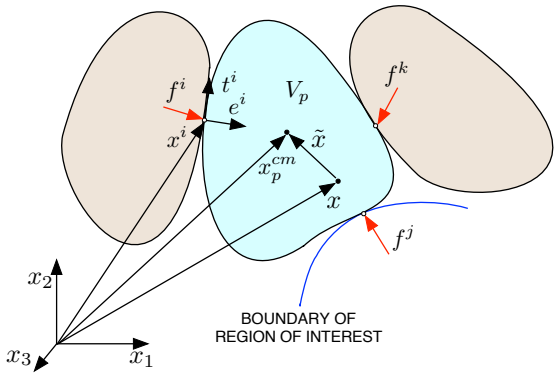

Figure 3.1: Illustration of various terms used in the governing equations.

the derivative and ignoring body forces, one obtains

$$\sum_{\alpha=1}^{N_c^p} \boldsymbol{f}^\alpha = \int_{V_p} \rho \boldsymbol{a} \, \mathrm{d}v \tag{3.2}$$

where $\boldsymbol{f}^\alpha$ is a contact point as shown in Fig. 3.1 and N_c^p is the total number of contact points for particle p. We have made use of the fact that integrating tractions on disjoint sections of a surface is equivalent to summing the total force on each of those sections. We can further reduce Eq. (3.2) by making use of the definition of center-of-mass acceleration to obtain

$$\sum_{\alpha=1}^{N_c^p} \boldsymbol{f}^\alpha = m_p \boldsymbol{a}_p^{cm} \tag{3.3}$$

The balance of angular momentum arises from noting that the total torque on a deformable particle is equal to the time derivative of its angular momentum:

$$\frac{\mathrm{d}}{\mathrm{d}t} \left(\int_{V_p} \boldsymbol{x} \times \rho \boldsymbol{v} \, \mathrm{d}v \right) = \int_{V_p} \boldsymbol{x} \times \rho \boldsymbol{b} \, \mathrm{d}v + \int_{\partial V_p} \boldsymbol{x} \times \boldsymbol{t} \, \mathrm{d}s \tag{3.4}$$

where $\boldsymbol{x}$ is a position vector and $\times$ represents a cross product of two vectors. Taking the derivative and ignoring body forces, one obtains

$$\sum_{c=1}^{N_c^p} \boldsymbol{x}^c \times \boldsymbol{f}^c = \int_{V_p} \boldsymbol{x} \times \rho \boldsymbol{a} \, \mathrm{d}v \tag{3.5}$$

where we have made use of the same argument as above to turn the integral into a sum while approximating the contact point $\boldsymbol{x}^c$ as the center of the contact area. Now define $\boldsymbol{x} = \boldsymbol{x}_p^{cm} + \tilde{\boldsymbol{x}}$ and $\boldsymbol{a} = \boldsymbol{a}_p^{cm} + \tilde{\boldsymbol{a}}$, where $\boldsymbol{x}_p^{cm}$ and $\boldsymbol{a}_p^{cm}$ are the position and acceleration of the center-of-mass, respectively. Plugging these into Eq. (3.5) yields

$$\sum_{c=1}^{N_c^p} \boldsymbol{x}^c \times \boldsymbol{f}^c = m_p(\boldsymbol{x}_p^{cm} \times \boldsymbol{a}_p^{cm}) + \int_{V_p} \rho(\tilde{\boldsymbol{x}} \times \tilde{\boldsymbol{a}})\,\mathrm{d}v \tag{3.6}$$

Note that the second term on the right hand side of this equation is negligibly small when accelerations within a grain remain small relative to its center-of-mass acceleration.

Linear and angular momentum balance, Eqs. (3.3) and (3.6), can be combined into a single matrix equation for a group of contacting particles, taking the form

$$\underbrace{\begin{array}{c} \\ p \\ \\ q \\ \\ \end{array}\!\!\begin{array}{c} \begin{array}{ccccc} & & i & & j & \\ \end{array} \\ \begin{pmatrix} \ddots & \mathbf{0} & \cdots & \mathbf{0} & \cdots \\ \mathbf{0} & \boldsymbol{K}_m^i & \mathbf{0} & \boldsymbol{K}_m^j & \mathbf{0} \\ \vdots & \mathbf{0} & \ddots & \mathbf{0} & \vdots \\ \mathbf{0} & -\boldsymbol{K}_m^i & \mathbf{0} & \mathbf{0} & \mathbf{0} \\ \vdots & \mathbf{0} & \vdots & \mathbf{0} & \ddots \end{pmatrix} \end{array}}_{\boldsymbol{K}_m} \underbrace{\begin{pmatrix} \vdots \\ \boldsymbol{f}^i \\ \vdots \\ \boldsymbol{f}^j \\ \vdots \end{pmatrix}}_{\boldsymbol{f}} = \underbrace{\begin{pmatrix} \vdots \\ \boldsymbol{b}_m^p \\ \vdots \\ \boldsymbol{b}_m^q \\ \vdots \end{pmatrix}}_{\boldsymbol{b}_m} \tag{3.7}$$

where p and q represent particles, i and j represent particle-particle and particle-boundary contacts as shown in Fig. 3.1, and $\boldsymbol{K}_m^i$, $\boldsymbol{f}^i$, and $\boldsymbol{b}_m^p$ encompass Eqs. (3.3)

and (3.6) and in 2D take the form

$$\boldsymbol{K}^i_m = \begin{bmatrix} 1 & 0 \\ 0 & 1 \\ -x_2^i & x_1^i \end{bmatrix}; \quad \boldsymbol{f}^i = \begin{pmatrix} f_1^i \\ f_2^i \end{pmatrix} \tag{3.8}$$

$$\boldsymbol{b}^p_m = \begin{bmatrix} m_p \boldsymbol{a}_1^{cm} \\ m_p \boldsymbol{a}_2^{cm} \\ m_p(x_1^{cm} a_2^{cm} - x_2^{cm} a_1^{cm}) \end{bmatrix} \tag{3.9}$$

where we have omitted the integral term from Eq. (3.6) for brevity. In general, $3N_p$ equations are contained in Eq. 5.1, where N_p is the number of particles in the region of interest. Extension of $\boldsymbol{K}^i_m$, $\boldsymbol{f}^i$, and $\boldsymbol{b}^p_m$ to 3D is straightforward.

The stress force relations are derived as follows. The volume-averaged stress in a deformable particle can be written as

$$\bar{\boldsymbol{\sigma}}_p = \frac{1}{V_p} \int_{V_p} \boldsymbol{\sigma} \, \mathrm{d}v \tag{3.10}$$

Left-multiplying the $\boldsymbol{\sigma}$ within the integral by the identity matrix $x_{i,k}$ and switching to index notation yields

$$\bar{\sigma}_{ij} = \frac{1}{V_p} \int_{V_p} \left[(x_i \sigma_{kj})_{,k} - x_i \sigma_{kj,k} \right] \mathrm{d}v \tag{3.11}$$

Using the divergence theorem on the first term inside the integral of this equation and balance of linear momentum in the absence of body forces ($\sigma_{kj,k} = \rho a_j$) on the second term, we obtain

$$\sum_{c=1}^{N_c^p} \boldsymbol{x}^c \otimes \boldsymbol{f}^c = V_p \bar{\boldsymbol{\sigma}}_{V_p} + \int_{V_p} \boldsymbol{x} \otimes \rho \boldsymbol{a} \, \mathrm{d}v \tag{3.12}$$

where $\otimes$ is a dyadic product ($\boldsymbol{a} \otimes \boldsymbol{b} = a_i b_j$). Finally, defining $\boldsymbol{x} = \boldsymbol{x}_p^{cm} + \tilde{\boldsymbol{x}}$ and

$\boldsymbol{a} = \boldsymbol{a}_p^{cm} + \tilde{\boldsymbol{a}}$ as above, we obtain

$$\sum_{c=1}^{N_c^p} \boldsymbol{x}^c \otimes \boldsymbol{f}^c = V_p \bar{\boldsymbol{\sigma}} + m_p(\boldsymbol{x}^{cm} \otimes \boldsymbol{a}^{cm}) + \int_{V_p} \tilde{\boldsymbol{x}} \otimes \rho \tilde{\boldsymbol{a}} \, \mathrm{d}v \tag{3.13}$$

Once again, we note that the third term on the right hand side of this equation is negligibly small when accelerations within a grain remain small relative to its center-of-mass acceleration.

The stress-force relation in Eq. (3.13) can also be written into a matrix equation for a group of contacting particles, taking the form

$$\underbrace{\begin{array}{c} \\ p \\ \\ q \\ \\ \end{array}\!\!\begin{array}{c} \begin{array}{ccccc} & & i & & j & \\ \end{array} \\ \begin{pmatrix} \ddots & \mathbf{0} & \cdots & \mathbf{0} & \cdots \\ \mathbf{0} & \boldsymbol{K}_s^i & \mathbf{0} & \boldsymbol{K}_s^j & \mathbf{0} \\ \vdots & \mathbf{0} & \ddots & \mathbf{0} & \vdots \\ \mathbf{0} & -\boldsymbol{K}_s^i & \mathbf{0} & \mathbf{0} & \mathbf{0} \\ \vdots & \mathbf{0} & \vdots & \mathbf{0} & \ddots \end{pmatrix} \end{array}}_{\boldsymbol{K}_s} \underbrace{\begin{pmatrix} \vdots \\ \boldsymbol{f}^i \\ \vdots \\ \boldsymbol{f}^j \\ \vdots \end{pmatrix}}_{\boldsymbol{f}} = \underbrace{\begin{pmatrix} \vdots \\ \boldsymbol{b}_s^p \\ \vdots \\ \boldsymbol{b}_s^q \\ \vdots \end{pmatrix}}_{\boldsymbol{b}_s} \tag{3.14}$$

where $\boldsymbol{f}^i$ is the same as in Eq. (3.8), and $\boldsymbol{K}_s^i$ and $\boldsymbol{b}_s^p$ encompass Eq. (3.13) and in 2D take the form

$$\boldsymbol{K}_s^i = \begin{bmatrix} x_1^i & 0 \\ 0 & x_2^i \\ x_2^i & x_1^i \end{bmatrix} \tag{3.15}$$

$$\boldsymbol{b}_s^p = \begin{bmatrix} V_p \bar{\sigma}_{11} + m_p(x_1^{cm} a_1^{cm}) \\ V_p \bar{\sigma}_{22} + m_p(x_2^{cm} a_2^{cm}) \\ 2V_p \bar{\sigma}_{12} + m_p(x_1^{cm} a_2^{cm} + x_2^{cm} a_1^{cm}) \end{bmatrix} \tag{3.16}$$

where we have omitted the integral terms from Eq. (3.13) for brevity. In general, $3N_p$ equations are also contained in Eq. 3.14. Extension of $\boldsymbol{K}_s^i$ and $\boldsymbol{b}_s^p$ to 3D is

straightforward.

Constraint equations can also be written for a group of cohesionless grains obeying a Coulomb-type friction law. These constraints in 2D require that $(\boldsymbol{f}^i \cdot \boldsymbol{e}^i) \geq 0$ and $(\mu \boldsymbol{e}^i \pm \boldsymbol{t}^i) \cdot \boldsymbol{f}^i \geq 0$ where $\boldsymbol{e}^i$ and $\boldsymbol{t}^i$ are the normal and tangential to the contact surface of contact point i as shown in Fig. 3.1 and μ is the inter-particle friction coefficient. This friction coefficient can be measured from a separate experiment performed on the particle material and may be either dynamic or static depending on the nature of the experiment. In 3D, the tangential direction must be specified by two vectors and the Coulomb friction constraint written above must be modified during implementation in the numerical optimization problem. We will continue with the 2D form and discuss the 3D extension briefly below.

The cohesionless force and Coulomb friction constraint equations can be expressed as a matrix equation for a group of contacting particles, taking the form $\boldsymbol{B}\boldsymbol{f} \geq \boldsymbol{0}$ where

$$\boldsymbol{B} = \begin{array}{c} \\ i \\ \vdots \\ j \\ i \\ \vdots \\ j \\ i \\ \vdots \\ j \end{array} \begin{array}{c} \begin{array}{ccccc} i & i & & j & j \end{array} \\ \begin{pmatrix} e_1^i & e_2^i & \mathbf{0} & \mathbf{0} & \mathbf{0} \\ \mathbf{0} & \mathbf{0} & \ddots & \mathbf{0} & \mathbf{0} \\ \mathbf{0} & \mathbf{0} & 0 & e_1^j & e_2^j \\ \mu e_1^i + t_1^i & \mu e_2^i + t_2^i & \mathbf{0} & \mathbf{0} & \mathbf{0} \\ \mathbf{0} & \mathbf{0} & \ddots & \mathbf{0} & \mathbf{0} \\ \mathbf{0} & \mathbf{0} & 0 & \mu e_1^j + t_1^j & \mu e_2^j + t_2^j \\ \mu e_1^i - t_1^i & \mu e_2^i - t_2^i & \mathbf{0} & \mathbf{0} & \mathbf{0} \\ \mathbf{0} & \mathbf{0} & \ddots & \mathbf{0} & \mathbf{0} \\ \mathbf{0} & \mathbf{0} & 0 & \mu e_1^j - t_1^j & \mu e_2^j - t_2^j \end{pmatrix} \end{array} \tag{3.17}$$

and $\boldsymbol{f} = (f_1^i \, f_2^i \ldots f_1^j \, f_2^j)^\top$. In general, $3N_c^p$ constraints are contained in Eq. (3.17), where N_c^p is the total number of contacts.

The mechanics of a group of contacting grains is fully governed by the three matrix Eqs. (5.1), (3.14), and $\boldsymbol{B}\boldsymbol{f} \geq \boldsymbol{0}$. Every term in these equations except for the inter-particle forces $\boldsymbol{f}$ must be measured during an experiment as described in section 3.2.1.

Once measured, finding the set of forces $\boldsymbol{f}$ that best fits the measured data involves solving a multi-objective optimization problem of the form:

$$\boldsymbol{f} = \arg\min_{\boldsymbol{f}} \left(||\boldsymbol{K}_s \boldsymbol{f} - \boldsymbol{b}_s||_2 + \lambda ||\boldsymbol{K}_m \boldsymbol{f} - \boldsymbol{b}_m||_2 \right) \tag{3.18a}$$

$$\text{subject to: } \boldsymbol{B}\boldsymbol{f} \geq \boldsymbol{0} \tag{3.18b}$$

Here, the objective functions $||\boldsymbol{K}_s \boldsymbol{f} - \boldsymbol{b}_s||_2$ and $||\boldsymbol{K}_m \boldsymbol{f} - \boldsymbol{b}_m||_2$ represent the desire to minimize the difference between inferred forces and experimental measurements of stress and momentum, respectively. The value λ is a weight that conveys the relative importance of the two objectives. No previous knowledge of boundary forces is needed as in past implementations of this inverse problem [13].

In order to solve Eq. (3.18), a suitable value of λ must be selected. With no prior knowledge of the type or magnitude of error in stress or momentum measurements, the best strategy is to seek a solution which does not favor one set of measurements (e.g., momentum or stress) over another. To do this, we solve Eq. (3.18) with many values of λ and obtain a curve of $||\boldsymbol{K}_s \boldsymbol{f} - \boldsymbol{b}_s||_2$ versus $||\boldsymbol{K}_m \boldsymbol{f} - \boldsymbol{b}_m||_2$, as shown in Fig 3.2. All points on this curve for which neither objective can be decreased without increasing the other are referred to as Pareto optimal points, and the resulting curve is referred to as the optimal trade-off curve or the Pareto front [74].

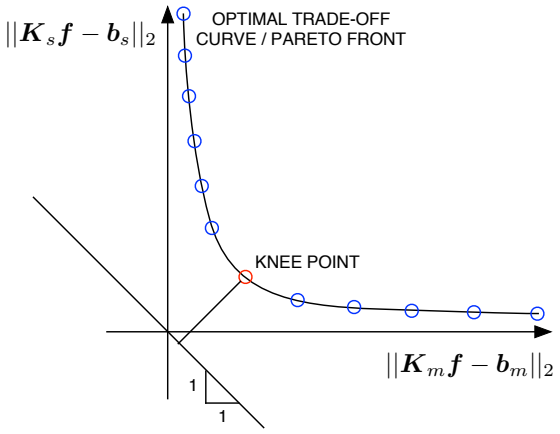

Figure 3.2: Pareto front.

In principle, any point on the optimal trade-off curve is a possible solution to the multi-objective problem. However, in order to use as much information in the two objective functions as possible, we wish to select a point where the slope of the trade-off curve is steep. At a steep point, a small decrease in one objective function is accompanied by a small increase in the other. This steep "knee" of the optimal trade-off curve therefore represents the solution where we satisfy each objective without making an unfavorably large sacrifice in the other.

Finally, we mention that when solving Eq. (3.18) for 2D experiments, special care must be taken because of the nonzero thickness of the disks or cylinders involved. In particular, the mass used in Eqs. (5.1) and (3.14) must be mass per unit thickness (i.e., actual mass divided by thickness of the particles) and the volume in Eq. (3.14) must be the area of the face of the particle. The result of solving Eq. (3.18) will be force per unit thickness, from which actual forces can be obtained by multiplying by the particle thickness.

In 3D, a contact surface between two particles must be specified by a normal vector and two orthogonal tangent vectors, $\boldsymbol{t}_1^i$ and $\boldsymbol{t}_2^i$, rather than one. Defining q_1^i and q_2^i to be the magnitude of $\boldsymbol{f}$ projected onto each tangent vector, the multi-objective optimization problem takes the form

$$\boldsymbol{f} = \arg\min \left(||\boldsymbol{K}_s \boldsymbol{f} - \boldsymbol{b}_s||_2 + \lambda ||\boldsymbol{K}_m \boldsymbol{f} - \boldsymbol{b}_m||_2 \right) \tag{3.19a}$$

$$\text{subject to: } \boldsymbol{e}^i \cdot \boldsymbol{f}^i \geq \boldsymbol{0} \tag{3.19b}$$

$$q_1^i = (\boldsymbol{t}_1^i \cdot \boldsymbol{f}) \tag{3.19c}$$

$$q_2^i = (\boldsymbol{t}_2^i \cdot \boldsymbol{f}) \tag{3.19d}$$

$$\mu(\boldsymbol{e}^i \cdot \boldsymbol{f}^i) - ||\boldsymbol{q}^i|| \geq 0 \tag{3.19e}$$

where $||\boldsymbol{q}^i|| = ((q_1^i)^2 + (q_2^i)^2)^{1/2}$. Many of the constraints in Eq. (3.19) can be cast in matrix form as in Eq. (3.18). However, the last constraint is a second-order cone constraint which is not present in the 2D problem and cannot be written in matrix form, instead requiring a norm [74]. For more details on this type of constraint,

see [74].

3.3 Example 1: Validation

This section contains a validation of the proposed force inference technique. An experiment is performed with a group of two-dimensional rubber grains impacted by a foreign intruder. Force inference is performed with the proposed method and the results are compared with those of a finite-element simulation of the experiment. The section is presented in three steps: (1) experimental setup; (2) experiment analysis; (3) experimental results and FEM comparison.

3.3.1 Experiment setup

The experimental setup is shown in Fig 3.3. The setup involves a small 0.4m x 0.6m table containing an air chamber under its upper surface. The chamber is fed through an air duct connected to a fan (Hydrofarm Active Air 6 inch in-line fan) and air is permitted to escape the top surface of the table through 1.6mm diameter holes drilled on a grid with 19mm spacing in perpendicular directions, as shown in Fig. 3.3a-b.

Six 44.45mm diameter by 6.35mm thick disks were cut out of 60A durometer polyurethane (McMaster-Carr product number 8784K55) with measured Young's modulus $E = 5.85$ MPa and Poisson's ratio $\nu \approx 0.5$ through compression testing up to 13% strain. The friction coefficient between disks was measured by pulling a block (of known weight) fastened to a sheet of polyurethane across another sheet of the same material and measuring the horizontal force with a load cell. The mean friction coefficient from this experiment is approximately 0.6. This coefficient is used throughout the numerical analysis since neighboring disks appear to engage mostly static friction throughout the test. However, future work should address the quantitative sensitivity of the force inference results to this parameter as well as the appropriate selection between a static and dynamic friction coefficient. The underside of each disk is endowed with a shallow 38.1mm diameter by 1.19mm thick concentric cut to create a small plenum chamber, as shown in Fig. 3.3c. This allows the disks to

"float" on a frictionless bed of air on the top surface of the table and interact with one another through mechanical contact only. The top surface of each disk is endowed with a painted speckle pattern to enhance DIC results, as shown in Fig. 3.3b.

Two stiff wooden blocks are fastened to the top surface of the table to form a corner and the six disks are placed at rest in the corner in two rows of three, as shown in Fig. 3.3d. A stiff wooden impactor is then manually propelled toward the disks with a measured initial velocity of $v_x = -1.141\text{m/s}$, $v_y = -0.66\text{m/s}$ and negligible initial rotational velocity. Initial contact between the disks and the impactor occurs at an angle of approximately 27^o with respect to the center of the top right particle in Fig 3.3d. The entire impact event is captured with a Phantom v310 high-speed camera at 5000 frames per second. The impact and subsequent rebound of the impactor and all disks are monitored for 0.028 seconds to obtain the necessary input to the multi-objective optimization problem in Eq. (3.18).

A finite-element (FEM) model with the same initial conditions discussed above was created and analyzed in Abaqus/Explicit [75] to compare inferred inter-particle forces with the results of the multi-objective optimization problem. FEM was chosen to model the grains rather than DEM because FEM uses only material properties and the governing equations of continuum mechanics, making no assumption of contact law. Since our goal is to validate a method that makes no assumption of contact law in an experiment where we do not necessarily know the contact law, it is logical to use a validation method with the same features. DEM instead relies on a prescribed contact law (e.g., Hooke's or Hertz's law) and would likely require extensive calibration with experimental results to produce quantitatively accurate dynamics. The grain material is modeled using a 2D plane stress formulation with grain properties discussed above. The walls are modeled as rigid boundaries. The impactor is modeled as a stiff 2D linear elastic body. The Young's modulus of the impactor does not affect the final results so long as it is an order of magnitude higher than the grains' Young's modulus.

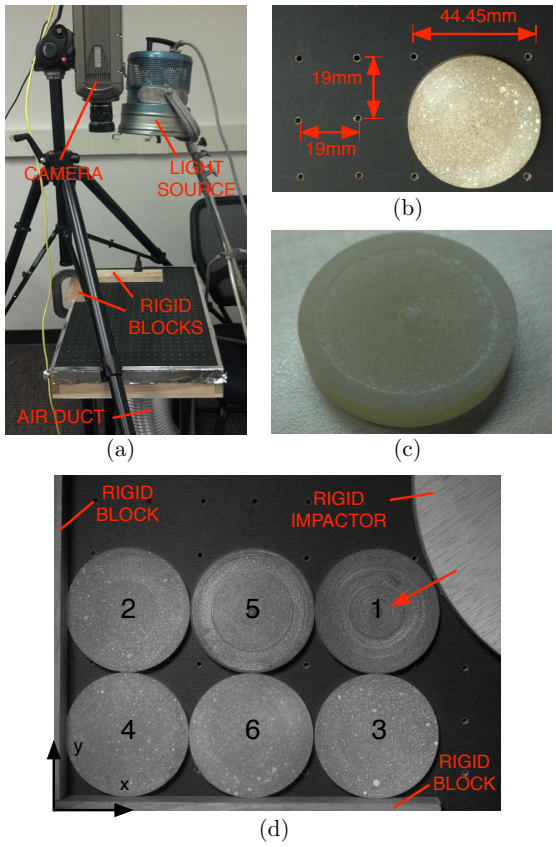

Figure 3.3: Experimental materials and setup. (a) Table setup with air duct connected to fan, rigid blocks fastened to table, camera and light source vertically over the area of interest. (b) Close-up view of table top and the top surface of a polyurethane disk with speckle pattern. (c) The underside of a polyurethane disk, showing plenum chamber for compressed air. (d) Experimental setup with 6 polyurethane disks and rigid impactor propelled at initial conditions $v_x = -1.141\text{m/s}$ and $v_y = -0.66\text{m/s}$. Particle labels will be used later and are in no meaningful order.

3.3.2 Experiment analysis

The DIC software VIC-2D [57] is used to calculate full-field intra-particle strains and velocities in each of the six grains in the experiment. Particle diameters are approximately 220 pixels in the 800x600 images captured at each time step. Subset size is chosen to be 15 pixels and subset step size is selected as 2 pixels, giving a ratio of particle diameter to subset size of approximately 15. Other DIC parameters such as prediction margin, confidence interval, and matchability are selected with default values of 0.02, 0.1, and 0.1, respectively. However, it is nearly impossible

to determine how the selection of these parameters influences the calculated strain values [76]. This is an area of ongoing research in the DIC community. Nevertheless, our parameter selection appears to give smooth, visually reasonable results for the displacement field within each grain. The influence of uncertainty in strain values on the results of a similar optimization problem was discussed briefly in [13], where it was shown that relative errors in strain values cause similar relative errors in force values. Future work on further assessing how changing some parameter values, such as subset size, influence the results presented here would be useful.

The ϵ_{xy} component of the strain field as measured using DIC and FEM is shown in Fig. 3.4 at four times during an impact event. The comparison illustrates an excellent agreement between DIC measurements and FEM results. Intra-particle stresses are obtained by using the full-field strains in a linear elastic plane stress formulation at each pixel. It is important to note that we could alternatively use grain boundary deformations to obtain volume-averaged grain strains (applying the divergence theorem to the definition of volume-averaged strain) before computing volume-averaged grain stresses with the linear elastic constitutive law. Material properties are taken as $E = 5.85$ MPa and $\nu = 0.5$ as mentioned above. Stresses are then averaged over each pixel within a particular grain, yielding the average stress needed in Eq. (3.14).

Particle edges and centroids are calculated at each time step (i.e., each movie frame) using a circular Hough transform in Matlab's image processing toolbox [77]. In particular, the Matlab function **imfindcircles** is used, which makes use of the techniques developed in [78] and [79].

The resulting centroids and radii are then used to find contacting particles: if the distance between two centroids is less than two times the radii of the corresponding particles, the particles are taken to be contacting with appropriate normal and tangent vectors. While the circular geometry of our grains makes this step of the analysis simple, the method is not restricted to circular particles.

Accelerations of the center-of-mass of each particle can be calculated in two ways: by summing and numerically differentiating intra-grain velocity fields calculated using VIC2D, or by twice numerically differentiating centroids obtained from the circular

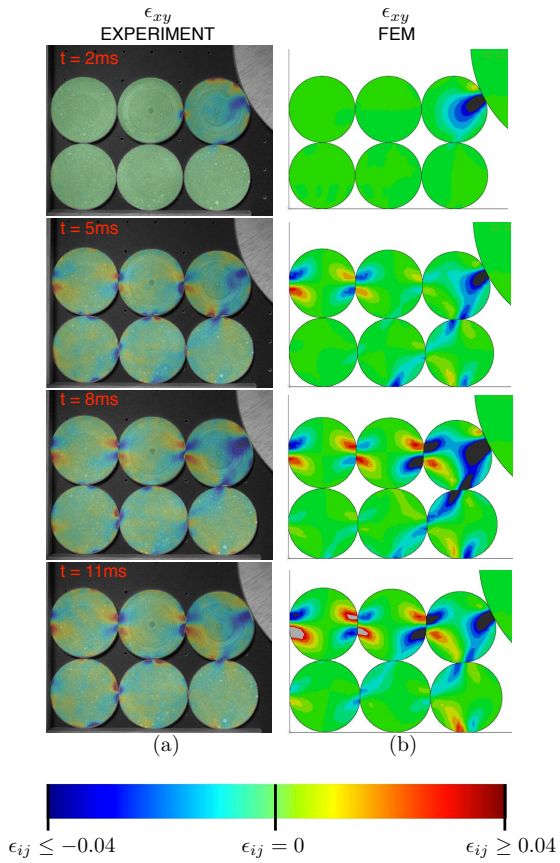

Figure 3.4: The ϵ_{xy} component of strain from (a) DIC and (b) FEM at four times during the impact event. All figures share a common scale. Strain values above and below the extreme values of the scale occur in small areas.

Hough transform. We use the latter approach to obtain the results presented in this chapter, although both methods produce very similar center-of-mass accelerations. While using the latter approach, we also employ a low-pass filter on the centroid and acceleration time series. The filter is a finite-impulse response filter with a Hamming window, provided by Matlab's signal processing toolbox. Filter order and normalized cutoff frequency are selected to maintain a signal to noise ratio greater than 10 for each acceleration time series, as done in other works [42].

3.3.3 Experiment results and FEM comparison

The optimization problem, Eq. (3.18), is solved at each time step using CVX [71] in MATLAB. The result of solving Eq. (3.18) is shown in Fig. 3.5 next to forces

calculated using the FEM model. It is important to use caution when comparing the forces calculated using the proposed method and the FEM model. The FEM model does not represent the *exact* forces in the experiment because the material model and initial and boundary conditions are approximate. However, the FEM model does provide an example of the force evolution at each contact point in an idealized experiment and should therefore capture major features of the force evolution (i.e., large peaks) and the appropriate order of magnitude. Integral terms in Eqs. (3.8) and (3.15) are neglected as they were assumed to be small for the observed particle accelerations. The results validate this decision.

The evolution of forces obtained using Eq. (3.18) shows excellent agreement with the FEM results in Fig. 3.5. Figs. 3.5a and 3.5b illustrate that force magnitudes and directions obtained using Eq. (3.18) qualitatively match those obtained from the FEM model. Fig 3.5d illustrates that most major features of the force evolution at each contact are captured using Eq. (3.18). The order of magnitude of all forces is also in excellent agreement, often differing by less than 20% from those obtained using FEM. Eq. (3.18) is clearly capable of extracting quantitative force information representative of the true physical state of the system of particles.

We also compared the calculated impulse imparted to each particle using the forces from Eq. (3.18) with those obtained from the high-speed images. The impulses obtained from Eq. (3.18) are calculated by numerically integrating all forces on a particular particle over the period of time in which they are in contact with neighboring bodies. The results are presented in Table 3.1 in terms of Δv obtained from Eq. (3.18) and those measured from high-speed images. Again, the agreement between the results of Eq. (3.18) and actual measurements is excellent in most cases. There are some slight deviations in the calculated and measured changes in velocity, likely due to experimental measurement error and the simplifying assumptions of the constitutive law.

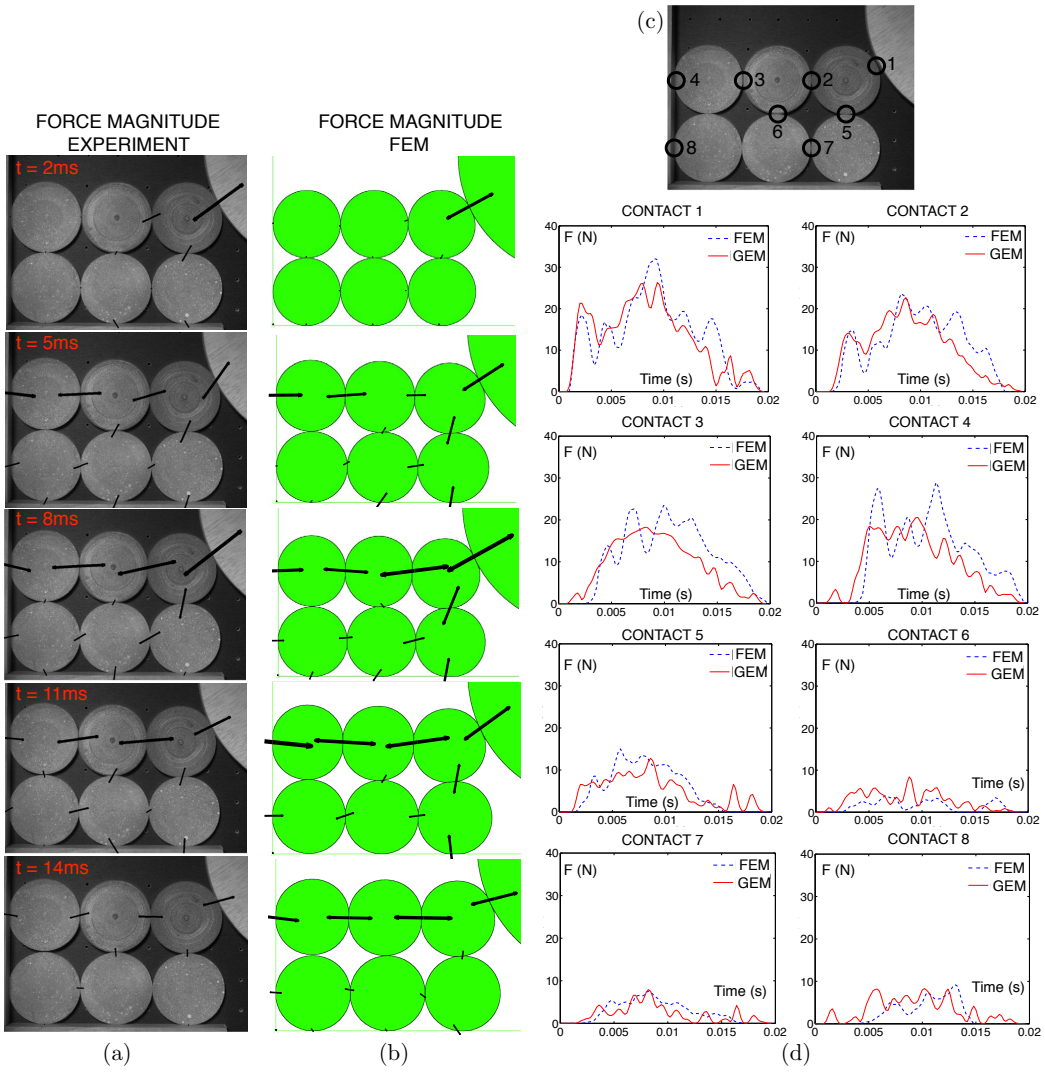

Figure 3.5: (a) Forces found using Eq. (3.18). Length and width of lines are proportional to force magnitude. (b) Forces found from the FEM model. (c) Eight contact point locations, chosen to include the major force chain and otherwise at random. (d) A comparison of force evolutions using Eq. (3.18) and the FEM model.

Table 3.1: Comparison of expected change in velocity obtained by dividing impulse obtained from Eq. (3.18) by particle mass and by direct measurement from high-speed video. All results are in m/s and particle numbers are those in Fig. 3.3d.

Particle	Δv_x Eq. (3.18)	Δv_x Measured	Particle	Δv_y Eq. (3.18)	Δv_y Measured
1	0.76	0.54	1	0.28	0.25
2	0.16	0.04	2	0.12	0.12
3	0.38	0.40	3	0.07	0.04
4	0.26	0.00	4	-0.01	0.00
5	0.51	0.47	5	0.18	0.09
6	0.23	0.21	6	0.11	0.00

3.4 Example 2: Application

This section contains a preliminary application of the proposed force inference method to the study of impact of an intruder on a model granular bed. This example is intended to demonstrate how the method may be used in practice in experiments more complex than the one illustrated in section 3.3. The section is presented in two steps: (1) experimental setup and (2) experimental results.

3.4.1 Experimental setup

The experimental setup is shown in Fig. 3.6. A 1.22m tall by 0.81m wide granular bed is prepared between a Plexiglas window and a sheet of PVC plastic. A small 1.11cm gap is provided between the Plexiglas and PVC to allow the 0.95cm thick grains to move without significant interference. The granular bed is composed of several hundred rubber grains made from polyurethane (E = 12MPa, $\nu \approx 0.5$, friction coefficient 0.6) dropped randomly into the gap. Two grain diameters were used to prevent crystallization: 2.54cm and 3.175cm.

Each dynamic experiment begins by dropping a 20cm steel intruder into the granular bed. Under the weight of gravity, the intruder accelerates to an impact velocity of approximately 2.4m/s in each of the experiments presented here. The entire impact event is captured with a high-speed Phantom v310 camera at 4500 frames per second.

3.4.2 Experiment analysis

As in the previous example, Vic2D is used to extract intra-particle strain fields and MATLAB's image processing toolbox is used to determine particle positions at each time step. The smallest particle diameters are approximately 72 pixels in the 800x600 images captured at each time step. Subset size is chosen to be 13 pixels and the subset step size is chosen as 2 pixels, giving a ratio of particle diameter to subset size of approximately 5.5 in the smallest particles. This ratio is lower than in the first example, implying that there may be larger uncertainty in the strains calculated in this case. However, without a systematic way of determining the influence of subset size on calculated strains, there is no way to quantify this additional uncertainty [76]. Nevertheless, parameter selection in this example also appears to give smooth, visually reasonable results for the displacement field in each grain. Other DIC parameters are chosen to be the same as in the previous example.

It is important to note that by using images of the prepared granular bed as reference images in Vic2D, we are implicitly ignoring prestress in the grains. The result of force inference therefore does not account for forces existing in the granular bed before impact. However, in dynamic experiments like those presented here, such pre-existing forces are likely negligible.

3.4.3 Experimental results

The inter-particle forces are once again obtained by solving Eq. (3.18) at each time step. An example of inter-particle forces inferred as a function of time are shown for one experiment in Fig. 3.7. A force-chain develops beneath the intruder at approximately 5ms into the experiment before it collapses at approximately 28ms. The emergence of a persistent force chain immediately beneath the intruder in these experiments agrees with past experiments that use photoelastic disks [42, 43]. In contrast to past experiments, the present work resolves individual force values at grain-grain and grain-intruder contact points.

Figure 3.8 shows inter-particle forces in the granular bed during an experiment

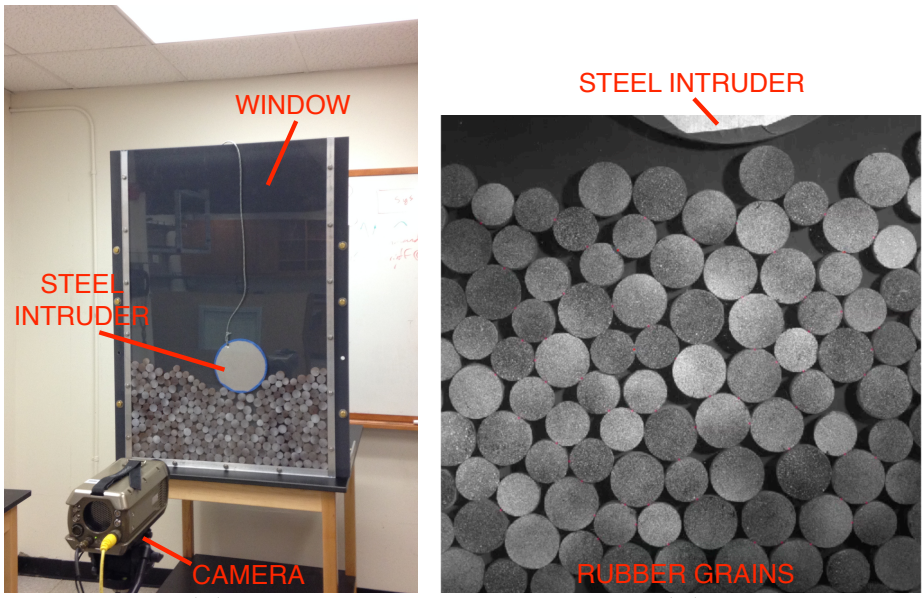

(a) (b)

Figure 3.6: Experimental setup. (a) A window featuring a piece of Plexiglas and a sheet of PVC plastic holding the 2D granular bed in place. A high speed camera is used to view the granular bed as it is impacted by a steel intruder. (b) A close-up of the steel intruder about to impact the granular bed at -2.4m/s.

with a different initial packing than that shown in Fig. 3.7. The response of the granular bed is clearly different in the two cases. The force response shown in Fig. 3.8 demonstrates the emergence of force chains, as in Fig. 3.7, but through different particles and branching in different directions. Such sensitivity to initial packing conditions is characteristic of granular media. This behavior is the reason that past research on force transmission and force chains has focused so extensively on the statistics of forces [31,80]. Similar statistics are expected to arise regardless of distinct local features of the response and may elucidate critical intrinsic behaviors of the material.

Figure 3.9 shows the vertical force on the intruder as a function of time in the experiments shown in Figs. 3.7 and 3.8. Both force responses demonstrate several peaks during the time in which a persistent force chain exists beneath the intruder. We attribute these peaks to repeated excitations of the existing force chain as the intruder's energy is sent into the granular bed along this path [42]. The excitations

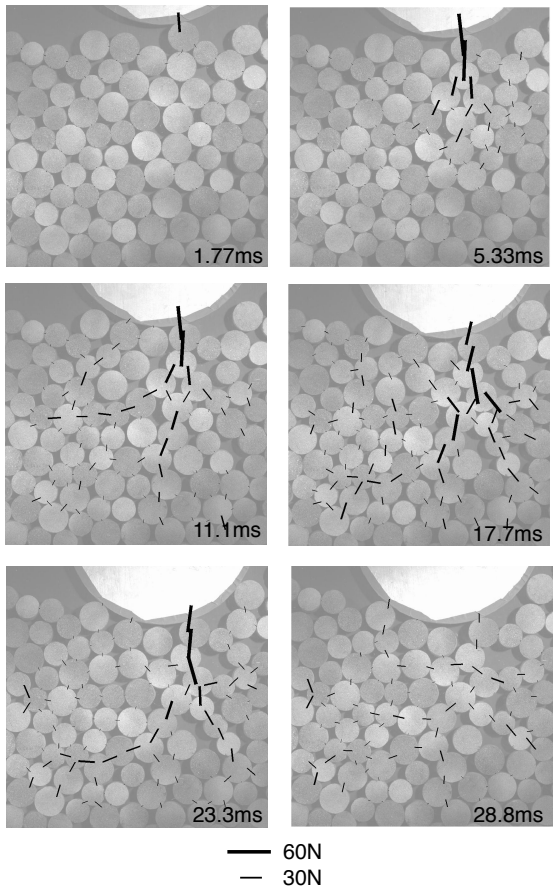

Figure 3.7: Inter-particle forces in the granular bed at six times during an impact event.

may be caused by repeatedly collapsing and restrengthening of the primary force chain as particles rearrange beneath the intruder. The primary force chain and its collapse is labeled for the curve pertaining to Fig. 3.7. In both experiments, the force response at early times is similar, while the force response at later times differs significantly.

A guiding question in the ongoing research into granular bed impact response is: Does the response of a granular bed to low-velocity impact admit any repeatable features indicative of intrinsic collective behavior of the grains? For instance, past work has indicated that the distribution of inter-particle forces evolves similarly during an impact event regardless of initial packing conditions [32]. In Fig. 3.10 we demonstrate another feature of the granular bed response that appears to be independent

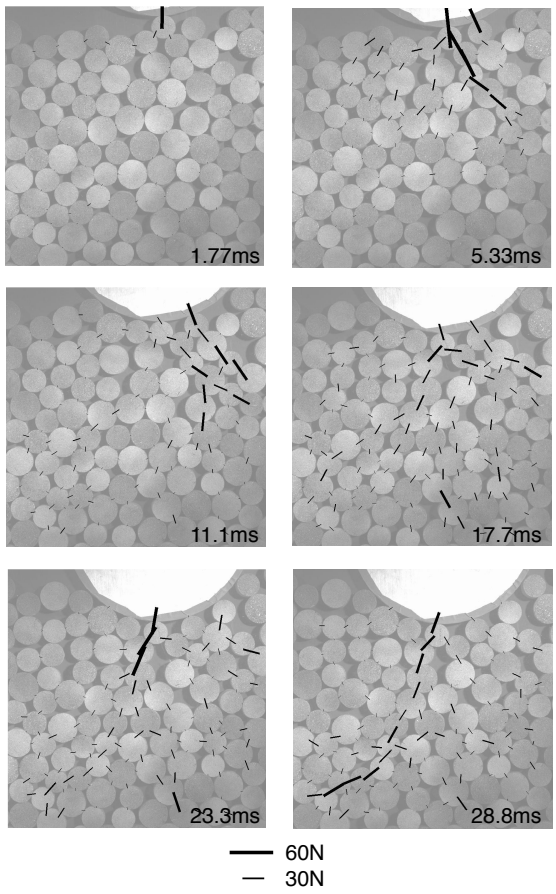

Figure 3.8: Inter-particle forces in the granular bed at six times during an impact event with an initial packing of the bed different from the experiment shown in Fig. 3.7.

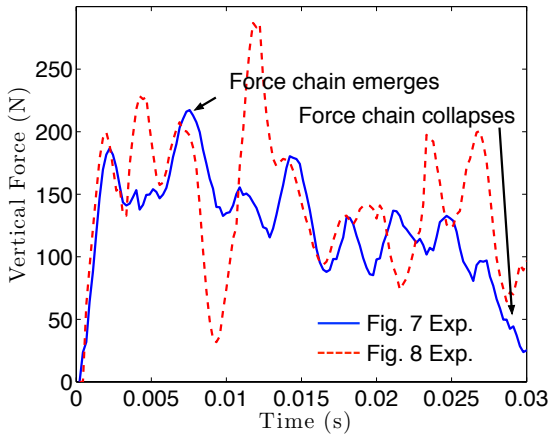

Figure 3.9: The vertical force felt by the intruder for the experiments shown in Figs. 3.7 and 3.8.

of initial packing conditions. The three curves in Fig. 3.10 represent the maximum force between two grains as a function of distance to the surface of the intruder in three experiments with three distinct initial packing conditions. Experiment 1 refers to the response shown in Fig. 3.7 and experiment 2 refers to the response shown in Fig. 3.8. All experiments have an intruder impact velocity of approximately 2.4m/s. Despite the emergence of force chains along different paths in each experiment, the maximum force as a function of distance from the intruder surface is very similar in each experiment. This suggests that, regardless of initial packing configuration, force chains are only able to transmit large loads a certain distance into a granular medium before the forces split into different paths and decay, a theory proposed in past work [21, 42]. This phenomenon, and other phenomena involving inter-particle forces are the subject of ongoing research and will be discussed in more depth in future work. GEM offers a valuable tool for investigating these questions regarding intrinsic material response.

3.5 Discussion

The force inference method proposed in this chapter has a number of advantages and disadvantages. Compared to photoelasticity [42, 43], the proposed method does not

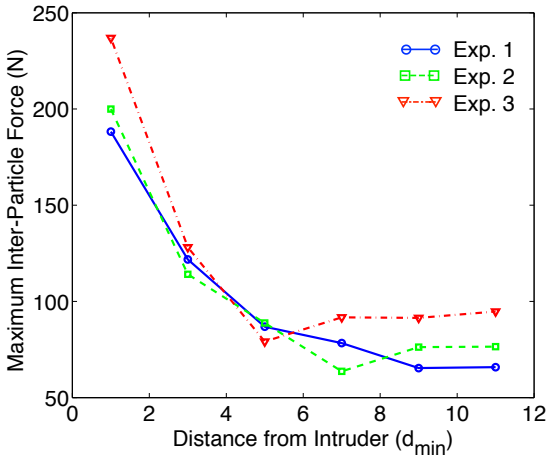

Figure 3.10: Maximum inter-particle force as a function of distance from the surface of the intruder for three experiments with distinct initial packings. Exp. 1 refers to Fig. 3.7. Exp. 2 refers to Fig. 3.8. An inter-particle force is considered to be a distance $nd_{\min}$ from the surface of the intruder if the contact point that it belongs to falls within a range of $nd_{\min}$ and $(n+1)d_{\min}$ away from the surface of the intruder, where $d_{\min}$ is the minimum particle diameter in the granular bed, 2.54cm.

place any inherent restriction on the grain material used in experiments. The material can be opaque and, for materials with linear constitutive laws, without any internal contrast. The grains can undergo plastic deformation so long as a constitutive law exists to obtain volume-averaged stresses from strain measurements. However, the grains' deformation must be of the appropriate order of magnitude to be captured by a technique for calculating strain. While the governing equations in photoelasticity can be modified for force inference in arbitrarily shaped grains, the proposed method requires essentially no modification, making it straightforward to apply when each grain has a different shape. A possible disadvantage of the proposed method is the requirement of volume-averaged strain calculation. For grains with non-linear constitutive laws, this requires calculating full-field grain strains, which remains a challenge in 3D dynamic experiments. However, in static experiments, strain fields can now be measured in realistic 3D quartz grains by using 3DXRD, offering the opportunity to apply the proposed method to such data sets in the near future [81].

While photoelasticity has been used to infer an approximate force averaged over tens of grain diameters in dynamic experiments [42], the proposed method has been

used to provide individual inter-particle forces. Thus, whereas photoelasticty has the advantage of being able to infer approximate forces across larger domains with more grains, the proposed method provides finer force resolution in local areas of interest. This resolution has previously only been demonstrated in numerical simulations using, for instance, the discrete element method [33] or FEM simulations [82]. The interest in resolving individual inter-particle forces is driven by a desire to understand the grain scale origin of the macroscopic response in many environments. For instance, in impact into a granular bed, researchers have long been interested in understanding frictional drag forces between the intruder and grains [32], the importance of inter-particle friction in energy dissipation within the granular bed [83], and the dynamics of force chains [42]. While numerical simulations can provide some of this information in idealized systems, experimental methods are the only way to study such physics in real systems. To date, the proposed method is the only one that has been used to infer quantitative inter-particle force values in such dynamic experiments.

Both photoelasticity and the proposed method have strengths and weaknesses. We are not advocating the use of one over the other in all scenarios. Rather, the proposed method may provide increased resolution and the ability to study different materials in certain experiments, while photoelasticity may prove to be more practical in other experiments.

3.6 Conclusion

In this chapter, we have proposed a new method for quantitatively inferring the evolution of inter-particle forces during a dynamic experiment on granular materials. The proposed method has been validated using a 2D experimental example in which inferred forces were compared to an FEM simulation. The results illustrate that the method can accurately infer the evolution of inter-particle forces at individual contact points in granular assemblies undergoing dynamic deformation. Preliminary results from experiments in which the method is applied to study impact in a granular bed demonstrate a potential application of the method: for unraveling the physics

of model granular materials in a variety of environments. Future applications of the method may include the study of granular flow, impact, and intruder dynamics with a variety of complex shaped grains and grain materials. The ongoing development of 3D imaging techniques may soon allow dynamic force inference in real powders and sands.

Chapter 4

Friction in inertial granular flows: Competition between dilation and grain-scale dissipation rates[1]

4.1 Introduction

Granular flows are ubiquitous in nature and technology [84]. Geologic events such as landslides and earthquakes occur because granular materials are able to transition from a solid state to a flowing state. Industrial processes such as hopper flows and powder transport involve the flow of food and pharmaceutical particles. Defense applications of brittle ceramics rely on the flow of a pulverized bulk material for energy dissipation. All of these applications demonstrate the need to understand granular flows at a fundamental level. Effective friction describes the shear resistance of a flowing granular medium and, in continuum simulations of these events, encodes information about grain-scale and contact-scale processes in a single parameter (see Fig. 4.1).

Granular flows can be classified as quasi-static, inertial (also referred to as dense), or rapid based on a dimensionless shear rate known as the inertial number [3,11]. The quasi-static behavior of granular media is typically modeled using critical state soil mechanics [85]. Rapid granular flows are similar in some respects to gases and have

[1]Adapted from R.C. Hurley and J.E. Andrade. Friction in inertial granular flows: Competition between dilation and grain-scale dissipation rates. *Granular Matter*, 17(3)287-295, 2015. DOI: 10.1007/s10035-015-0564-2

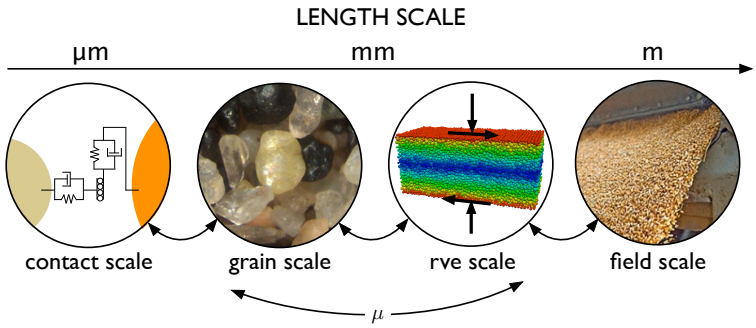

Figure 4.1: Friction encodes contact-scale and grain-scale information in a single parameter for continuum analysis.

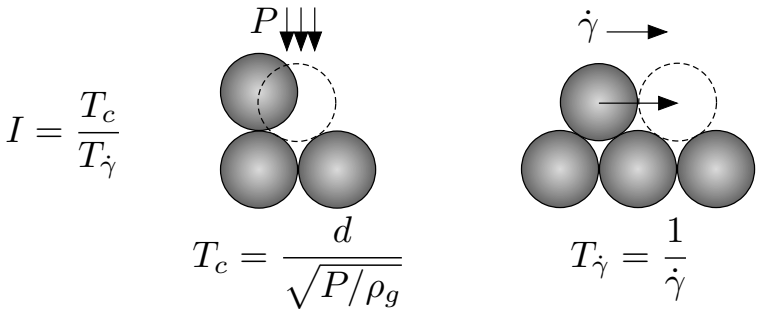

Figure 4.2: The two timescales associated with the inertial number, $I = T_c/T_{\dot{\gamma}}$.

therefore been extensively modeled using kinetic theories (e.g., [86, 87]). The intermediate regime of inertial granular flows has, unlike the quasi-static and rapid cases, eluded a unified modeling approach. Nevertheless, researchers have made important progress in understanding inertial granular flows in recent years.

The inertial flow regime corresponds to flows with an inertial number, $I = \dot{\gamma}d/\sqrt{P/\rho_g}$, between approximately 0.001 and 1. Here, $\dot{\gamma}$ is the shear rate ($|\dot{\boldsymbol{\gamma}}|$ in 3D), d is the grain diameter, P is the confining pressure, and ρ_g is the grain density. The inertial number is the ratio of the particle relaxation time $d/\sqrt{P/\rho_g}$ to the macroscopic shear time $\dot{\gamma}^{-1}$, as illustrated in Fig. 4.2 [11, 88]. This interpretation will be revisited when we develop a new friction relationship in section 4.2.

Researchers studying the inertial flow regime have developed empirical relationships between I and the steady state effective friction coefficient μ, the solid fraction ϕ, and the coordination number Z [4, 11]. For instance, da Cruz and co-workers pro-

posed a linear relationship between μ and I given by $\mu = a + bI$ for 2D simple shear flows, where a and b are empirical constants [11]. Jop and co-workers have proposed the nonlinear relationship $\mu = \mu_1 + (\mu_2 - \mu_1)/(I_0/I + 1)$ for 3D flows where μ_1, μ_2, and I_0 are empirical constants [4]. Jop and co-workers have also developed a constitutive law for predicting the stress distribution and flow profile for well developed granular flows, using the empirical friction law described above [4]. Other local and non-local continuum models have been developed for inertial flows. Each model takes advantage of one of the empirical friction laws described above [89, 90, 91]. These models have provided promising tools for predicting the behavior of granular media in a variety of flow configurations. However, investigative studies of inertial granular flows continue on a more basic level in an effort to understand the processes underlying frictional rate-dependence and the microstructure that develops during an inertial flow [2].

Da Cruz and co-workers studied the evolution of forces and anisotropy in inertial granular flows, showing that the anisotropy of the contact network can be explicitly related to friction [11]. Azema and Radjai similarly showed that a classical stress-force-fabric relation holds for inertial flows, demonstrating another link between friction and contact network anisotropy [1, 92]. Hatano and Kuwano [93] provided another interpretation of friction, using an energy balance equation to derive a steady state friction law very similar to that of rate-and-state theory. Jenkins has provided interesting links between friction and various attributes of inclined plane flows by extending hydrodynamic equations valid for rapid flows to the inertial regime [94]. Sun and co-workers have studied the energy characteristics of inertial granular flows and revealed a number of correlations between the friction coefficient and energy ratios [95]. All of these studies have provided valuable insight into the nature of effective friction in inertial granular flows.

In this chapter, we intend to contribute an additional interpretation of effective friction in granular flows by explicitly relating it to the inertial number, the coordination number, the solid fraction, and grain-scale dissipation rates. In section 4.2, we develop the friction relationship for steady state simple shear flows by performing an energy balance and a simple statistical analysis. We discuss the resulting picture of

friction as a competition between dilation and grain-scale dissipation rates. In section 4.3, we discuss numerical simulations of simple shear flows and present results showing the accuracy of the proposed friction relation. Simulation results are used to illustrate how the effective friction coefficient can be decomposed into contributions from grain-scale dissipation mechanisms. An analysis of the scaling of each of each term in the friction relationship elucidates the mechanisms controlling rate-strengthening. In section 4.4, we briefly compare our friction law with others proposed in past research. Finally, section 4.5 offers concluding remarks.

4.2 The friction law for simple shear

This section provides a derivation of our steady state friction relationship for simple shear flows. Fig. 4.3a illustrates such a well-developed flow in which the velocity profile in the direction of flow is quasi-linear.

Similar to past analyses of simple shear flows [93, 96], our starting point is the energy balance relationship

$$\frac{\mathrm{d}}{\mathrm{d}t}(T+U) = D_{ij}\sigma_{ji} - \Gamma \tag{4.1}$$

where T and U are the kinetic and potential energy densities, respectively, $D_{ij} = \partial u_i/\partial x_j$ is the velocity gradient tensor, and Γ is the dissipation rate per unit volume. In steady state simple shear flows, only one component of the velocity gradient tensor is nonzero ($D_{xy} = \dot{\gamma}$ in our case), and a time average of Eq. (5.10) yields

$$\overline{\dot{\gamma}\sigma_{yx}} = \overline{\Gamma} \tag{4.2}$$

where the $\overline{(\cdot)}$ indicates a time-average. Defining the effective friction coefficient as $\mu = \overline{\sigma}_{yx}/\overline{\sigma}_{yy}$ and assuming dissipation occurs only at grain contact points, Eq. (4.2) can be rewritten as

$$\overline{\dot{\gamma}\mu\sigma_{yy}} = \overline{\frac{N_c\langle\Gamma_c\rangle}{V}} \tag{4.3}$$

where N_c is the number of grain contacts in the system, V is the volume of the system, and $\langle \Gamma_c \rangle$ is the average dissipation rate at grain contacts in the system. We have made use of the fact that $\sum_{c=1}^{N_c} \Gamma_c = N_c \langle \Gamma_c \rangle$.

Numerical simulations to be described in the next section demonstrate that there is less than a 1% correlation in the fluctuations in the terms in Eq. (4.3). We will therefore assume averages of products can be written as products of averages and we will drop all time-averaging symbols. Variables in all following equations should be assumed to be time-averaged unless otherwise noted. Equation (4.3) becomes

$$\mu = \frac{N_c \langle \Gamma_c \rangle}{\sigma_{yy} \dot{\gamma} V} \tag{4.4}$$

We can further simplify Eq. (4.4) by noting: (1) the number of contact points is related to the coordination number by $N_c = Z N_p/2$ where N_p is the number of particles in the flow; (2) the number of particles can be related to the solid volume of grain material V_s by defining d such that $N_p(4/3)\pi d^3/8 = V_s$; (3) $V_s/V = \phi$ where ϕ is the solid fraction. The definition of d to satisfy (2) is consistent with d being the grain diameter in the case of monodisperse spheres, an average grain diameter in the case of polydisperse spheres, and a characteristic grain size in flows of complex shaped grains.

Combining the simplifications described above, Eq. (4.4) becomes

$$\mu = \frac{Z\phi}{I} \left(\frac{3\sqrt{\rho_g}}{\pi d^2 \sigma_{yy}^{3/2}} \right) \langle \Gamma_c \rangle \tag{4.5}$$

where the quantity $\pi d^2 \sigma_{yy}^{3/2}/(3\sqrt{\rho_g})$ is a pressure dependent term with units of energy dissipation rate. We therefore call this quantity $\tilde{\Gamma}$ and rewrite Eq. (4.5) as

$$\mu = \frac{Z\phi}{I} \frac{\langle \Gamma_c \rangle}{\tilde{\Gamma}} \tag{4.6}$$

Equation (4.6) is the most general form of our friction relationship. This expression makes no assumption of contact law or grain properties and only imposes the

restrictions that the flow is in steady state and energy dissipation occurs at contact points. This assumption does not prohibit the incorporation of material plasticity or fracture so long as such processes are assumed to arise because of contact between grains. In section 4.3, Eq. (4.6) will be applied to a specific contact law to discuss the results of numerical simulations.

Before discussing numerical simulations, we can provide a physical interpretation of Eq. (4.6). The coordination number Z and solid fraction ϕ convey the connectivity and compactness of the granular material. Both of these quantities, as well as $Z\phi/I$ taken together, can be assumed to decrease during shearing dilation, a process by which the packing expands at higher shear rates. In contrast, the grain-scale dissipation rates $\langle \Gamma_c \rangle$ may be expected to increase with shear rate due to higher inter-particle forces and collision velocities. The term $\tilde{\Gamma}$ remains constant when the confining pressure is held fixed.

The friction law in Eq. (4.6) therefore conveys a competition between dilation and microscopic dissipation rates. At low shear rates, $Z\phi/I$ is large and $\langle \Gamma_c \rangle / \tilde{\Gamma}$ is small. At high shear rates, $Z\phi/I$ is small and $\langle \Gamma_c \rangle / \tilde{\Gamma}$ is large. The result of this competition dictates whether the material is rate-strengthening or rate-weakening and highlights the role of dilation in effective friction. This interpretation of effective friction is closely related to the interpretation of the inertial number given in Fig. 4.2. The same time scales at work in the inertial number, those of confinement and macroscopic shear, are at work in determining the effective friction coefficient. The confinement time scale dictates the value of $Z\phi/I$ while the macroscopic shear time scale dictates the frequency and intensity of particle collisions.

4.3 Numerical simulations of simple shear

In this section, we discuss numerical simulations of simple shear flows. The simulations explore the behavior of the variables in Eq. (4.6) and elucidate the competing roles of dilation and microscopic dissipation rates during simple shear at a variety of imposed shear rates. The numerical code used for the simulations is first discussed,

followed by a discussion of results.

4.3.1 Description of code

We use a discrete element code [33] to study the various components of Eq. (4.6) in the inertial flow regime. Our simulations use a modified version of the granular module from the molecular dynamics code LAMMPS [97, 98]. Grains are modeled as spheres and interact with a Hertzian contact model. The normal force, $\boldsymbol{F}_n = \boldsymbol{F}_n^m + \boldsymbol{F}_n^v$, has a mechanical portion, $\boldsymbol{F}_n^m = R^* k_n \delta^{3/2} \boldsymbol{n}_{ij}$, and a viscous portion $\boldsymbol{F}_n^v = \sqrt{\delta} R^* m_{\text{eff}} \gamma_n \boldsymbol{v}_n$, where $R^* = \sqrt{R_i R_j/(R_i + R_j)}$, k_n is a spring constant, δ is the particle overlap, $\boldsymbol{n}_{ij}$ is a vector from the centroid of particle j to the centroid of particle i, $m_{\text{eff}} = m_i m_j/(m_i + m_j)$, γ_n is a damping coefficient, and $\boldsymbol{v}_n$ is the normal component of the relative velocity vector. The tangential force, $\boldsymbol{F}_t = \min(\boldsymbol{F}_t^m, \mu_p |\boldsymbol{F}_n|)$, has a mechanical portion, $\boldsymbol{F}_t^m = -\sqrt{\delta} R^* k_t \boldsymbol{\Delta}_s$, and a Coulomb slider enforcing $|\boldsymbol{F}_t^m| < \mu_p |\boldsymbol{F}_n|$ where k_t is a spring constant, $\boldsymbol{\Delta}_s$ is the accumulated tangential displacement of the grains, and μ_p is the inter-particle friction coefficient. The accumulated tangential displacement of the grains is frozen when grains are sliding. The constants k_n and k_t have units of force per area, consistent with the model presented in [99] and discussed in [97]. Thus, k_n and k_t are material properties that are independent of grain size and can be explicitly linked to grain properties if desired [100]. The constant γ_n prescribes a velocity-dependent coefficient of restitution of a binary collision, consistent with experiments [101, 102].

Simple shear is achieved by compressing approximately 10,000 bidisperse spheres between rough boundaries made of grains and moving the boundaries at a specified velocity in opposite directions, as shown in Fig. 4.3a. Grain radii are $(1 \pm 0.2)\tilde{d}$ where $\tilde{d}$ is specified. The height of the flow h is chosen such that $h/\tilde{d} \geq 20$. The rough boundaries are moved in the y direction to maintain a constant confining pressure throughout each simulation. Periodic boundary conditions are used in the x and z directions.

Confining pressure and grain stiffness is chosen such that $(k_n/\sigma_{yy})^{2/3} \geq 10^4$, mak-

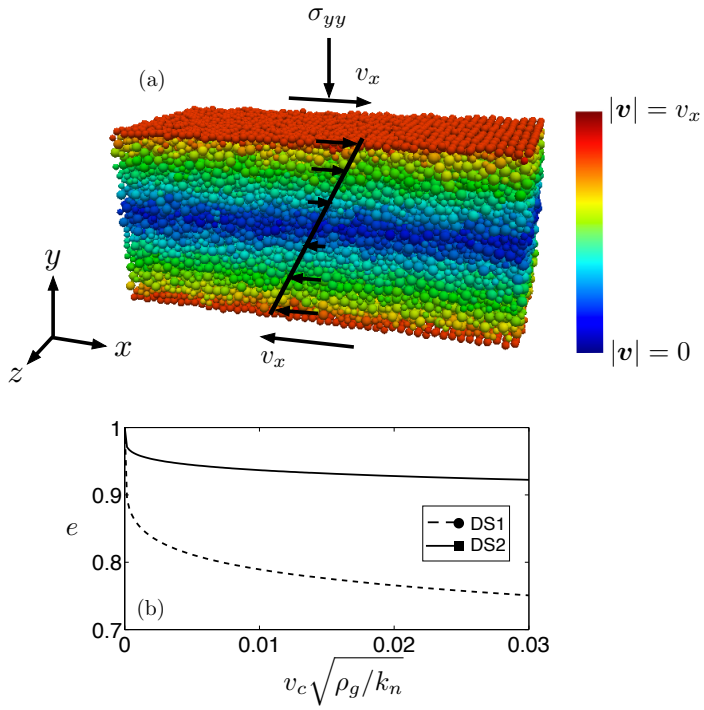

Figure 4.3: (a) A rendering of the simple shear flows featured in this paper. The top-most and bottom-most particles are used as rough boundaries. Colors indicate the magnitude of velocity, where v_x is the imposed wall velocity. (b) Coefficient of restitution e in a two-particle collision with normal velocity $v_c\sqrt{\rho_g/k_n}$ for data set 1 (--) and data set 2 (-).

ing the grains "rigid" as described in [11]. The parameter k_t is chosen to be 1/2 of k_n. Our primary data (DS1) set features 26 simulations across the inertial flow regime in which $\mu_p = 0.3$ and γ_n is set to prescribe the coefficient of restitution e shown as the dashed line in Fig. 4.3b. The inter-particle friction coefficient of $\mu_p = 0.3$ is chosen to provide a balance between lower values found in recent experiments [103] and slightly higher values used in recent simulations [1, 11]. We found that changing this inter-particle friction coefficient has minimal qualitative influence on the results, and mainly acts to shift the $\mu(I)$ curve up or down as reported in [11]. A secondary data set (DS2) features 18 simulations throughout the inertial flow regime with $\mu_p = 0.3$ and γ_n set to prescribe e as the solid line in Fig. 4.3b. This data set is only referred to in order to illustrate how grain viscoelasticity influences the material response. Unless otherwise specified, data should be assumed to belong to the primary data set. We leave an in-depth study of the effects of varying μ_p, γ_n, particle size distribution, and contact laws for future work.

Stress is measured using the equation

$$\sigma_{ij} = \frac{1}{V} \sum_{c=1}^{N_c} l_i^c f_j^c \tag{4.7}$$

where V is volume, c are contact point labels, N_c is the number of contacts in the material, l_i^c is a branch vector pointing from the centroid of particle j to the centroid of particle i, and f_j^c is the force vector from particle j to i [104]. The effective friction coefficient is computed using $\mu = \overline{\sigma}_{yx}/\overline{\sigma}_{yy}$, where averages are carried out over several thousand stress calculations once a steady state velocity profile has been reached.

Figure 4.4 compares μ and ϕ found in our simulations (using DS1) with available data from contact dynamics simulations [1] and 3D annular shear cell experiments [2, 3]. Our simulations show an excellent collapse with the other data sets both in terms of effective frictional response and solid fraction. The effective friction coefficient increases from its quasi-static value throughout the inertial flow regime, approaching a plateau at the transition to the rapid flow regime. The solid fraction decreases approximately linearly throughout the inertial flow regime from a maximum quasi-

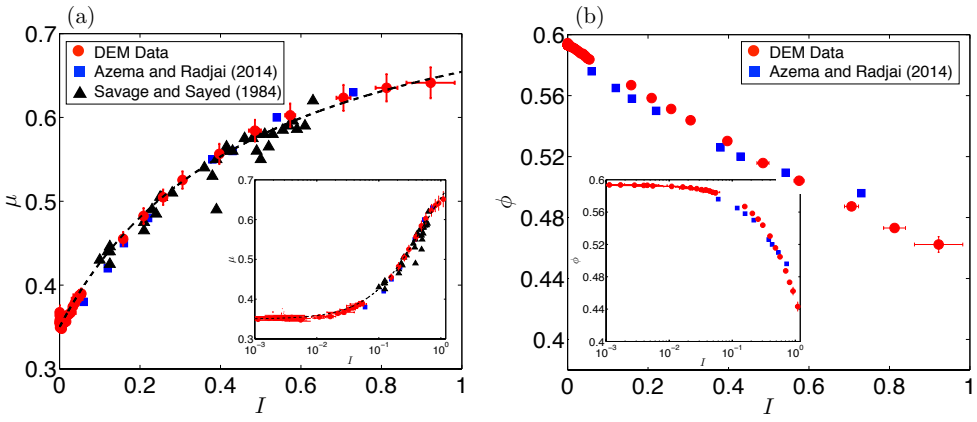

Figure 4.4: A comparison of (a) effective friction and (b) solid fraction from our simulations and available data sets taken from the literature. Blue squares are from contact dynamics simulations [1]. Black triangles are from 3D annular shear cell experiments [2,3]. Error bars indicate standard deviations in time of measured quantities. The dashed line shows the fit $\mu = \mu_0 + (\mu_1 - \mu_0)/(1 + I_0/I)$ from [4].

static value of 0.59.

In Fig. 4.4, as in all figures in this paper, plotted quantities are obtained as follows. First, a quantity of interest (e.g., coordination number) is computed at periodic times (approximately 5×10^4 times) once steady state flow has been achieved. The total strain over which quantities are extracted is taken such that averages over larger strains do not change the results. Next, the average of these quantities is used to obtain the plotted data points. Finally, the sample standard deviation is used to obtain the error bars. Error bars are typically omitted from inset plots for clarity.

4.3.2 Results: Validity of friction law

Figure 4.5 displays the effective friction coefficients for our primary data set computed using the friction relationship in Eq. (4.6) and the stress formula in Eq. (4.7). The figure demonstrates that the proposed friction law excellently approximates the effective friction coefficient throughout the inertial flow regime. We have confirmed that a similarly accurate fit exists for other grain properties.

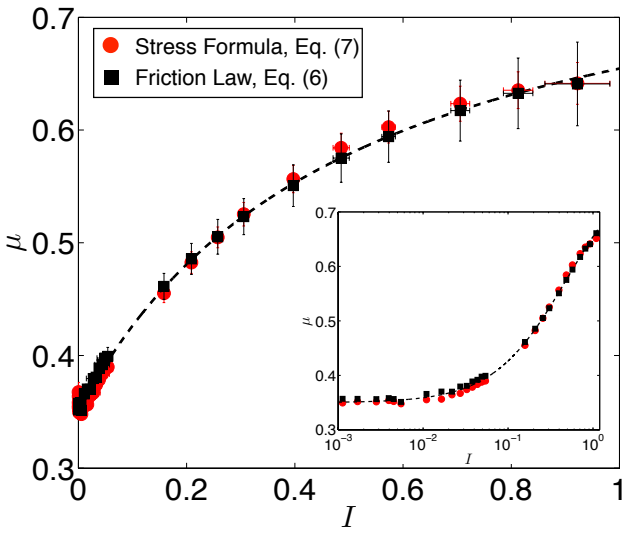

Figure 4.5: A comparison of the effective friction coefficient calculated from proposed friction relationship in Eq. (4.6) and the stress formula in Eq. (4.7).

4.3.3 Results: Grain-scale dissipation mechanisms

The contact law discussed in section 4.3.1 implies that Eq. (4.6) can be written as

$$\mu = \frac{Z\phi}{I}\,\frac{\langle \Gamma_n \rangle + \langle \Gamma_s \rangle}{\tilde{\Gamma}} \tag{4.8}$$

where $\langle \Gamma_n \rangle = \langle \boldsymbol{F}_n \cdot \boldsymbol{v}_n \rangle$ is the average viscoelastic dissipation rate, averaged over all contacts, and $\langle \Gamma_s \rangle = \langle |\boldsymbol{F}_t||\boldsymbol{v}_t| \rangle$ is the average dissipation rate from grain sliding, averaged only over sliding contacts. An additive decomposition of Eq. (4.8) into $\mu = \mu_n + \mu_s$ yields

$$\mu_n = \frac{Z\phi}{I}\,\frac{\langle \Gamma_n \rangle}{\tilde{\Gamma}} \quad \text{and} \quad \mu_s = \frac{Z\phi}{I}\,\frac{\langle \Gamma_s \rangle}{\tilde{\Gamma}} \tag{4.9}$$

The effective friction coefficient can thus be written in a form that clearly decouples contributions from the two grain-scale dissipation mechanisms, viscoelasticity and grain sliding.

Figure 4.6a illustrates how the two terms in Eq. (4.9) evolve throughout the inertial flow regime. At low shear rates, dissipation from grain sliding is the primary

contributor to effective friction. At higher shear rates, the contribution from grain sliding remains constant or declines as the contribution from viscoelastic dissipation becomes increasingly prominent.

4.3.4 Influence of material properties

In order to highlight how grain properties influence the relative contributions of microscopic dissipation mechanisms, results from the secondary data set are also shown in Fig. 4.6 (the solid lines). We recall that the primary data set (DS1) features the same grain properties as the secondary data set (DS2) except for a lower coefficient of restitution, as shown in Fig. 4.3b.

Figure 4.6a compares how the two terms in Eq. (4.9) evolve as a function of shear rate for each data set. Compared to DS1, DS2 features a larger effective friction contribution from grain sliding and a smaller contribution from viscoelasticity throughout most of the inertial flow regime. This occurs because grain viscoelasticity dissipates less energy for a given particle collision in DS2, leaving more kinetic energy in the system to be dissipated by grain sliding. Despite the difference in the grain-scale contributions to effective friction, both data sets feature similar values for μ until $I \approx 0.4$, as shown in Fig. 4.6b.

In past work [1,11], some researchers have ignored the influence of the coefficient of restitution e in shear flows because of the similarity of the effective friction coefficient when measured in systems using different values of e. Simulations are therefore often carried out using $e = 0$ [1]. The finding in Fig. 4.6 illustrates that although effective friction may be similar, the grain-scale dissipation mechanism responsible for friction is different in systems with different values of e. It may be interesting to explore the range of grain-scale behaviors that emerge from varying μ_p and e and the reason that they have such a minor influence on effective friction below $I \approx 0.4$. We leave such an investigation as future work.

Increasing or decreasing the inter-particle friction coefficient has the effect of shifting the effective friction curves in Fig. 4.6b up or down, respectively, but does not

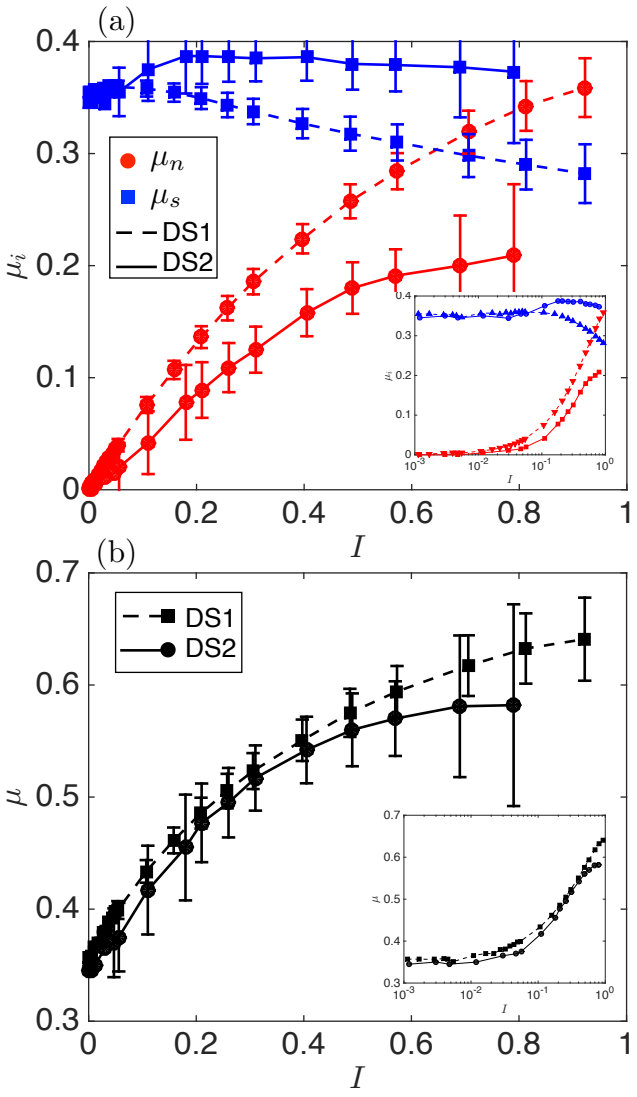

Figure 4.6: (a) The two terms $\mu_n = Z\phi\langle\Gamma_n\rangle/(I\tilde{\Gamma})$ and $\mu_s = Z\phi\langle\Gamma_s\rangle/(I\tilde{\Gamma})$ in the additive decomposition of effective friction given in Eq. (4.9) for the primary data set (--) labeled DS1 and the secondary data set (-) labeled DS2. (b) The total effective friction for the two data sets as a function of I. Error bars are omitted from inset plots for clarity.

significantly affect their shape or the magnitude of viscoelastic dissipation. Thus, the inter-particle friction coefficient primarily sets the baseline magnitude of effective friction while the coefficient of restitution controls the grain-scale contributions.

4.3.5 Results: Dilation and dissipation rates

The evolution of each term in Eq. (4.6) is shown in Fig. 4.7. Shearing dilation is captured in the evolution of Z, ϕ, and $Z\phi/I$ in Figs. 4.7a, 4.7b, and 4.7d, respectively. At low shear rates, Z and ϕ maintain maximum quasi-static values that depend upon properties such as the inter-particle friction coefficient and particle shape. For our primary data set, these quasi-static values are approximately 4 and 0.59 for Z and ϕ, respectively. As shear rates increase throughout the inertial flow regime, both Z and ϕ decrease as the material dilates. At all shear rates investigated, Z is well described by

$$Z \approx Z_1 + \frac{Z_2}{b + I} \tag{4.10}$$

and ϕ is well described by

$$\phi \approx \phi_{\max} - mI \tag{4.11}$$

where Z_1, Z_2, b, $\phi_{\max}$, and m are constants. These approximations hold for both data sets set discussed here and for simulations with different values of μ_p and γ_n, and different particle size distributions which we do not discuss here.

When combined, Eqs. (4.10) and (4.11) suggest the two scaling regimes of $Z\phi/I$ shown in Fig. 4.7d. The scaling $Z\phi/I \propto I^{-1}$ arises because Z and ϕ maintain quasi-static values at the low end of the inertial regime. The scaling $Z\phi/I \propto I^{-2}$ arises because Z and ϕ decrease in agreement with Eqs. (4.10) and (4.11) at higher shear rates. This decreasing contribution of $Z\phi/I$ in Eq. (4.6) reflects a decrease in both number of contact points and total solid fraction as shearing dilation increases. From an energy perspective, this decay conveys the decrease in internal surface area over which the material can dissipate energy.

While $Z\phi/I$ decreases with shear rate due to shearing dilation, average grain-scale

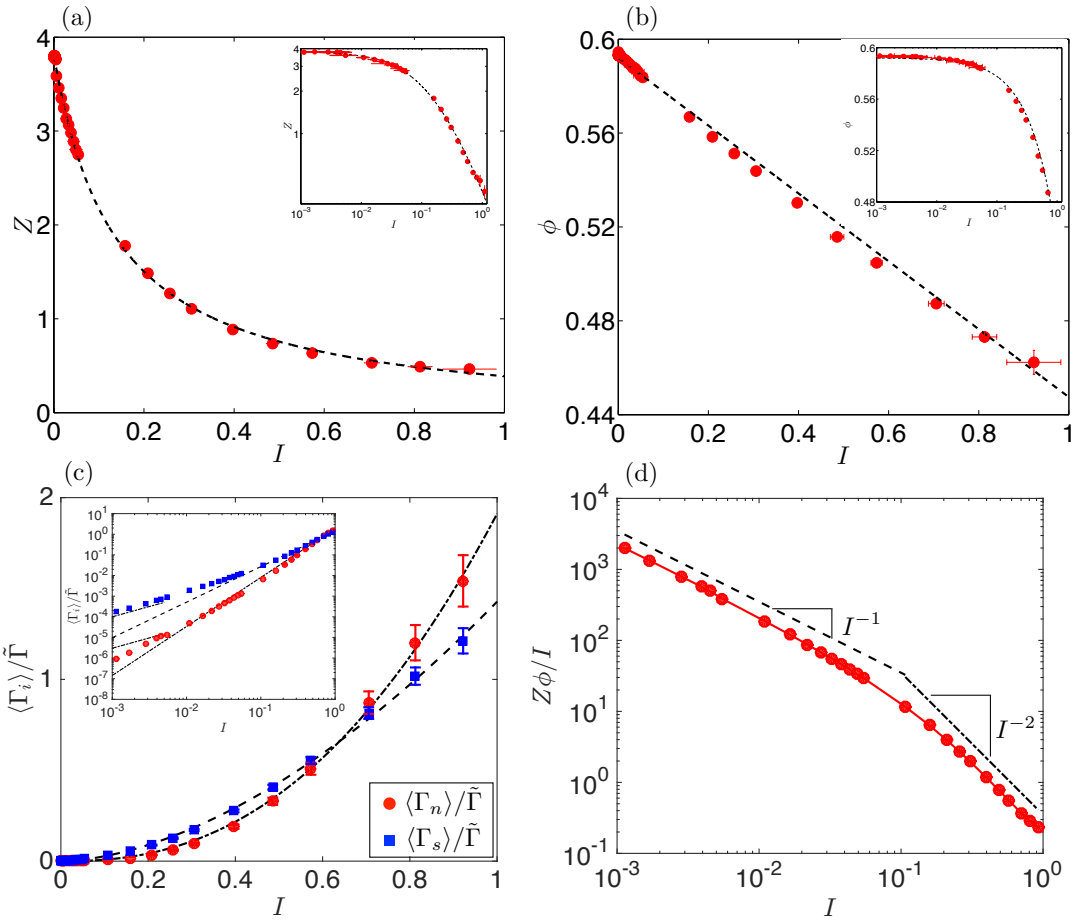

Figure 4.7: (a) The coordination number Z as a function of inertial number. The dashed line is the fit from Eq. (4.10). (b) The solid fraction ϕ as a function of inertial number. The dashed line is the fit from Eq. (4.11). (c) The average grain-scale dissipation rates $\langle\Gamma_n\rangle/\tilde{\Gamma}$ and $\langle\Gamma_s\rangle/\tilde{\Gamma}$ as a function of inertial number. The dashed lines are power-law fits, with $\langle\Gamma_n\rangle/\tilde{\Gamma} \propto I^{2.4}$ and $\langle\Gamma_s\rangle/\tilde{\Gamma} \propto I^{1.87}$ (d) The quantity $Z\phi/I$ as a function of inertial number. The dashed lines represent the two regimes of behavior in which $Z\phi/I \propto I^{-1}$ and $Z\phi/I \propto I^{-2}$. Error bars in (d) are negligibly small.

dissipation rates increase as shown in Fig. 4.7c. Both viscoelastic and grain sliding dissipation rates approximately follow a power-law dependence on I throughout the inertial flow regime, with $\langle \Gamma_n \rangle / \tilde{\Gamma} \propto I^{2.4}$ and $\langle \Gamma_s \rangle / \tilde{\Gamma} \propto I^{1.87}$, as shown in the inset of Fig. 4.7c. We generally expect $\langle \Gamma_n \rangle / \tilde{\Gamma}$ to scale at least as fast as I^2 for our chosen contact law because collision velocities scale approximately with I and viscous normal contact forces scale with collision velocity. Surprisingly, we also find $\langle \Gamma_n \rangle / \tilde{\Gamma}$ to scale at least as fast as I^2 when we impose sub-linear dependence of viscous normal forces on grain collision velocities. This likely occurs because the correlation between collision velocities and viscous normal contact forces implies that $\langle \Gamma_n \rangle \propto \overline{\langle \boldsymbol{F}_n^v \cdot \boldsymbol{v}_n \rangle} > \overline{\langle \boldsymbol{F}_n^v \rangle} \, \overline{\langle \boldsymbol{v}_n \rangle} \propto I^2$.

We have not found a similar argument for the scaling of $\langle \Gamma_s \rangle / \tilde{\Gamma}$ with shear rate, but we have always observed this term to scale slower than $\langle \Gamma_n \rangle / \tilde{\Gamma}$.

4.3.6 Results: Rate-dependent friction

When combined, the competing processes of shearing dilation and grain scale dissipation rates give rise to a rate-strengthening effective friction coefficient in our data sets, as shown in Fig. 4.6b. Rate-strengthening seems to occur because $Z\phi/I$ never decays faster than I^{-2} while $\langle \Gamma_n \rangle / \tilde{\Gamma}$ increases at least as fast as I^2 in the inertial regime.

Data sets using other values for μ_p and γ_n, as well as other simple contact laws (linear springs or nonlinear dependence of viscous normal force on collision velocity) have been investigated and yield similar results: $Z\phi/I$ never decays faster than I^{-2} and $\langle \Gamma_n \rangle / \tilde{\Gamma}$ always increases at least as fast as I^2 in the inertial regime. Velocity-strengthening therefore appears to be a generic system response for bidisperse spheres interacting with many viscoelastic contact models in the inertial regime. We have not observed a transition to rate-weakening friction at low shear rates as observed in some recent experiments [93]. Given the variety of grain properties and particle size distributions we have studied (but not discussed here), we suspect such a crossover, if it exists, to be caused by processes not captured by the current viscoelastic contact

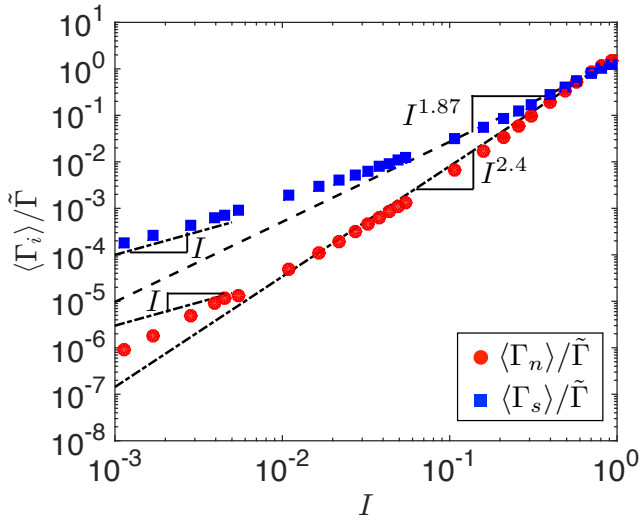

Figure 4.8: The inset of Fig. 4.7c, showing the average grain-scale dissipation rates as a function of inertial number on a log-log scale. The dashed lines illustrate the scaling of each dissipation rate discussed in the text, as well as the scaling proportional to I at the transition to quasi-static flow.

model, such as flash heating [93].

In Fig. 4.7c, dissipation rates approach 0 as $I \to 0$. This seems to suggest effective friction also approaches 0 as $I \to 0$; however, I appears in the denominator of Eq. (4.6). The scaling of dissipation rates with I is therefore the quantity controlling the approach to a quasi-static value of effective friction, not the absolute value of dissipation rates. To clarify this, we enlarge the inset of Fig. 4.7c in Fig. 4.8. At the transition from inertial to quasi-static flow, close to $I = 10^{-3}$, both dissipation rates trend toward scaling as $\langle\Gamma_i\rangle/\tilde{\Gamma} \propto I$. In the quasi-static regime below $I = 10^{-3}$, both dissipation rates reach this scaling. When this occurs, the effective friction coefficient reaches a quasi-static value and the strength is rate-independent. This transition is significant for understanding the onset of rate-dependent behavior and deserves further investigation in future work.

4.4 Discussion

The primary finding of sections 4.2 and 4.3 are: (1) effective friction in inertial granular shear flows can be interpreted as a competition between shearing dilation and grain-scale dissipation rates; and (2) rate-strengthening effective friction occurs in the inertial flow regime for many viscoelastic contact models and grain properties because grain-scale dissipation rates win the competition with shearing dilation. Although the first finding may seem intuitive, Eq. (4.6) provides a quantitative means of studying it. Equation (4.9) also provides a method of tracing macroscopic frictional energy loss down to the grain-scale.

The interpretation of steady state effective friction given in this chapter complements interpretations offered by past work [1, 11]. In these past works, researchers explicitly linked friction to the anisotropy of the contact network. An increase in normal force anisotropy was implicated in causing rate-strengthening. This interpretation offers an understanding of how the structural organization of grains may influence macroscopic frictional response. The interpretation of friction in the current chapter, however, makes no mention of structural organization and rather relies upon energy dissipation to explain changes in the macroscopic frictional response. That each interpretation can independently explain the change in effective friction as a function of shear rate is interesting and deserves further investigation.

Several other interesting behaviors were observed during the simulations carried out for this work. Many of these behaviors warrant future investigation. First, a similarity in the effective friction coefficient was observed for simulations using different values for the coefficient of restitution e. This similarity persisted even while differences were observed in the grain-scale contributions to friction (see Fig. 4.6). This behavior has been noted by previous authors [1, 11] and has not yet been explained. A number of interesting changes in behavior were also observed to occur near $I \approx 0.1$. Authors in [1] noted a number of topological transitions occurring at this shear rate. In this chapter, we observe the transition from $Z\phi/I \propto I^{-1}$ to $Z\phi/I \propto I^{-2}$ close to $I \approx 0.1$. We also observe a dramatic increase in the fraction

of sliding contacts at $I \approx 0.1$, regardless of the inter-particle friction coefficient μ_p used in simulations. Finally, we have observed that Eq. (6) holds for other contact laws and holds locally in layers of roughly constant inertial number in systems and flow configurations where the inertial number varies spatially. It would be useful to investigate such systems in more detail in future work to determine whether the quantitative results of this chapter persist.

4.5 Conclusion

We have presented a relationship between steady state effective friction, the inertial number, coordination number, solid fraction, and grain-scale dissipation rates in a granular shear flow. This relationship elucidates the rate- and porosity-dependent nature of effective friction in granular flows. Numerical simulations of simple shear flows have been used to illustrate how effective friction is furnished by grain-scale dissipation mechanisms. Rate-strengthening was seen to occur because terms encompassing shearing dilation decay more slowly with shear rate than terms encompassing grain-scale dissipation rates increase. We discussed how our findings compare with other interpretations of effective friction and mentioned several observations that warrant future investigation.

Chapter 5

Modeling dilative viscoplastic granular flows using SPH[1]

5.1 Introduction

Many geologic and industrial processes involve large deformation and flow of granular media such as soils, sands, powders, and pulverized brittle materials. Examples of such processes include landslides, debris flows, asteroid impact and cratering, bulk food transport, pharmaceutical processing, and ballistic impact of ceramics. Numerical models that can accurately simulate these processes are particularly important as predictive tools. However, the lack of well-established rheological relations for flowing granular media and the difficulty of representing arbitrarily large deformations with traditional numerical methods makes predictive modeling of these processes difficult.

The rheological behavior of flowing granular media is complex and has been a subject of study for many decades. Dry granular materials can exhibit solid-like, liquid-like, and gas-like behavior depending upon their excitation [8]. The ability of granular media to accommodate additional liquids and gases in their pore space further complicates their flow behavior [105]. Through decades of experimental and numerical investigation, the constitutive behavior of granular materials in several flow configurations has been elucidated (e.g., see [3, 4, 86, 88]). Particularly relevant to the present chapter, the rheology of dry granular flows has been examined in flows

[1]Adapted from R.C. Hurley and J.E. Andrade. Modeling dilative viscoplastic granular flows using SPH. *Under review.*

down inclined planes ([4,106]), simple shear flows [11], slow flows [85,107], and rapid flows [86]. Authors in [4] proposed a rate-dependent constitutive law for steady-state granular flows down inclined planes that has since proven to be an accurate framework for modeling large-scale processes such as impact cratering and granular column collapses (e.g., see [89, 108]). The rate-dependent nature of friction in this constitutive law has been examined analytically and shown to have grain-scale origins (e.g., see [10]). This rheological picture provides one of the most unifying frameworks for granular flows to-date. Below, we will adopt part of this constitutive law to model granular media in both their solid-like and liquid-like states.

Numerous numerical methods have been used for modeling granular materials. Depth-averaged finite difference methods have been a popular means of predicting geological flows for many decades (e.g., see [109]). The finite element method (FEM) has also been a popular tool for modeling both the quasi-static and dynamical flow of granular media using classical constitutive laws for soils and newer viscoplastic constitutive laws similar to the one developed by [4] (e.g., see [110] and [111]). More recently, the material point method (MPM) has been used to model the dynamic behavior of granular media using a Matsuoka-Nakai constitutive framework (e.g., see [112]). Smoothed Particle Hydrodynamics (SPH) has also been used to model the dynamic behavior of granular media using a Drucker-Prager plasticity law (e.g., see [113,114]). While each of these methods has strengths, mesh-free methods (MPM and SPH) are particularly attractive for very large and rapid material deformations since they do not require mesh-refinement. Furthermore, Lagrangian mesh-free methods that do not require a background grid (SPH) eliminate the convective effects of classical Eulerian formulations. Compared to Eulerian methods, SPH also offers precise interface definition and arbitrary resolution of flow details.

In this chapter, we present an SPH approach to modeling the flow of dry granular media. The novelty of our approach comes from combining an SPH formulation with a rate-dependent constitutive law similar to that proposed by [4] and used by [107]. We augment the rate-dependent constitutive law used in [4] and [107] with the rate of dilation and justify this approach with an analysis of the continuum energy

balance equation. We then present four qualitative and quantitative examples of the method. In particular, we model angle of repose tests, steady-state rate-dependent flows down inclined planes, granular column collapses on flat surfaces, and granular column collapses down inclined planes. These examples provide a partial validation of the method against experimental results and illustrate that, with some future work, it may be used as a predictive tool for many processes involving granular media. Compared to past mesh-free simulations of granular media (e.g., [112, 113, 114]), our method employs a new constitutive law well-suited for rate-dependent behavior, and is implemented three dimensionally.

The layout of this chapter is as follows. In section 5.2, we describe the balance and constitutive laws we use to model granular materials. We present our rate-dependent constitutive law in this section. We also show in this section that analyzing the continuum energy balance equation in the context of our constitutive law suggests a relationship between the rate of dilation and the effective friction coefficient. Section 5.3 is dedicated to describing the SPH framework used in this chapter and the algorithm we employ in our simulations. Four numerical examples of our method are described in section 5.4. We first discuss simulations of slumping granular media that demonstrate the ability of our method to produce angles of repose consistent with the friction angle used in our model. We then discuss simulations of inclined plane flows that illustrate the rate-dependent feature of our numerical method and the ability to match Bagnold velocity profiles. Next, we simulate granular column collapses on flat surfaces to illustrate the ability of our method to produce scaling laws of slump and runout consistent with those found experimentally. Finally, we compare time-dependent profiles of granular column collapses down inclined planes to demonstrate that our method accurately models the dynamic structure of granular flows. Section 5.5 offers a discussion of future work and concluding remarks.

5.2 Balance and constitutive Laws

5.2.1 Balance law

The governing balance law we will solve is the equation of momentum balance given by

$$\nabla \cdot \boldsymbol{\sigma} + \rho \boldsymbol{b} = \rho \boldsymbol{a} \tag{5.1}$$

where $\boldsymbol{\sigma}$ is the Cauchy stress tensor, ρ is the mass density, $\boldsymbol{b}$ is a body force, and $\boldsymbol{a}$ is the material acceleration.

5.2.2 Constitutive law

Defining the spatial velocity gradient as $\boldsymbol{L} = \nabla \boldsymbol{v}$, we introduce the strain rate tensor as

$$\boldsymbol{D} = \boldsymbol{L} + \boldsymbol{L}^T \tag{5.2}$$

where the T indicates a transpose. This definition differs by a factor of two from the classical definition in order to be consistent with [4], whose constitutive law we now adopt. We propose a stress tensor similar to that used for yield-stress (e.g., Bingham) fluids

$$\boldsymbol{\sigma} = -p\boldsymbol{I} + \frac{(\mu p + c)\boldsymbol{D}}{||\boldsymbol{D}||} \tag{5.3}$$

where p is pressure, $\boldsymbol{I}$ is the identity tensor, μ is the friction coefficient, c is cohesion, and $||\boldsymbol{D}|| = (\frac{1}{2}\boldsymbol{D} : \boldsymbol{D})^{1/2}$ is the second invariant of the strain rate tensor. This form of the stress tensor is similar to that proposed by [4], the difference being the addition of a cohesion term.

The second term in Eq. (5.3) can be identified as the shear stress tensor $\boldsymbol{\tau}$. When $\boldsymbol{D}$ is nonzero, the material flows with shear stress magnitude $||\boldsymbol{\tau}|| = \mu p + c$ where

$||\boldsymbol{\tau}|| = (\frac{1}{2}\boldsymbol{\tau} : \boldsymbol{\tau})^{1/2}$. Thus, the yield criterion is given by

$$||\boldsymbol{\tau}|| = \mu p + c \tag{5.4}$$

This form is again similar to the Drucker-Prager-type yield criterion in [4], but with the addition of cohesion.

The pressure in the granular material p is derived from an equation of state relating pressure to density. The general form of our equation of state is reminiscent of Tait's equation of state for nearly-incompressible fluids and is given by

$$p = \begin{cases} \kappa \left(\left(\frac{\rho}{\rho_0} \right)^{\gamma} - 1 \right) & \rho \geq \rho_0 \\ 0 & \rho < \rho_0 \end{cases} \tag{5.5}$$

where κ and γ are parameters and ρ_0 is the critical "jamming" density of the granular material, or the loosest packing density at which the material supports a nonzero stress state. We choose $\gamma = 3/2$ to produce a pressure-density relationship consistent with that found at the jamming transition for granular solids in [115]. The parameter κ is then constrained by the desired bulk modulus of the material through the relationship

$$K = \rho \frac{\mathrm{d}p}{\mathrm{d}\rho} = \begin{cases} \frac{3}{2}\kappa \left(\frac{\rho}{\rho_0} \right)^{3/2} & \rho \geq \rho_0 \\ 0 & \rho < \rho_0 \end{cases} \tag{5.6}$$

We use a rate-dependent and dilation-dependent friction coefficient given by

$$\mu = \mu_l + \frac{\mu_h - \mu_l}{D^*/||\boldsymbol{D}|| + 1} + \beta \tag{5.7}$$

where μ_l is the friction coefficient at low shear rates, μ_h is the asymptotic friction coefficient at high rates, D^* is a hardening or softening strain rate scale, and β is related to the rate of dilation by

$$\beta = \frac{\frac{1}{2}\mathrm{tr}(\boldsymbol{D})}{||\boldsymbol{D}||} \tag{5.8}$$

where $\mathrm{tr}(\boldsymbol{D})$ is the trace of $\boldsymbol{D}$. Note that the friction coefficient given by Eq. (5.7) can be either rate-strengthening or rate-weakening depending upon the chosen values of μ_l and μ_h. In granular materials, the classical choice is for a rate-independent or rate-strengthening friction coefficient. The theoretical link between the friction coefficient and the rate of dilation β is discussed next.

5.2.3 Theoretical link between friction and dilation rate

Several classical stress-dilatancy relationships link the frictional strength of a granular material to expansion or contraction (e.g., see [85]). One example is that of [116] who proposed a stress-dilatancy relationship of the form

$$\tan \phi'_m = \mu + \tan \psi \tag{5.9}$$

where ϕ'_m is the externally mobilized friction angle, μ is a frictional constant representing local internal material strength, and ψ is the dilation angle. Similar relationships have been used extensively in modeling quasi-static soil behavior (e.g., see [107]). Recently, a friction law linking dynamic friction and the rate of dilation has also been derived for simple shear of a granular material ([15]). As with the the derivation in [116], this friction law emerges from analysis of the governing energy balance equation. Below, we give a similar derivation but for three-dimensional flow of a material with a stress tensor given by Eq. (5.3). This derivation is meant to establish a theoretical justification for including the dilation rate β in Eq. 5.7.

Consider a granular material undergoing deformation at a rate $\boldsymbol{D}$. In the absence of heat sources, local energy balance requires that

$$\rho \dot{e} = \frac{1}{2}\boldsymbol{\sigma} : \boldsymbol{D} - \nabla \cdot \boldsymbol{q} \tag{5.10}$$

where e is the specific internal energy, $\boldsymbol{q}$ is the heat flux vector, and the factor of $1/2$ accounts for the difference between our definition of the strain rate tensor given in Eq. (5.2) and the classical definition. The strain-rate tensor can be decomposed into

volumetric and deviatoric components such that

$$\boldsymbol{D} = \boldsymbol{D}_v + \boldsymbol{D}_s \tag{5.11}$$

where $\boldsymbol{D}_v = \mathrm{tr}(\boldsymbol{D})\boldsymbol{I}/3$ and $\boldsymbol{D}_s = \boldsymbol{D} - \boldsymbol{D}_v$. Note that $\mathrm{tr}(\boldsymbol{D}_s) = 0$ by definition and thus $\boldsymbol{D}_v : \boldsymbol{D}_s = 0$. Substituting Eqs. (5.11) and (5.3) into (5.10) and rearranging, while ignoring cohesion, therefore yields

$$-\frac{1}{2}p\,\mathrm{tr}(\boldsymbol{D}) + \mu p||\boldsymbol{D}|| = \rho\dot{e} + \nabla\cdot\boldsymbol{q} \tag{5.12}$$

Solving this equation for μ yields

$$\mu = \frac{\rho\dot{e}}{p||\boldsymbol{D}||} + \frac{\nabla\cdot\boldsymbol{q}}{p||\boldsymbol{D}||} + \frac{\frac{1}{2}\mathrm{tr}(\boldsymbol{D})}{||\boldsymbol{D}||} \tag{5.13}$$

At steady-state, granular materials are observed to deform at constant volume ([4,85]) and constant average internal energy. Therefore, sufficiently long time averages of the first and third terms in Eq. (5.13) are zero at steady-state. The second term in Eq. (5.13) is then the rate-dependent steady-state friction coefficient represented by the first two terms in Eq. (5.7). The first term in Eq. (5.13) is a transient term associated with changes in internal energy of the material that accompany non-steady deformations (e.g., see [15]). In this work, we neglect representing this term in our friction law Eq. (5.7), making the assumption the time required for local internal energy equilibrium is sufficiently short that it does not play a significant role in the problems we wish to solve. Relaxing this assumption in future work will be discussed in section 5.5. The third term in Eq. (5.13) is identified as the rate of dilation of the material and is represented directly in Eq. (5.7).

In the examples presented in this chapter, the value of β is limited to $0 \leq \beta \leq 0.5$. This choice is meant to accomplish three things. First, these limits eliminate the influence of contraction of SPH particles ($\beta < 0$) near boundaries that can reduce friction and result in excessive slip. Second, we wish to capture the role of dilation in a similar manner to past models (e.g., see [107]), which use it primarily as a means

of enhancing the ultimate strength of a yielding granular material. Third, we wish to eliminate the effects of free-floating particles (i.e., those with $p = 0$) on the material dilation. One way of accomplishing this is with the current limits, which restrict β to values we perceive as more physically realistic and important as highlighted by past work ([107]). We will highlight the consequences of limiting β in this manner in section 5.3.4 and examples 1 and 2 in sections 5.4.1 and 5.4.2. We will discuss future extensions of our treatment of dilation in sections 5.3.4 and 5.5.

5.3 SPH formulation and algorithm

5.3.1 Kernel function and basic equations

We use SPH to model granular materials. Lagrangian particles of fixed mass represent a fixed mass of granular material and move according to the governing balance and constitutive laws. All field quantities are expressed at these particle locations using summation interpolants and a kernel function W with smoothing length h. The theory and history of SPH, a description of various kernel functions and summation interpolants, and a discussion of special considerations such as free surfaces and instabilities can be found in various monographs on the topic (e.g., see [117, 118, 119]). Here, we merely state that classical SPH has a number of attractive properties, including zero intrinsic dissipation, exact conservation of mass, momentum, angular momentum, energy, and entropy. We also note that resolution follows the chosen SPH particle mass.

We use the classical cubic spline kernel in all summation interpolants ([120])

$$W(r,h) = \frac{1}{h^3\pi} \begin{cases} 1 - \frac{3}{2}q^2 + \frac{3}{4}q^3 & 0 \le q < 1 \\ \frac{1}{4}(2-q)^3 & 1 \le q < 2 \\ 0 & q \ge 2 \end{cases} \tag{5.14}$$

where $q = r/h$ and $r = |\boldsymbol{x}_a - \boldsymbol{x}_b|$ is the distance between two particles labeled a and b. Equation (5.14) is normalized for three dimensions since all simulations in this

chapter are three-dimensional. One-dimensional and two-dimensional normalizations can be found elsewhere ([117]). Alternative higher-order kernels may be implemented in the future to reduce instabilities (e.g., see [121]), but were not required for the examples presented here. The smoothing length h is kept constant in this work since the modeled granular media is fairly incompressible. The length h is chosen to be 1.2 times the spacing of SPH particles when the granular material is in its loosest packing state. The fairly incompressible nature of the material prevents significant particle concentrations that might cause instabilities discussed in other works (e.g., see [122]).

The basic SPH interpolants used throughout this work include the summation interpolant for a field variable f at a particle location a given by (e.g., see [117])

$$f_a = \sum_b f_b \frac{m_b}{\rho_b} W(r,h) \tag{5.15}$$

and the interplant for the first derivative of a field variable, such as the pressure, given by (e.g., see [123])

$$\nabla p_a = -\sum_b m_b \rho_a \left(\frac{p_b}{\rho_b^2} + \frac{p_a}{\rho_a^2} \right) \nabla W(r,h) \tag{5.16}$$

where m is mass and $\nabla W(r,h) = (\boldsymbol{x}_a - \boldsymbol{x}_b)F$, F being a scalar symmetric function in a and b.

5.3.2 Density

We use the basic SPH equation for density with a Shepard filter applied at each time step. For particle a, we first compute ([117])

$$\tilde{\rho}_a = \sum_{b \in N} m_b W(r,h) \tag{5.17}$$

where the set N includes neighboring particles in the support domain of a as shown

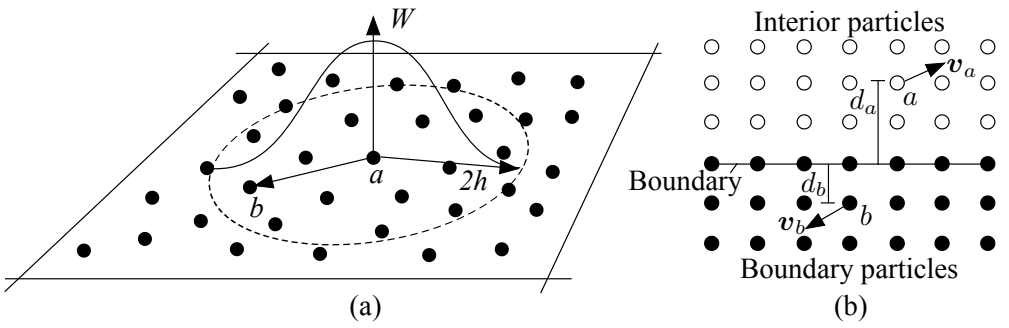

Figure 5.1: (a) Illustration of the smoothing kernel W with compact support of radius $2h$ about particle a. (b) Interior particles interacting with boundary particles, which are given artificial velocity.

in Figure 5.1a. We then apply the Shepard filter to obtain

$$\rho_a = \frac{\sum_{b \in N} m_b W(r,h)}{\sum_{b \in N} \frac{m_b}{\rho_b} W(r,h)} \tag{5.18}$$

This filter corrects particle deficiencies near free surfaces and boundaries and is equivalent to modifying the kernel to satisfy the partition of unity

$$\sum_{b \in N} \frac{m_b}{\rho_b} W(r,h) = 1 \tag{5.19}$$

We note that we have also employed the more common and efficient free surface density formulation proposed by [124]. While we obtain similar results in many cases using this formulation, we use Eq. (5.18) instead in order to retain high accuracy in density near the free surfaces. Future work may find this to be unnecessary.

5.3.3 Equation of state

After the density ρ_a at each particle has been computed using Eq. (5.18), pressure is calculated by direct application of Eq. (5.5).

5.3.4 Equation of motion

To update SPH particle locations, we discretize the momentum balance relationship Eq. (5.1) to give

$$\boldsymbol{a}_a = \rho_a \sum_{b \in N} \left(\frac{\boldsymbol{\sigma}_a}{\rho_a^2} + \frac{\boldsymbol{\sigma}_b}{\rho_b^2} \right) \nabla W(r,h) + \boldsymbol{b} \tag{5.20}$$

where $\boldsymbol{\sigma}$ is given by Eq. (5.3). In computing Eq. (5.3) before the calculation of Eq. (5.20), the strain rate tensor $\boldsymbol{D}$ must be calculated using Eq. (5.2) and the velocity gradient computed by

$$\boldsymbol{L}_a = \sum_{b \in N} \frac{m_b}{\rho_b} (\boldsymbol{v}_b - \boldsymbol{v_a}) \otimes \nabla W(r,h) \tag{5.21}$$

The value of p used in $\boldsymbol{\sigma}$ is given by applying the equation of state to the current density computed using Eq. (5.18). When rate-dependent friction is employed, the value of μ used in $\boldsymbol{\sigma}$ is computed with Eq. (5.7) applied to the particle velocities at the last time step.

When the rate of dilation β is included in calculating the value of μ from Eq. (5.7), β should be calculated by computing the third term in Eq. (5.13) for each particle. Unfortunately, doing this from SPH continuum fields in a simulation with arbitrary resolution (particle size and time step) may introduce artifacts due to temporal fluctuations in $\boldsymbol{D}$ that are time-step-dependent and spatial fluctuations in $\boldsymbol{D}$ that are particle-size-dependent. A more appropriate approach that recognizes β as arising from processes occurring "within" each SPH particle (i.e. inherently below the resolution of the continuum method) would be to evolve the rate of dilation β of each SPH particle by it's own evolution equation. This could be done with a source-decay differential equation that increases β due to a source (i.e. rapid change in strain rate of the particle) and allows β to decay to zero as a function of strain when strain rate is roughly constant. For example, such an evolution equation could take the form

$$\frac{\mathrm{d}\beta}{\mathrm{d}\epsilon_s} = -\frac{\beta}{\epsilon_s^*} + S \tag{5.22}$$

where ϵ_s is total strain, ϵ_s^* is a scale of decay, and S is a source term. This method for evolving β may be the focus of future work and may embrace a hierarchical multiscale approach like that proposed in [125]. However, since data to calibrate this method are lacking in the literature and since the present chapter is more focused on qualitative demonstration of the SPH framework and constitutive laws, we use the former approach of computing β directly from the SPH $\boldsymbol{D}$ field. We note that this choice introduces a few numerical artifacts into the solution. Most importantly, β is not seen to be identically zero when averaged during steady-state flows like those encountered in example 2 in section 5.4.2, primarily because of fluctuations in $\boldsymbol{D}$ due to SPH particle disorder, the choice of ignoring data outside the limits $0 \leq \beta \leq 0.5$, and the finite non-local smoothing effect employed in SPH. We will discuss this topic and needed future work more in sections 5.4.2 and 5.5.

5.3.5 Boundary conditions

In all simulations shown in this chapter, SPH particles are used to represent solid boundaries. Figure 5.1b shows a configuration of these "boundary" particles relative to the "interior" particles comprising the material of interest. The density of boundary particles is evolved using Eq. (5.18) with a summation over all neighboring particles, including those on the boundary and interior. Interior particles similarly use all neighboring particles in their density calculation. Interior particles also use all neighboring particles in their velocity gradient and stress tensor calculation. A basal friction coefficient μ_b may be used in place of the first two terms in Eq. (5.7) when an interior particle interacts with a boundary particle.

Boundary particles are given an artificial velocity when interacting with interior particles in order to simulate a smooth velocity gradient across the boundary. As discussed in [121], when interacting with interior particle a, a boundary particle b will have an artificial velocity of

$$\boldsymbol{v}_b = (1-\beta)\boldsymbol{v}_a + \beta \boldsymbol{v}_{\mathrm{w}} \tag{5.23}$$

where $\boldsymbol{v}_{\mathrm{w}}$ is the imposed velocity of the boundary and

$$\beta = \min\left(\beta_{\max}, 1.0 + \frac{d_b}{d_a}\right) \tag{5.24}$$

We choose a value of $\beta_{\max} = 1.5$, consistent with past work ([113, 121]). The lengths d_b and d_a are shown in Fig. 5.1b.

As discussed in [113] and [126], the artificial velocity of boundary particles is insufficient to provide a no-slip condition; artificial stress values must also be assigned to boundary particles. In the present work, we do not assign artificial stress values to boundary particles and instead directly compute the stress values of boundary particles as we do with interior particles. The effect of this is to reduce the shear stress gradient for interior particles close to boundaries, thus allowing a certain about of slip across the boundary. We note that this choice does not reduce the density, pressure, or velocity gradient of interior particles near the boundary since these quantities are computed by directly including boundary particles in the appropriate summations. Boundary slip is a key feature of granular systems that distinguishes them from idealized fluid systems. Future work may compare our boundary condition with that obtained by imposing a no-slip condition in various scenarios. An alternative to both the present approach and the no-slip approach used in [113] would be to assign an artificial stress value to boundary particles, the value of which is between the value computed by evolving this quantity directly and the average stress value that would be assigned artificially from interior particles. In the present work, we simply quantify the amount of boundary slip in an example of inclined plane flow.

There are several disadvantages of representing boundaries using real SPH particles. One disadvantage is the inability to represent curved surfaces when the simulation resolution is low. Another disadvantage is the potential for interior SPH particles to penetrate a boundary composed of SPH particles. We have found that modeling boundaries using real SPH particles with the same parameters as interior particles sometimes permits penetration of SPH particles into the boundary. One solution to this problem was proposed by [127], who modified particle velocities by an average of

velocities nearby. To avoid modifying bulk dynamics, we instead choose to alter the parameter ρ_0 used in calculating the pressure of boundary particles only. We set ρ_0 to approximately 3% below the initial packing density of boundary SPH particles in order to create a higher pressure p of stationary boundary particles and thus a higher pressure gradient for interior particles that interact with the boundary. This modification is not performed on interior particles, whose value of ρ_0 is maintained at the initial packing density. The modification of the boundary ρ_0 value slightly decreases the pressure of the interior particles closest to the boundary. Bulk dynamics are not noticeably affected; the modification only serves to increase the pressure gradient of interior particles closest to the boundary and therefore prevent penetration of interior particles through boundary particles. We illustrate this effect in section 5.4.1.

5.3.6 Time integration

We use a Velocity Verlet time integration scheme equivalent to the time-synchronized Leapfrog method. This symplectic integrator has been shown to conserve momenta and energy, making it particularly attractive with SPH which possesses conservation properties ([117]). This approach involves the following updates for particle a's position and velocity

$$\boldsymbol{x}_a^{n+1} = \boldsymbol{x}_a^n + \boldsymbol{v}_a^n \Delta t + \tfrac{1}{2}\boldsymbol{a}_a^n \Delta t^2 \tag{5.25}$$

$$\boldsymbol{v}_a^{n+1} = \boldsymbol{v}_a^n + \tfrac{\boldsymbol{a}_a^n + \boldsymbol{a}_a^{n+1}}{2}\Delta t \tag{5.26}$$

As an intermediate step, the half-step velocity can be written as

$$\boldsymbol{v}_a^{n+1/2} = \boldsymbol{v}_a^n + \frac{\boldsymbol{a}_a^n}{2}\Delta t \tag{5.27}$$

The acceleration $\boldsymbol{a}_a^{n+1}$ is then computed using Eq. (5.27) and $\boldsymbol{x}^{n+1}$. The precise update steps are described in Algorithm 1 below. We note that all field quantities $\rho, p, \boldsymbol{D}$, and $\boldsymbol{\sigma}$ are computed at each time step rather than their values being updated

rom previous time steps. In this manner, the procedure is simpler than traditional implementations of plasticity, which require a return mapping algorithm. The absence of a mesh eliminates the need for a mesh-updating, re-meshing, or mesh-mapping step characteristic of finite element or material point method implementations.

The time-step Δt must be chosen to satisfy a Courant condition, a limit imposed by maximal force, and a viscous diffusion condition (see [121,123]). These conditions amount to

$$\Delta t \leq \min\left(0.25\frac{h}{c_a}, 0.25\frac{h}{|\boldsymbol{f}_a|}, 0.125\frac{h^2\rho_a}{\mu_a p_a + c_a}\right) \tag{5.28}$$

where $c_a = \sqrt{K_a/\rho_a}$ is the bulk sound speed and the last condition emerges from analyzing the viscous condition discussed in [123] and [121]. In practice, some trial and error may be necessary to ensure the time-step satisfies these conditions, particularly the second condition since maximum particle accelerations may not be known *a priori*.

Algorithm 1 Velocity Verlet time step procedures for SPH simulation.

1. Begin with fixed particle mass m_a, particle positions $\boldsymbol{x}_a^n$, velocities $\boldsymbol{v}_a^n$, and accelerations $\boldsymbol{a}_a^n$ from last time step, and constants $\beta, \rho_0, \gamma, \mu_l, \mu_h, D^*, c, \mu_b, h$.
2. Compute updated particle positions $\boldsymbol{x}_a^{n+1}$ and partially updated particle velocities $\boldsymbol{v}_a^{n+1/2}$ using $\boldsymbol{a}_a^n$ and Eqs. (5.25) and Eqs. (5.27).
3. Perform intermediate steps to obtain $\boldsymbol{v}_a^{n+1}$.
   (a) Compute density ρ_a^{n+1} using Eq. (5.18) and $\boldsymbol{x}_a^{n+1}$.
   (b) Compute pressure p_a^{n+1} using Eq. (5.5) and $\boldsymbol{x}_a^{n+1}$.
   (c) Compute strain rate tensor $\boldsymbol{D}_a^{n+1}$ using $\boldsymbol{x}_a^{n+1}, \boldsymbol{v}_a^{n+1/2}$ and Eqs. (5.2) and (5.21).
   (d) Compute friction coefficient μ_a^{n+1} using $\boldsymbol{D}_a^{n+1}, \boldsymbol{x}_a^{n+1}, \boldsymbol{v}_a^{n+1/2}$ and Eqs. (5.7)-(5.8).
   (e) Compute stress tensor $\boldsymbol{\sigma}_a^{n+1}$ using $\boldsymbol{x}_a^{n+1}, \boldsymbol{v}_a^{n+1/2}$ and Eq. (5.3).
   (f) Compute particle acceleration $\boldsymbol{a}_a^{n+1}$ using $\boldsymbol{x}_a^{n+1}, \boldsymbol{v}_a^{n+1/2}$ and Eq. (5.20).
   (g) Compute updated velocity $\boldsymbol{v}_a^{n+1}$ using Eq. (5.26).
4. Set $\boldsymbol{x}_a^{n+1}, \boldsymbol{v}_a^{n+1}, \boldsymbol{a}_a^{n+1}$ to $\boldsymbol{x}_a^n, \boldsymbol{v}_a^n, \boldsymbol{a}_a^n$ and $n+1$ to n and return to Step 2 for next time step.

5.4 Examples

This section provides several demonstrations of the SPH algorithm applied to modeling granular media. Qualitative and partial quantitative comparisons with existing experimental data are provided. The major findings of each example are: (1) for a given friction coefficient μ, the method produces an angle of repose consistent with classical theory; (2) the rate-dependent feature of the friction law produces flow profiles in inclined plane settings that are consistent with Bagnold's theory; (3) the method produces scaling laws for column collapse runout and slump that agree well with experimental results; and (4) the method produces time-dependent column collapse profiles down inclined planes that agree remarkably well with those observed experimentally. In addition to these major findings, we also illustrate with these examples the role of β in our friction law (Eq. 5.7), the influence of our boundary condition on slip velocities and interior pressures, the effect of scaling the bulk modulus on simulation results, and the influence of numerical resolution (i.e. SPH particle mass).

5.4.1 Example 1: Angle of repose

This example illustrates how the friction coefficient μ that appears in Eq. (5.3) influences the simulated angle of repose of the material. The friction coefficient μ appearing in Eq. (5.3) is readily related to the internal friction angle ϕ of the material by comparing Eq. (5.4) to the classical Mohr-Coulomb failure criterion to obtain

$$\phi = \tan^{-1}(\mu) \tag{5.29}$$

[128] noted that the angle of repose of a dry granular material has a roughly constant value close to the angle of internal friction of the material in the loosest packing state. This definition suggests that the angle of repose should be a lower bound for the internal friction angle of the material. To test our model's ability to approximate this effect, we simulate a slump test through an orifice using various

internal friction coefficients and compare the resulting angles of repose θ with the internal friction angle computed using Eq. (5.29). As the first example of this method, we also use the results to illustrate the pressure-drop in the bottom-most layer of the slumped granular piles (mentioned in section 5.3.5).

The initial simulation conditions are shown in Fig. 5.2a. The simulated bulk of granular material measures 60 cm in the x dimension, 50 cm in the y dimension, and 6 cm in the z dimension (into the page). Periodic boundary conditions are used in the z direction to produce the effect of an infinitely wide slope. The granular material is permitted to leave the domain through a 5 cm wide orifice in the bottom boundary. The final simulation conditions are shown in Fig. 5.2b. Once the granular media has flowed through the orifice and come to rest (kinetic energy density of less than 1×10^{-5} J/m^3), the resulting angle of repose is measured by a linear least-squares fit to the surface of the material in the middle 75% of the domain between the left wall and the orifice. The simulation parameters used for this example are shown in Table 5.1. The SPH particle spacing is chosen to be $\Delta x = 0.01$m and the SPH particle mass is chosen to produce the loosest packing density of the granular material ρ_0 at this particle spacing. Five simulations are run, each with a constant internal friction coefficient between 0.364 ($\phi = 20°$) and 0.839 ($\phi = 40°$). The parameter κ is set to 10^5 to reduce the wave speed and permit a large time step. It will be shown in example 3 that this choice, rather than a more realistic choice (e.g., 10^7 or higher), does not significantly influence the material response in simulations where the wave speed does not control the quantities of interest or the quasi-static deformation field is not of interest. In simulations in which wave speed plays a significant role or the quasi-static deformation must be captured accurately, κ should be chosen to enforce a more realistic bulk modulus. The dilation β is limited to $0 \leq \beta \leq 0.5$ as discussed in section 5.2.3.

Simulation results are shown in Fig. 5.2c. Results are shown both for simulations with and without β included in the calculation of friction (see Eq. (5.7)). The simulations that do not use β in the calculation of friction ($\beta = 0$) yield an angle of repose slightly lower than the internal friction angle of the material. This is consistent with

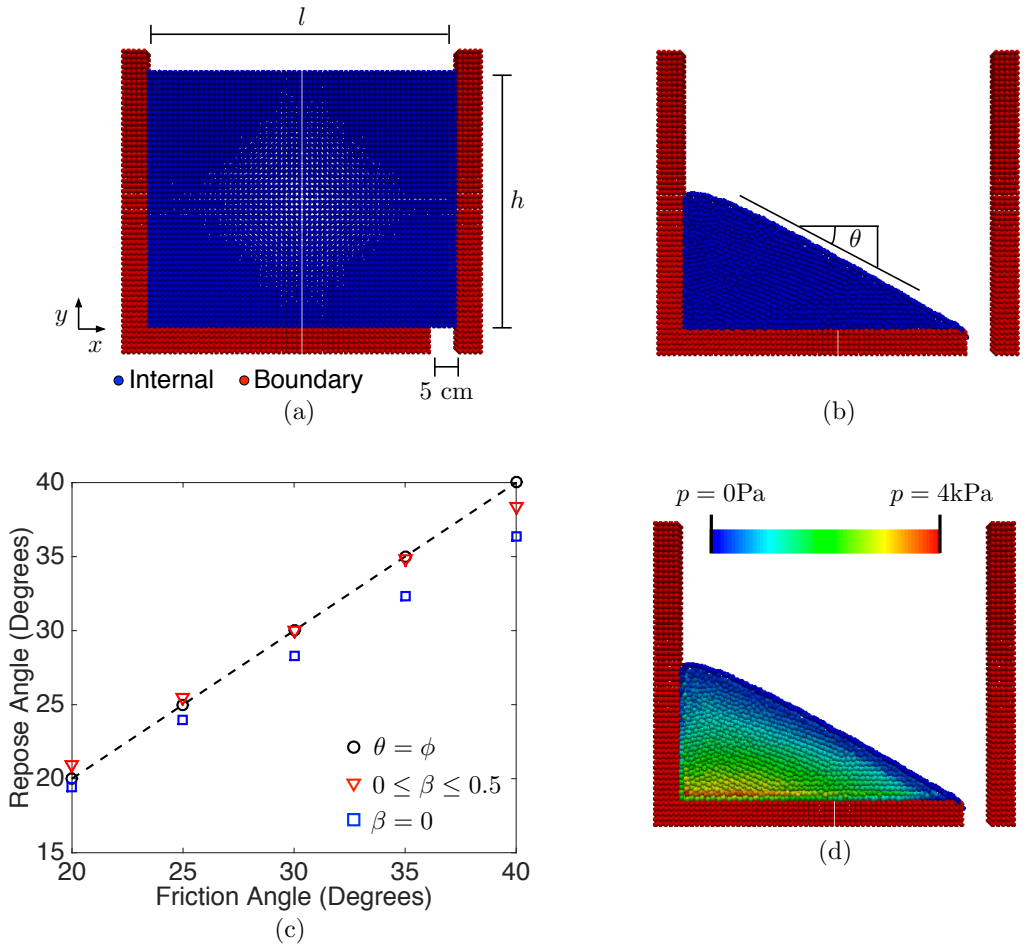

Figure 5.2: (a) Initial conditions of the slump test through an orifice. In color, blue represents internal SPH particles and red represents boundary particles. Length $l = 60$ cm, $h = 50$ cm, and the size of the simulated material in the z dimension is 6 cm. (b) Final collapsed side profile of the slump test through an orifice for $\phi = 30°$. The repose angle θ is measured in the middle 75% of the domain between the left wall and the orifice. (c) Results of the simulations with and without including β in the calculation of friction. The dashed line and circles represents the curve $\theta = \phi$. Results without β are blue squares which provide a lower bound to the $\theta = \phi$ curve. Results with β are red inverted triangles which nearly match the $\theta = \phi$ curve. (d) Pressure in the collapsed granular pile for $\phi = 30°$ showing a slight pressure drop in the layer of SPH particles directly above the bottom surface of the container.

Table 5.1: Model parameters used in the angle of repose simulations. Note that the friction law is taken as rate-independent, so μ_h is set to μ_l and the value of D^* is irrelevant. Basal friction coefficient μ_b is also set to μ_l. The initial SPH particle spacing of $\Delta x = 0.01$ m corresponds to the loosest packing state of the material (i.e. in which $\rho = \rho_0$.)

ρ_0 (kg/m^3)	μ_l	μ_h	D^*	c (Pa)	μ_b	κ (Pa)	γ	Δx (m)
1550	0.364-0.839	μ_l	-	0	μ_l	10^5	1.5	0.01

the classical theory of the angle of repose discussed by [128]. Simulations including β in the calculation of friction ($0 \leq \beta \leq 0.5$) yield an angle of repose that nearly matches the internal friction angle of the material, again consistent with the classical theory. Both simulation results deviate from the classical theory at large friction angles. This deviation may suggest a limitation of using a viscoplastic model for high friction angle materials but has not yet been fully investigated.

These results suggest that the constitutive law proposed in this work, both with and without the inclusion of dilation, is able to reproduce a key feature of granular systems: a steady-state angle of repose θ that is a lower bound for the internal friction angle ϕ of the material. We can see from Fig. 5.2c that including β in the calculation of friction in Eq. (5.7) has the effect of slightly increasing the yield strength of the granular material. This feature is consistent with the classical theory that β enhances the ultimate strength of a granular material leading up to steady-state (e.g., see [85,107]). However, including β in our model also appears to enhance steady-state strength slightly. This feature of the constitutive law and chosen parameters is discussed in more detail in section 5.4.2.

Fig. 5.2d illustrates the pressure distribution in the collapsed granular pile (for $\phi = 30°$). This distribution is qualitatively similar to our simulations with other material parameters. Interior SPH particles in the layer directly above the bottom surface of the container exhibit a pressure slightly below that of the second layer. This occurs because of the reduced value of ρ_0 taken for boundary particles, as mentioned in section 5.3.5. Using an identical value of ρ_0 for boundary and internal particles

eliminates this effect and restores the linear pressure increase as a function of depth up to and including the bottom layer of interior SPH particles. However, using identical values of ρ_0 for boundary and internal particles can lead to internal particles penetrating the boundary in some simulations. We have verified that aside from this artifact in the bottom-most layer, the pressure distribution in a pile under self-weight agrees with that expected from the overburden load. Therefore, we continue to employ this reduced value of ρ_0 for boundary particles and discuss possible extensions in section 5.5.

5.4.2 Example 2: Infinite inclined plane flow

Inclined plane flow experiments are a classical means of studying the rate-dependent frictional strength of granular media (e.g., see [4]). Experiments in this flow configuration have been used to derive rate-dependent frictional parameters, study Bagnold-type velocity profiles, investigate boundary-slip in granular flows, and examine non-local and finite-size effects of granular media (see [4, 88, 129, 130]). We use inclined plane flow simulations to qualitatively demonstrate the rate-dependent behavior of our friction law and to illustrate the slip generated by our boundary conditions. We also compare our results with a Bagnold-type velocity profile for completeness. Finally, we discuss the effect of including β and limiting it to $0 \leq \beta \leq 0.5$ on the frictional strength.

[105] presented a scaling argument for relating shear stress to strain rate in inertial granular flow that has since been used to derive a velocity profile for inclined plane flows. [130] and [88] derived Bagnold velocity profiles for inclined plane flows and found a close comparison when fitting to numerical and experimental results. The general form of the Bagnold profile is (see [88])

$$v_x(z) = A(\theta)\sqrt{gd}\frac{(h^{3/2} - (h-y)^{3/2})}{d^{3/2}} \tag{5.30}$$

where $A(\theta)$ is a θ dependent constant, θ is the slope inclination angle, g is the magnitude of gravity, d is the grain diameter, h is the height of the flow, and y is the

Table 5.2: Model parameters used in the infinite inclined-plane flow simulations. Note that the basal friction coefficient μ_b is taken as equal to the value of μ and thus is also rate-dependent.

ρ_0 (kg/m^3)	μ_l	μ_h	D^* (s^{-1})	c (Pa)	μ_b	κ (Pa)	γ	Δx (cm)
1550	0.268	0.577	20	0	μ	10^5	1.5	0.01

height above the inclined boundary. Close to the inclined plane surface, results do not fit well due to a clearly observed nonzero boundary slip velocity (see [130] and discussion in [88]). In addition, the Bagnold profile does not fit the results at the free-surface, where [88] notes that there is a nonzero shear rate exhibited numerically and experimentally but not modeled by Bagnold's theory.

Figure 5.3a illustrates the setup of our inclined-plane flow simulations. The simulated bulk of granular material measures 10 cm in the x dimension, 15 cm in the y dimension and 5 cm in the z dimension (into the page). Periodic boundary conditions are used in the x and z directions to simulate the effect of an infinitely wide and long slope. Table 5.2 lists the simulation parameters. The material is modeled as rate-dependent with a friction coefficient varying from $\mu_l = 0.268$ ($\phi = 15°$) to $\mu_h = 0.577$ ($\phi = 30°$) with parameter $D^* = 20$ s^{-1}. The bottom boundary is modeled using five layers of fixed SPH particles with the same properties as those used to represent the granular material, including frictional properties μ_l, μ_h, D^*. Often a constant basal friction coefficient is used in simulations of granular flows (e.g., see [109]). We find that such a choice results in an unbounded boundary slip velocity when the inclination angle exceeds the basal friction angle. Therefore, a constant basal friction coefficient does not capture the classical nature of rate-dependent inclined plane flows in which the material can find a steady state at a variety of inclination angles. The granular material is permitted to settle under self weight before tilt is instantaneously applied by changing the direction of gravity. The velocity profile is monitored by spatially averaging SPH particle velocity in bins of various heights (in 0.01m increments from the bottom boundary).

Simulation results are shown in Figs. 5.3c-d and 5.4a-d. Figs. 5.3c-d illustrate

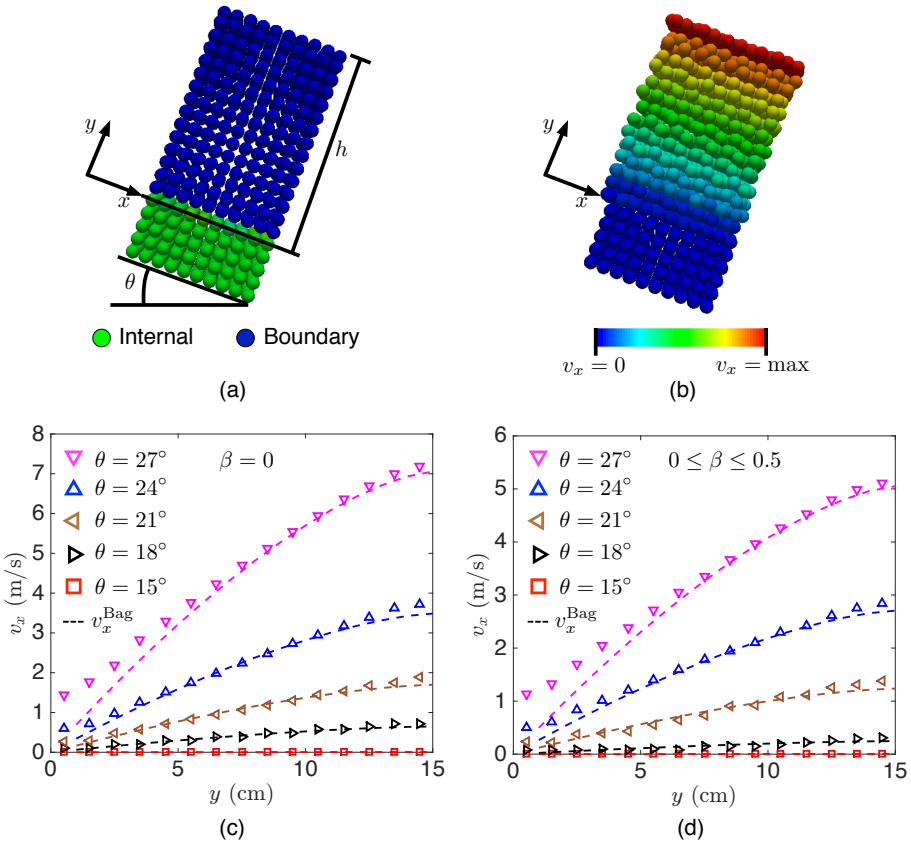

Figure 5.3: (a) Initial conditions of a typical inclined plane flow experiment showing internal SPH particles above $y = 0$ and boundary particles at or below $y = 0$. (b) A typical velocity profile of an inclined plane flow. (c) Velocitiy profiles in the x direction as a function of height y in the granular material for simulations that do not include β in the calculation of friction. Symbols represent simulation results and dashed lines represent the best fit of the Bagnold profile (Eq. (5.30)) to the simulation data. (d) Same as (c) but for simulations that include β in the calculation of friction.

the steady-state velocity profiles (symbols) for inclination angles angles ranging from $\theta = 15^\circ$ to $\theta = 27^\circ$ in increments of 3° for simulations both with and without β included in the calculation of friction. We clearly see a nonzero steady-state velocity profile for angles $\theta = 18^\circ$ through $\theta = 27^\circ$, as expected from the friction law. For simulations with $\theta = 12^\circ$ (not shown) and $\theta = 15^\circ$, the steady-state velocity profile is zero because the imposed shear stress on the material equals but does not exceed the yield strength (incipient flow). For simulations using $\theta = 30^\circ$ (also not shown), the velocity profile appears to approach a nonzero steady-state for simulations both with and without the inclusion of β in the calculation of friction. However, relaxation is very slow and we do not simulate the response to steady-state because of the immense computational cost. For simulations using $\theta = 33^\circ$, the velocity profile does not approach a steady-state profile for simulations either with or without β included in the calculation of friction because the imposed shear stress on the material exceeds maximum material strength, leading to a constant downslope acceleration.

Also shown on Figs. 5.3c-d as dashed lines are the Bagnold velocity profiles, found using a least-squares fit of Eq. (5.30) to the data. These profiles demonstrate an excellent match with the simulation data (symbols) within the bulk of the flow. The mismatch at the boundary and free-surface is consistent with the discussion in [88], highlighting the nonzero slip at the boundary and the nonzero strain rate at the free surface.

Fig. 5.4a-b illustrates the average bulk acceleration $\dot{\bar{a}}$ of the granular material as a function of time for all simulations. This average bulk acceleration is computed by averaging the velocities of all interior SPH particles in each simulation and taking the time derivative using backward finite difference with a time step of 0.01s. We note that due to finite numerical precision, all simulations eventually contain minor particle disorder and therefore fluctuations in the $\dot{\bar{a}}$ versus time curve. We thus fit each the data with a curve of the form

$$\dot{\bar{a}} = a + \frac{b-a}{c/t+1} \tag{5.31}$$

where a, b, and c are best-fit parameters, and t is time in seconds. These curves are fit to the data from the point of maximum acceleration, which occurs at roughly 0.02s after gravity is rotated in each simulation. These curves are the ones shown in Figs. 5.4a-b, with the raw data and fits shown superimposed in the inset plots. It is clear to see that for inclination angles from $\theta = 12^\circ$ to $\theta = 27^\circ$, a nonzero steady-state velocity profile is reached for simulations with and without β. This is confirmed by the best-fit parameter b in Eq. (5.31) being zero or very close to zero for each of these data sets. For inclination angle $\theta = 30^\circ$, the bulk acceleration approaches zero but does not reach zero in the time frame of our simulation, as mentioned above. For inclination angle $\theta = 33^\circ$, the bulk acceleration asymptotes to a nonzero value for simulations both with and without β being included in the calculation of friction.

Figs. 5.4c-d show the slip velocities for all simulations, computed by averaging the velocity of the bottom-most layer of SPH particles parallel to the stationary boundary. The raw data is shown for each inclination angle as well as a dashed-line found by least-squares fit of the data to Eq. (5.30). Consistent with other numerical simulations and experiments, we observe a nonzero slip velocity that increases monotonically with inclination angle (see insets for slip velocity versus θ). The slip velocities asymptote toward a constant value for inclination angles $\theta = 12^\circ$ through $\theta = 30^\circ$ for simulations both including and excluding β. Slip velocities undergo unbounded increase for inclination angles above $\theta = 30^\circ$ in simulations with and without β.

The slip velocities are a general feature both of the boundary conditions imposed in our simulations and of the constitutive law. Future work could involve implementing no-slip or reduced-slip boundary conditions by imposing an artificial stress tensor on boundary SPH particles, with a value falling between the stress tensor computed directly from Eq. (5.3) and that of the neighboring interior particles. This reduced-slip boundary condition could be calibrated to experimental data on boundary slip in real granular materials. We have verified that applying an artificial stress tensor to boundary SPH particles does indeed produce a no-slip condition, as discussed by [113, 121]. More details on our boundary condition are found in section 5.3.5.

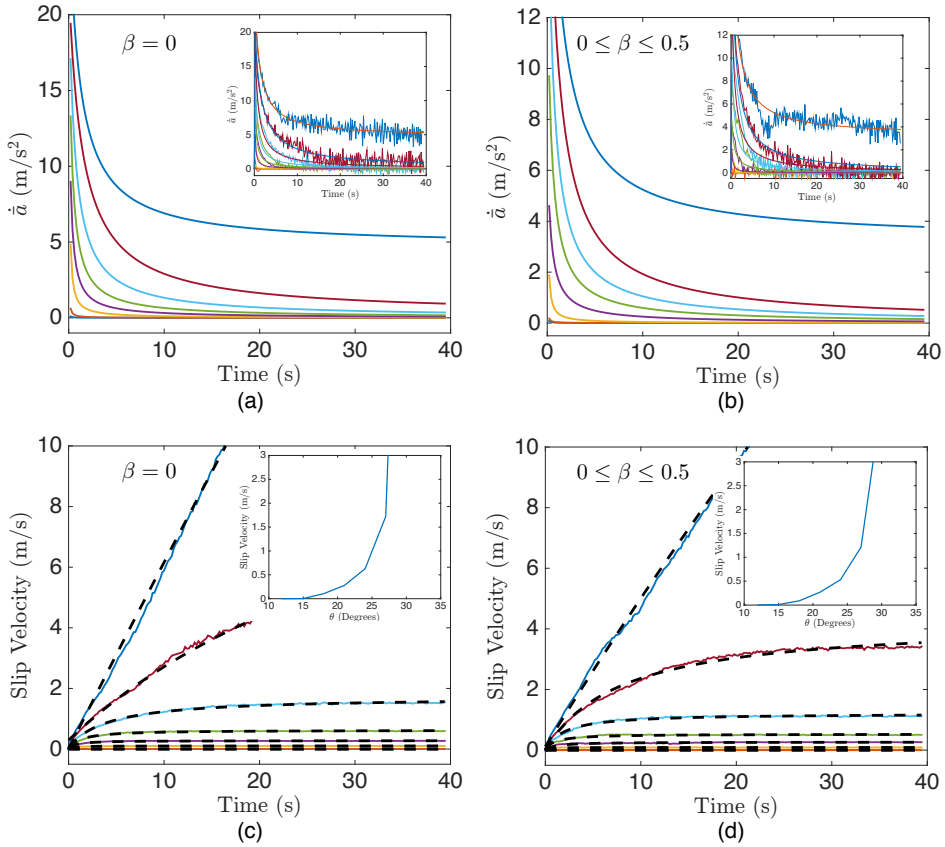

Figure 5.4: (a) Bulk acceleration $\dot{a}$ of the granular material in the inclined plane simulations, without the use of β in the calculation of friction, as a function of time. The highest curve represents $\theta = 33°$ and each lower curve represents a reduction in θ by 3°. All accelerations appear to asymptote to zero except for $\theta = 33°$. The inset shows raw data overlaid with the same fits. (b) Same as (a) except for simulations that include β in the calculation of friction. (c) Slip velocity in simulations not including β in the calculation of friction, found by averaging the v_x velocity of the bottom-most layer of interior SPH particles. All slip velocities appear to asymptote to finite values except for $\theta = 33°$. (d) Same as (c) but for simulations that include β in the calculation of friction.

5.4.3 Example 3: Granular column collapse

Granular column collapse is an important test of the flow and yield behavior of granular materials. This test is significant for a number of processes such as landslides, granular avalanches, hill-slope stability, and granular dam-break scenarios. Many researchers have studied this problem numerically and experimentally in order to understand the dynamics of the yielding and flow processes, the timescales associated with various regimes of flow, the local rheology within the flow, and the final scaling laws that describe the slumped profile of the medium (see [5, 108, 112, 131, 132, 133, 134, 135, 136]). Scaling laws describing the slumped runout length and final height of a collapsed granular medium are typically studied using an axisymmetric column or quasi-two-dimensional rectangular column as an initial state. These studies are designed to predict the basic physics of a sudden collapse event such as a landslide. This example examines the ability of our numerical model to produce scaling laws for quasi-two-dimensional column collapses consistent with those found in existing experimental literature. We also use this flow configuration to illustrate the influence of resolution (SPH particle mass and spacing), bulk modulus, and friction parameters on the final results of a column collapse simulation. The results of this latter study establish the resolution and reduced bulk modulus used in other examples as acceptable for accurately modeling processes such as granular avalanches.

5.4.3.1 Scaling laws

In order to compare our scaling laws with experimental data, we simulate column collapse using two materials with properties reported by [5]. In particular, we model "grit" (a fine-grained sand) and fine glass beads. These two materials have distinct bulk friction angles and loose-packing densities. Furthermore, both experience basal friction angles ϕ_b that are different than their bulk friction angles ϕ, as reported by [5]. Table 5.3 tabulates all properties of both materials, as well as the parameters used in modeling each for this particular analysis. Both materials are modeled as rate-independent and cohesionless, using the nominal parameters reported by [5]. The

basal friction coefficient is $\mu_b = \tan^{-1}(\phi_b)$.

Figs. 5.5a and 5.5b illustrate the initial setup of a typical SPH simulation of grit and fine glass, respectively. The most significant difference between the two initial configurations is the different initial length of the columns L_0. Simulations of grit use $L_0 = 9$ cm while simulations of fine glass use $L_0 = 2.5$ cm. These values roughly reflect those used for fitting scaling laws in [5] (i.e. see Figs. 10 and 11 of that reference). A finer resolution is used for the fine glass simulations ($\Delta x = 0.005$ cm) than for the grit simulations ($\Delta x = 0.01$ cm) in order to accommodate this difference. Various initial heights H_0 (19 for grit simulations, 13 for fine glass simulations) are used in order to examine the final runout L and final height H as a function of initial column aspect ratio $a = H_0/L_0$. In all simulations, the simulated bulk of grit or fine glass measures 10 cm in the z dimension. Periodic boundaries are employed in the z dimension to produce the effect of an infinitely wide slope. We note that this differs from experiments presented by [5], who used sidewalls spaced 20 cm apart. We ignore the effect of sidewalls in this analysis of scaling laws since we are primarily interested in a scaling exponent. Sidewalls would have the effect of increasing the apparent bulk friction ϕ slightly, as discussed in [137]. This would influence the runout and final height of individual runout simulations but would not significantly influence the derived scaling laws from a number of simulations using the same conditions. We let the simulated grit or fine glass settle under self weight before instantaneously deleting the right-most vertical wall and allowing the material to flow until it comes to rest. After the material comes to rest, we measure the final height H by finding the y coordinate of the highest interior SPH particle in the domain. We measure the final runout length L by finding the largest x coordinate of an interior SPH particle in the domain. Using materials with distinct bulk and basal friction coefficients and loose-packing densities suggests that our method is likely able to accurately capture the behavior of various materials flowing over various substrates.

Figs. 5.6a-d illustrate the our column collapse results for simulations with (Figs. 5.6c and 5.6d) and without (Figs. 5.6a and 5.6b) including the rate of dilation β in the calculation of the friction coefficient. As reported in [5], data for each material

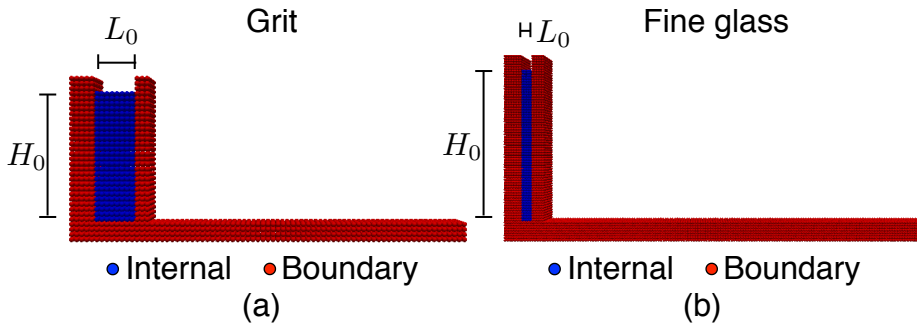

Figure 5.5: Typical initial conditions of the column collapse simulations for (a) grit and (b) fine glass. The right-most vertical wall in each figure is the containing wall that is deleted at $t = 0$. In the color figure, blue particles represent internal particles and red particles represent boundary particles.

Table 5.3: Model parameters used in the granular column collapse simulations. Both materials are modeled as rate-independent. Bulk and basal friction angles are taken as the nominal values reported in [5].

Material	ρ_0 (kg/m^3)	μ_l	μ_h	D^* s^{-1}	c (Pa)	μ_b	κ (Pa)	γ	Δx (cm)
Grit	1404	0.74	0.74	-	0	0.335	10^5	1.5	0.01
Glass	1450	0.456	0.456	-	0	0.263	10^5	1.5	0.005

Table 5.4: Comparison of scaling laws derived from simulation data and those reported in [5]. Note that [5] does not report values for λ_1 or λ_2.

Source	λ_1	α_a	λ_2	α_2
SPH Grit ($\beta = 0$)	1.24	0.55	1.99	0.72
SPH Glass ($\beta = 0$)	2.07	0.61	3.49	0.72
SPH Grit ($0 \leq \beta \leq 0.5$)	0.97	0.61	0.79	1.01
SPH Glass ($0 \leq \beta \leq 0.5$)	1.38	0.68	1.36	0.96
[5] Grit	-	0.58	-	0.88
[5] Glass	-	0.6	-	0.92
[5] All	-	$\sim$0.6	-	0.9$\pm$0.1

with $a > 1.7$ collapse well onto a linear line in logarithmic space indicating scaling laws of the form

$$\frac{H_0}{H} \sim \lambda_1 a^{\alpha_1} \quad \text{and} \quad \frac{(L - L_0)}{L_0} \sim \lambda_2 a^{\alpha_2} \tag{5.32}$$

where $\lambda_1, \lambda_2, \alpha_1$ and α_2 are scalars. The symbols in Fig. 5.6 represent the results of our SPH simulations while the dashed line indicates a least-squares linear fit to the data in logarithmic space. The reported slopes represent the scaling exponents α_1 and α_2. We find similar scaling exponents α_1 for final heights for grit and glass using $\beta = 0$ (Fig. 5.6a) and $0 \leq \beta \leq 0.5$ (Fig. 5.6c). As shown in table 5.4, these scaling exponents agree well with the experimental results of [5] in wide slots (most similar to infinitely wide slope modeled here; see Fig. 10 in that reference), indicating that our method, both with and without β, accurately captures scaling of the granular column collapse scenario. We find different values for final runout scaling when using $\beta = 0$ (Fig. 5.6b) and $0 \leq \beta \leq 0.5$ (Fig. 5.6d). The final runout scaling for $0 \leq \beta \leq 0.5$ agrees more closely with results of [5] for their gate experiments (most similar to the infinitely wide slope modeled here; see Fig. 11 in that reference), as shown in table 5.4. Individual simulations of laboratory-scale experiments using $\beta = 0$ tend to over-predict runout length, as discussed more in section 5.4.4. These results collectively indicate that our present simulations that include β in the calculation of friction can accurately reproduce experimental data. Section 5.4.4 further supports this claim.

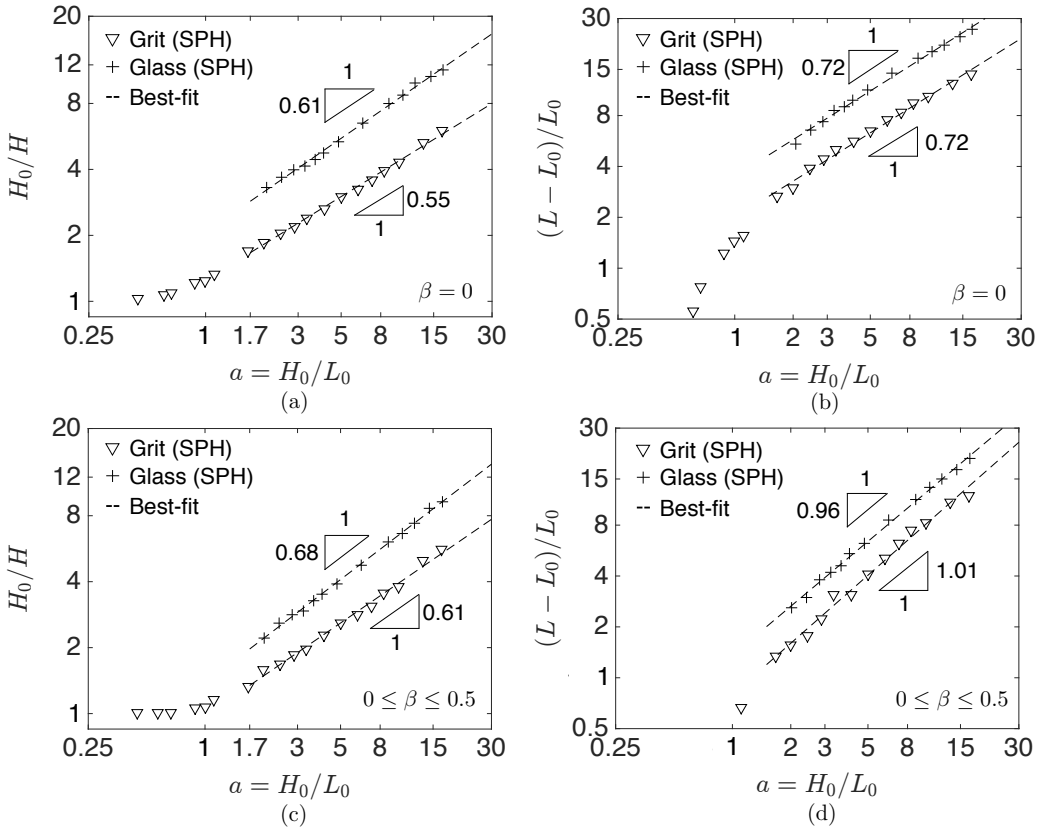

Figure 5.6: (a) Scaling laws for collapsed height in simulations not using β in the calculation of friction. Symbols are SPH simulations and dashed lines are linear best-fit lines in logarithmic space for all data with x coordinate above 1.7. (b) Scaling laws for collapsed runout distance in simulations not using β in the calculation of friction. (c) Same as (a) but for simulations using β in the calculation of friction. (d) Same as (b) but for simulations using β in the calculation of friction.

5.4.3.2 Reduced bulk modulus, friction angle, and resolution studies

We briefly explore the influence of resolution (SPH particle spacing and mass), reduced bulk modulus, and employed friction angle on the numerical results. For this study, we simulate the experimental setup of [5] with grit in a wide slot. The simulation is identical to those discussed in section 5.4.3.1 and listed in the first row of table 5.3 except the initial length L_0 is set to 20 cm, the initial height H_0 is set to 13 cm, and the z dimension is periodic and measures 18 cm. The simulation parameters for three parametric studies are outlined in table 5.5. Since the goal of this particular parametric study is not to investigate the influence of β on the results, we present some comparisons entirely with $\beta = 0$ and others entirely with $0 \leq \beta \leq 0.5$.

The first study explores the effect of varying κ over two orders of magnitude in the EOS presented in Eq. (5.5). The results of this study are shown in Fig. 5.7a which portrays simulation results with symbols and the experimentally observed collapse profile with a dashed black line. This figure illustrates that the bulk modulus has only a minor influence on the final results for this type of simulation. This is further supported by the results of example 4, which illustrate an excellent agreement between simulated time-dependent dynamic data using a reduced bulk modulus and experimental results. The second parametric study explores the effect of varying the bulk and basal friction coefficients within the error bounds provided in [5] for grit: $\phi = 36.5° \pm 4.5°$ and $\phi_b = 18.5° \pm 1.5°$. As shown in Fig. 5.7b, there is a clear difference in the response of the material, although the difference is minor. The difference in response is also as expected: a lower friction angle increases runout and reduces the slumped height of the material. This topic will be discussed in more detail in section 5.4.4. Finally, the third parametric study explores the effect of varying the resolution of the simulation. In SPH, the resolution simply follows SPH particle spacing and mass. We vary initial particle spacing over almost an order of magnitude, using 4,680 particles in the coarsest simulation with $\Delta x = 0.01$ m, 37,440 particles in the intermediate resolution simulation with $\Delta x = 0.005$ m, and 299,250 particles in the finest simulation with $\Delta x = 0.0025$ m. Fig 5.7c illustrates "mesh-convergence" in

Table 5.5: Model parameters used in parametric studies of granular column collapse. All models are rate-independent.

Test	ρ_0 (kg/m^3)	μ_l	μ_h	D^* s^{-1}	μ_b	c (Pa)	κ (Pa)	γ	Δx (cm)
Modulus	1404	0.74	0.74	-	0.335	0	10^5	1.5	0.01
Modulus	1404	0.74	0.74	-	0.335	0	10^6	1.5	0.01
Modulus	1404	0.74	0.74	-	0.335	0	10^7	1.5	0.01
Friction	1404	0.74	0.74	-	0.335	0	10^5	1.5	0.01
Friction	1404	0.87	0.87	-	0.364	0	10^5	1.5	0.01
Friction	1404	0.625	0.625	-	0.305	0	10^5	1.5	0.01
Resolution	1404	0.74	0.74	-	0.335	0	10^5	1.5	0.01
Resolution	1404	0.74	0.74	-	0.335	0	10^5	1.5	0.005
Resolution	1404	0.74	0.74	-	0.335	0	10^5	1.5	0.0025

the sense that progressive refinements in resolution appear to approach the results of the finest resolution ($\Delta x = 0.0025$ m). Fig. 5.7c also demonstrates that the coarsest resolution of $\Delta x = 0.01$ m used in most of the examples in this chapter yield nearly identical results to the finest resolution. Further studies into mesh refinement along with the results presented in Fig. 5.7c can elucidate the appropriate mesh to select for field scale simulations of events such as dry granular avalanches. Future studies on resolution are discussed in section 5.5.

5.4.4 Example 4: Column collapse down inclined planes

The ability of a numerical method to reproduce time-dependent two or three-dimensional granular collapse profiles down inclined planes is important for several reasons. First, granular column collapses down inclined planes reach significantly higher velocities and strain rates than those on flat surfaces ([6, 109]), making comparison with such experiments a more challenging test of the flow rheology. Second, reproducing profiles of individual flows is a more challenging test of the flow rheology than reproducing scaling laws since many numerical methods such as DEM can accurately reproduce scaling laws despite strongly overestimating the runout of individual experiments ([134, 135]). Finally, capturing the full two or three-dimensional profile of a collapse is crucial since many complex features that govern the flow, such as convection cells, only occur below specific length scales ([111]). This last point further motivates the

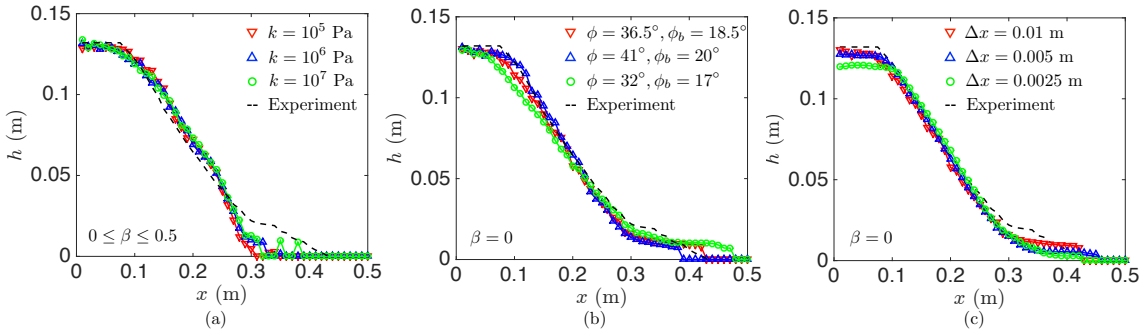

Figure 5.7: Results of parametric studies of various model parameters on numerical results. (a) Result of varying the bulk modulus over two orders of magnitude does not indicate any significant change in results. This also justifies our use of $\kappa = 10^5$ in most simulations in this chapter to eliminate the shorter time step that may otherwise be needed to ensure stability. (b) Result of varying bulk and basal friction coefficients within the experimental error bars of [5] illustrates the expected changes, but only minor changes. (d) Results of mesh-refinement study illustrate the coarse mesh used throughout the chapter produces results that are nearly the same as the finest mesh.

need for the three-dimensional full-field modeling techniques like the one presented in this chapter. One-dimensional depth-averaged finite difference models commonly employed in modeling geological flows are unable to resolve these complex features ([111]).

In this example, we compare time-dependent two-dimensional profiles of simulated column collapses down inclined planes with those reported at [6]. This comparison illustrates the capability of our method to reproduce the complex three-dimensional time-dependent dynamical processes occurring during the collapse event. This comparison also demonstrates the importance of including the rate of dilation β in the calculation of the friction coefficient for such processes.

We study four sets of numerical simulations of quasi-two-dimensional column collapses down inclined planes with parameters listed in table 5.6. Each row of table 5.6 represents the parameters used in one set of simulations that includes the rate of dilation β in the calculation of friction and one set of simulations that does not include β. The distinction between the rows is the use of sidewalls. Two simulations employ periodic boundary conditions in the z direction to produce the effect of an infinitely wide slope, while the other two explicitly model the sidewalls present in experiments. Figs.

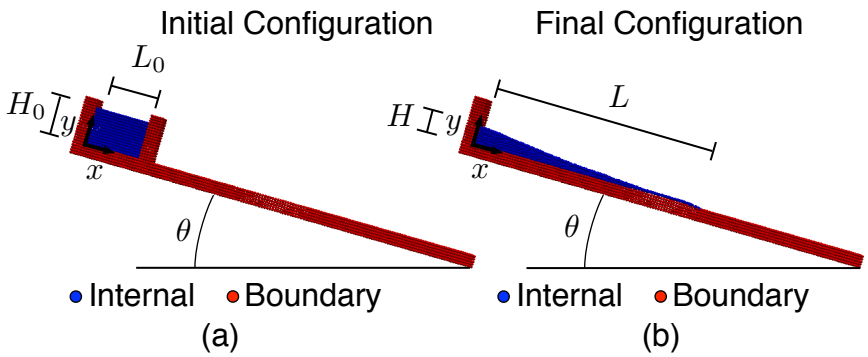

Figure 5.8: (a) Initial and (b) final configurations for simulations of column collapse down inclined planes. The right-most near-vertical wall in (a) represents the containing wall that is lifted in the y direction with $v_x = 2$ m/s at $t = 0$. In the color figure, blue particles represent interior particles and red particles represent boundary particles.

5.8a and 5.8b illustrate the typical initial and final configurations, respectively, of all simulations. Sidewalls are not shown in these figures. When used, sidewalls sandwich the interior SPH particles in the foreground and background between boundaries with the same properties as the basal boundary. In all cases, the initial length of the simulated granular material in the x dimension is 20 cm, the initial height in the y dimension is 14 cm, and the initial width in the z dimension (into the page) is 10 cm. Simulations progress by allowing the simulated material to settle under self weight before lifting the containing wall in the y direction with velocity 2 m/s starting at $t = 0$s. We use rate-independent friction in all simulations, leaving full parametric fitting of the rate-dependent rheology to existing experimental data for a future study. We note that this contradicts the work of [111] who used a rate-dependent model when simulating these collapses and [4] who derived rate-dependent parameters from laboratory experiments with similar flow rates. Nevertheless, we employ rate-independent friction and use the four sets of numerical simulations to illustrate how including β in the calculation of friction can increase the ultimate strength enough to accurately match experimental results. We note that the simulated granular material with parameters described in [6] and presented in table 5.6 is a collection of glass beads of diameter d between 600 and 800 μm.

Table 5.6: Model parameters used in column collapse simulations for deriving final runout and height scaling laws.

Sidewalls	ρ_0 (kg/m^3)	μ_l	μ_h	D^* (s^{-1})	μ_b	c (Pa)	κ (Pa)	γ	Δx (cm)
No	1550	0.435	0.435	-	0.435	0	10^5	1.5	0.01
Yes	1550	0.435	0.435	-	0.435	0	10^5	1.5	0.01

Figs. 5.9a and 5.9b illustrate the results of the simulations without sidewalls using $\beta = 0$ and $0 \leq \beta \leq 0.5$, respectively, for four inclination angles: $\theta = 0°, 10°, 16°$, and $22°$. Symbols in these figures represent the height of the highest SPH particle at three times after the containing wall is lifted. The lines represent the experimentally observed collapse profiles at these times reported in [6]. A comparison between Figs. 5.9a and 5.9b illustrates that simulations using β in the calculation of friction exhibit more accurate slumping in the bulk of the simulated material near the left-most boundary than simulations using $\beta = 0$ in Fig. 5.9a. Furthermore, simulations using β demonstrate reduced runout compared to those without β. These results are consistent with the simulations of [111], who found excessive slumping and runout even when using a rate-strengthening model without β. We have found in other simulations, not shown here, that increasing μ as suggested in [137] and [111] to model the effect of sidewalls does not correct the excessive slumping. The role of β in our simulations therefore plays the unique role of increasing the ultimate strength of the material to enhance yield strength and prevent slumping. It also appears to play a strengthening role near the flow front, where material is constantly turned over and subjected to rapid changes in strain rate.

Figs. 5.9c and 5.9d illustrate the results of the simulations with sidewalls using $\beta = 0$ and $0 \leq \beta \leq 0.5$, respectively, for the same four inclination angles as those in Figs. 5.9a and 5.9b. These simulations are performed in an effort to exactly reproduce the experimental conditions of [6]. In previous simulations where comparison to individual collapse profiles was not performed, simulating an infinitely wide slope was sufficient for qualitative and partial quantitative validation. The sidewall boundaries have the same properties as the bottom boundary. Fig. 5.9c illustrates that the pres-

ence of sidewalls, even without including β in the calculation of friction, improves the slumped profile and runout. However, the simulated profile near the left boundary is still significantly below that found in experiments. Furthermore, the numerical simulations continue to strongly overestimate the runout. Fig. 5.9d illustrates that including both sidewalls and β in the calculation of friction produces results that agree remarkably well at nearly all times for both the slump and runout. The exception to this remarkable fit occurs only for the highest inclination angle $\theta = 22°$, where the final runout is overestimated. This overestimation likely occurs because a rate-strengthening friction law is truly needed at the higher strain rates present at this inclination angle. The excellent agreement at nearly all times suggests that the presented numerical method, when modeling the same initial and boundary conditions as those found experimentally, and including β in the calculation of friction, can quantitatively reproduce collapse profiles and dynamics of granular flows down inclined planes.

For brevity, we leave a full investigation of the three-dimensional continuum fields and flow structures of our simulated incline plane flows for future work. Such an investigation will elucidate the physics behind the dynamical processes observed in simulations and experiments. In Fig. 5.10, we merely present snapshots of the 3D inclined plane flow with sidewalls at the same times as those shown in Fig. 5.9d. These snapshots are for the simulation employing β in the calculation of friction. SPH particles are rendered as spheres and colored by the magnitude of their strain rate tensor $\boldsymbol{D}$. We clearly see at all inclination angles that the flow progresses over a nearly stationary wedge of material. The influence of the sidewalls is evidenced by higher shear rates in the foreground and background where the sidewalls (not rendered) are located. It may be instructive in future work to investigate the flow/no-flow transition, the basal stresses, and the full three-dimensional structure of other continuum fields in these simulations.

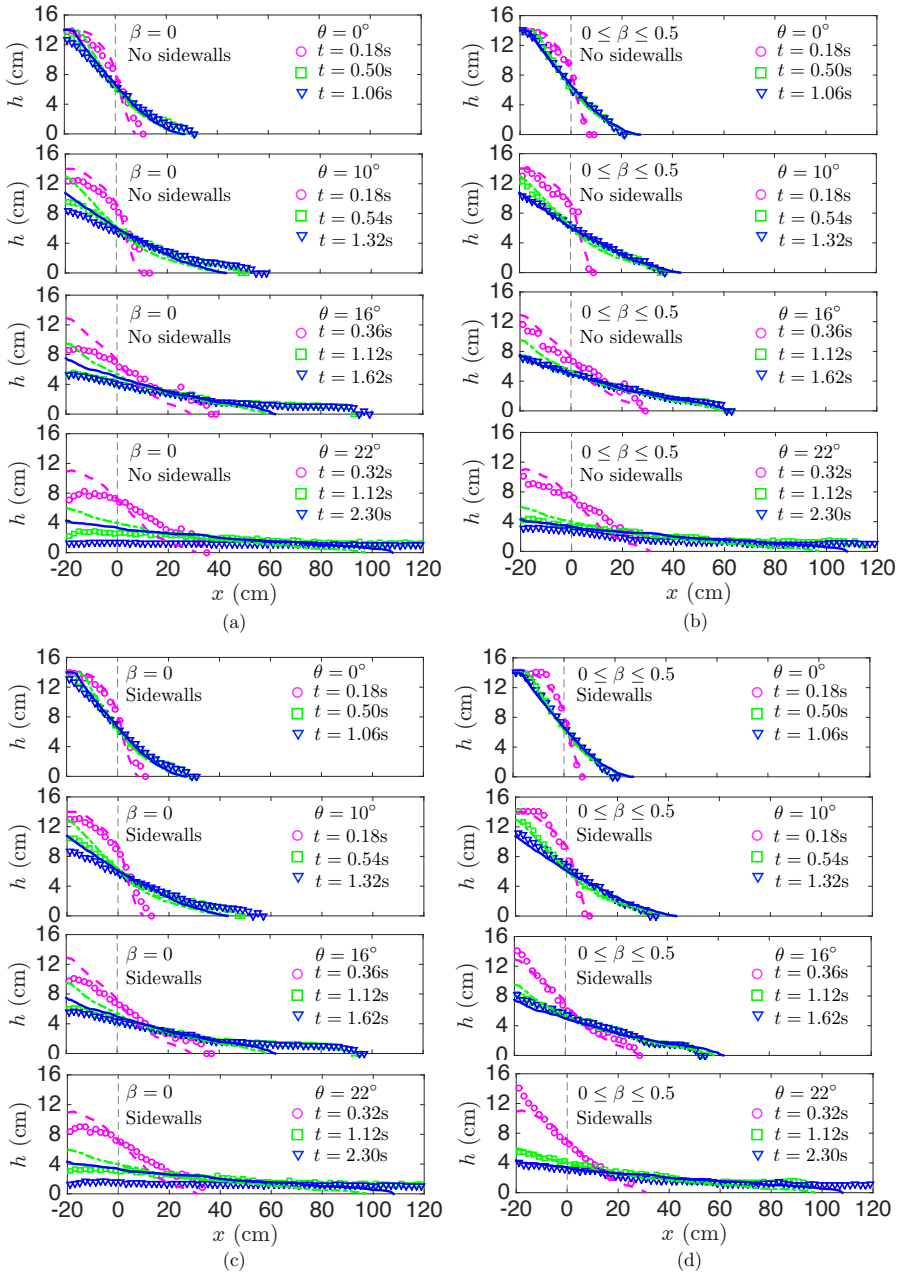

Figure 5.9: Time-dependent collapse profiles down inclined planes for four inclination angles: $\theta = 0°, 10°, 16°$, and $22°$. Symbols represent SPH profiles and lines represent experimental profiles from [6]. (a) and (b) illustrate results with periodic boundary conditions in the z direction and no sidewalls. (c) and (d) illustrate results with sidewalls. (a) and (c) show results for simulations not including β in the calculation of friction. (b) and (d) show results for simulations including β in the calculation of friction.

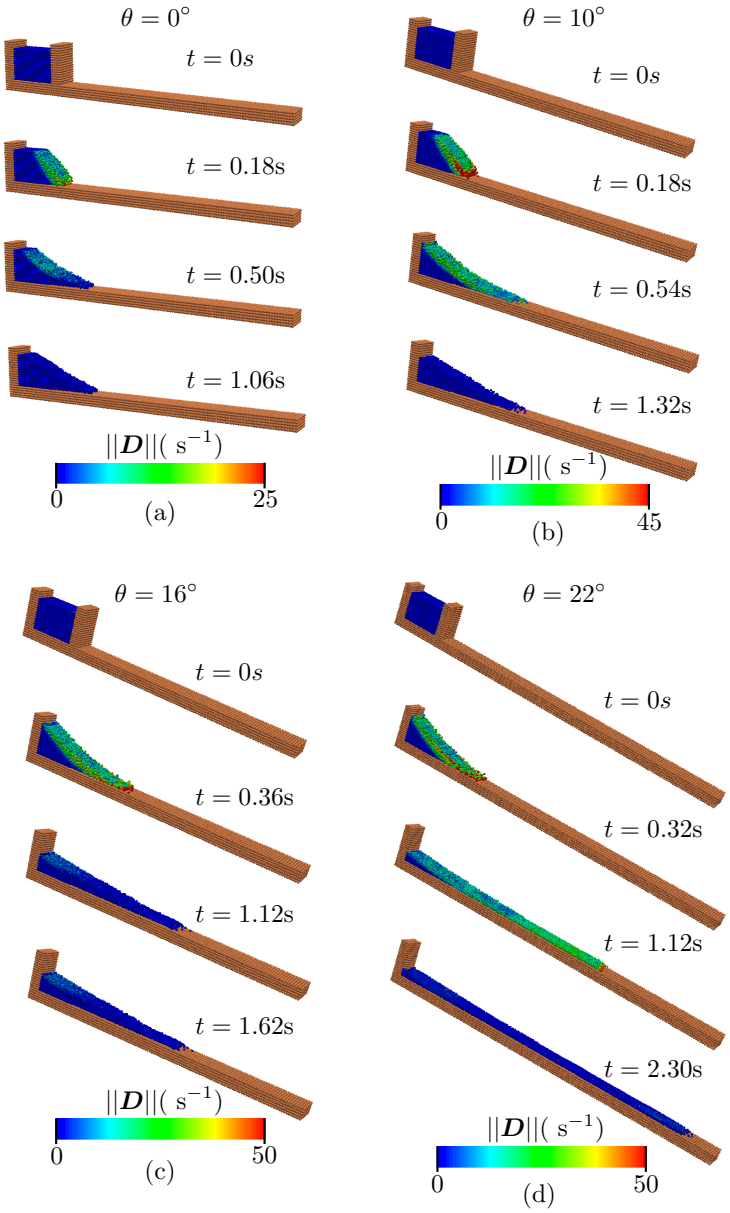

Figure 5.10: Snapshots of simulations shown in Fig. 5.9d for (a) $\theta = 0°$, (b) $\theta = 10°$, (c) $\theta = 16°$ and (d) $\theta = 22°$. These simulations employ β in the calculation of friction. In the color figure, the color of each particle corresponds to the magnitude of the strain rate tensor $\boldsymbol{D}$. We clearly see the influence of sidewalls (not rendered) at the first nonzero time for each inclination angle. At these times, particles appear to undergo a higher strain rate in the foreground and background than in the center of the flow.

5.5 Discussion and conclusion

We have presented an SPH method for simulating the flow of granular materials. A rate-dependent and dilation-dependent friction law has been employed and justified from an analysis of the continuum energy balance equation. Numerical examples have demonstrated that the SPH approach with the proposed constitutive law can accurately reproduce an angle of repose consistent with the employed friction angle, rate-dependent flows down inclined planes, scaling laws for granular column collapses on flat surfaces, and the dynamic structure of column collapses down inclined planes.

We have seen through numerical examples that future work is required before the numerical method can reliably be applied to a broad range of granular flows. In particular, four major aspects of the numerical method or constitutive law need additional study. First, the slip condition created by the imposed boundary condition needs additional calibration to experimental data in order to be reliable for many granular flows. Although it appears that the method is able to reproduce the runout of granular column collapses down inclined planes (e.g., see section 5.4.4), the inclined-plane flows in section 5.4.2 exhibit significant boundary slip that may not be realistic in all scenarios. Second, the method for calculating the rate of dilation β used in the friction coefficient needs to be refined and possibly given its own evolution law as discussed in section 5.3.4. This will involve calibrating the evolution of β as a function of numerous rheological parameters to experimental data as was done for the frictional parameters μ_l, μ_h, and D_s^* in [4]. Thirdly, we have not provided examples of simulating granular materials with cohesion (i.e. $c \neq 0$). We have done this purposefully since there exists less experimental validation data for flows of cohesive materials. Simulating cohesive flows poses an additional challenge in SPH of the so-called tensile instability. Methods exist for remedying the tensile instability (e.g., see [119, 121, 138]) and preliminary simulations of our method with cohesion do not exhibit a tensile instability, likely due to the real viscosity we employ. Nevertheless, future work should address any needed additions to our SPH framework that will permit simulation of highly cohesive flows in order to expand the range of problems

the method can address. Fourthly and finally, the friction law used in this chapter may need additional work before it can be applied to a range of very rapid granular flows. We have employed a friction law originally intended for steady-state flows in the present chapter. Eq. (5.13) and [15] have shown that additional terms related to changes in internal energy may be needed in flows exhibiting rapidly changing strain rates. Furthermore, using the inertial number rather than D_s^* in Eq. (5.7) as in [4] may be more accurate for many flows.

In addition to the future work described above, it would be instructive to use the method presented in this chapter to study the full three-dimensional structure of continuum fields in column collapses down inclined planes such as those presented in [6] and [136]. Future validation must also establish the the ability of the method to accurately reproduce stress fields at the base of granular avalanches, debris flows, and under sand piles. This test would elucidate the important role of basal stresses in erosion and deposition of sediment during geophysical flows [139]. Finally, we are currently implementing a two-phase approach for coupling granular flows with gas and fluid flows. This extension will permit full-field simulation of geophysical debris flows and other natural and industrial processes.

Chapter 6

Discussion and conclusion

6.1 Summary

In chapters 2 through 5, we have provided four studies of granular materials across length scales. We have focused on inter-particle forces at the micro-scale, illustrating how these quantities influence macro-scale behavior such as intruder dynamics. The inter-particle force inference technique detailed in chapters 2 and 3 provides a method of studying force chains and validating grain-scale numerical modeling techniques. The appeal of these methods is their applicability to arbitrarily shaped grains, non-linear materials and non-Hertzian contacts, and dynamic events. Ongoing and future work with these techniques is detailed in section 6.2.1.

In chapter 4, we have studied friction in granular flows at the mesoscale. We derived a new friction law relating the friction coefficient to the shear rate, coordination number, porosity, and grain-scale dissipation rates. This friction law allows us to examine, through grain-scale simulations with arbitrary contact laws (or potentially through experiments in the future), the grain-scale dissipation pathways responsible for causing macroscopic friction. This relationship also illustrates friction as a delicate competition between material dilation and grain-scale dissipation. When these two processes do not balance one another, rate-dependence is observed. Rate-strengthening friction is common in granular materials and has been studied using this relationship and numerical simulations. We direct the reader to another paper in which we extend this friction law to non-steady-state flows [15].

We have focused on continuum modeling at the macro-scale in chapter 5. Here, we developed a new technique for capturing the solid-like, liquid-like, and gas-like states of granular media in a single computational domain. The technique combines SPH and a viscoplastic constitutive law containing a strain-rate and dilation-dependent yield criterion. This yield criterion is justified theoretically using an analysis of the continuum energy balance equation analogous to that provided in [15]. Numerous examples demonstrate that the modeling technique accurately captures theoretically predicted and experimentally observed behavior of granular media in quasi-static and dynamic settings. Ongoing and future work will extend this technique to allow coupling of the granular material with gases and fluids, as described in section 6.2.2.

6.2 Ongoing and future work

6.2.1 Inter-particle force inference

We are currently applying the inter-particle force inference technique developed in chapters 2 and 3 to opaque three-dimensional single-crystal quartz grains imaged using combined X-ray tomography and x-ray diffraction. This work is in collaboration with Stephen Hall at Lund University and follows work described in [49].

The data set currently being studied comes from an oedeometric compression test on 77 nearly-spherical single-crystal quartz grains contained in a 1.5 mm diameter by 1.5 mm tall quartz oedeometer. The grains are subjected to one-dimensional load-unload-reload up to 70 N on the load curve and up to failure on the reload curve. We note that failure occurs by crushing of a single grain in a strong force chain. Fig. 6.1a illustrates the macroscopic load as measured by the load cell during this experiment. X-ray computed tomography (XRCT) and X-ray diffraction (XRD) are used periodically during the compression cycle to extract a volumetric image of the assembly and volume-averaged grain strains (e.g., see [49, 81]). Fig. 6.1b shows a sample volumetric image of the assembly obtained with XRCT during the load cycle. Various in-house algorithms are being applied to these volumetric images to extract

the evolution of particle position and contact point location and direction throughout the loading cycle. Preliminary results of force inference using Eq. (3.19) at a single load step are illustrated in Fig. 6.1c. Force chains are clearly seen to develop in the bulk of the material, splitting and recombining at various locations. While we will defer presenting most quantitative results until a future publication, we will mention that the results agree remarkably well with expected statistical trends. In particular, inferred forces exhibit an exponential probability distribution above the mean force at each load step. Forces also divide into a strong (40% of total contacts) and weak (60% of total contacts) network in close agreement with the predictions of [27].

The goal of the work described above is to provide the first three-dimensional example of our force inference technique applied to opaque grains with sand-like stiffness. In addition, the ongoing work will determine whether forces in such systems exhibit features and statistics consistent with past theory and simulations. Force distributions and force chains will also be studied leading up to the crushing event that occurs during the reload cycle. This crushing event is a characteristic means of dissipating energy during failure for granular media. A deeper understand of force arrangement leading up to crushing could improve plasticity models and predictions of energy dissipation for granular materials. However, the grain crushing event cannot be accurately modeled with available grain-scale numerical techniques. Thus, the force inference technique can provide information currently only experimentally available, and can also serve as a calibration tool when grain-scale models for particle crushing are developed.

6.2.2 SPH modeling of coupled granular media and fluid flows

We are currently extending the SPH technique described in chapter 5 to handle gas and fluid flows coupled to granular flows. This work was originally motivated by a need to model gas impinging on a porous surface of sand or soil. This problem has important applications for planetary exploration, where the current technique of

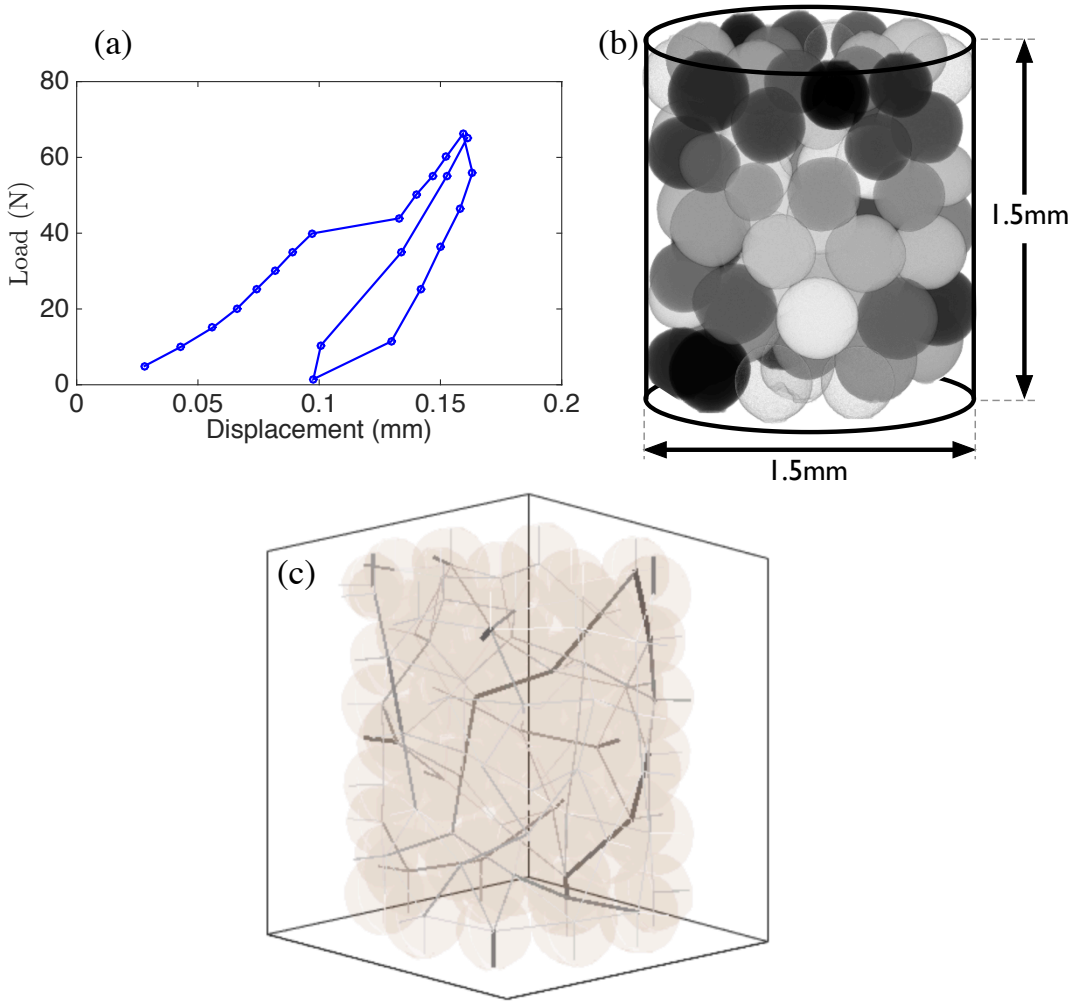

Figure 6.1: (a) Macroscopic load curve for oedeometric compression of single-crystal quartz grains. (b) Sample volumetric image of the assembly obtained with XRCT during the load cycle. (c) Preliminary results of force inference using Eq. (3.19) applied to a single load step. Lines connect contacting grain centroids and are darkened and thickened linearly with force magnitude.

landing on celestial bodies involves firing rockets downward to arrest motion during the final stages of vehicular descent. Predicting erosion during this descent would tighten the bounds on mission risk and provide a quantitative means of comparing landing sites. While extensive work has addressed part or all of this problem (e.g., see [140, 141, 142, 143]), the problem involves numerous coupled phase interactions that are not easily examined separately. For example, viscous erosion, fluidized soil erosion, and soil diffusion are all processes involving the coupled interaction of a gas and granular material. Thus, a full-field modeling technique that captures the coupled behavior of these two phases is required for a truly predictive simulation of erosion. Furthermore, such a technique would enhance our understanding of debris flows, gas or fluid driven terrestrial erosion, and industrial processes involving porous media.

The proposed approach in chapter 5 involved combining SPH with a viscoplastic constitutive law. SPH is well-suited for the problem described above because it provides precise interface definition and allows one to calculate ballistic soil trajectories. Eulerian techniques do not provide this precise interface definition or the ballistic soil trajectories needed to predict the potentially hazardous motion of eroded soil.

Currently, we have implemented a two-phase saturated porous media formulation in SPH. We have provided porosity-based switches for drag between phases that permit one to model the Darcy-like flow regime characteristic of low porosity states and the dusty-gas flow regime characteristic of high porosity states (see [144, 145]). Combining these capabilities in a single computational domain will allow us to perform predictive simulations of gas-driven soil erosion in the future.

A qualitative example of predicting gas-driven soil erosion is provided in Fig. 6.2. This figure depicts a jet of gas impinging on a sandy surface. The domain is 0.5 m wide in the x dimension and 0.1 m thick in the y dimension (into the page). Periodic boundary conditions are used in the x and y dimensions. The sand has density $\rho_0 = 1600$ kg/m^3 (using the conventions of chapter 5), and the gas is modeled as ideal with a viscosity of 10 μPa·s. The frictional strength of the granular material is a constant $\mu = 0.8$, permeability is 2×10^{-10} m^2, and gravity is set to 3.711 m/s^2. The soil layer is approximately 0.25 m thick in the z dimension, sitting above an

impermeable solid substrate (i.e. fixed SPH particles). The gas is driven at 100 m/s downward and the switch between Darcy drag and dusty-gas drag is at a porosity of 0.38.

The images in the left column of Fig. 6.2 illustrate the sand response only in the first 75 ms following the gas impingement event. The images in the right column illustrate the gas response only. At early times, rapid diffusion of the gas into the granular medium results in a high-pressure region beneath the impingement zone. This high-pressure region is diminished as gas diffuses deeper into the sand. During this diminishing process, a crater begins to form on the surface of the granular material due to the high-pressure bulb of gas forcing the granular medium upward. At later times, the sand crater is seen further developing, with sand mass accelerating outward and upward as it is entrained in the background dusty-gas flow.

Future work at the continuum scale will also address modeling other porous materials using the SPH framework described above and in chapter 5. Adding the appropriate balance and constitutive laws will allow us to address a wide range of problems involving large deformation and flow of materials. Some examples include post-fracture flow of brittle ceramics and comminution of brittle rocks.

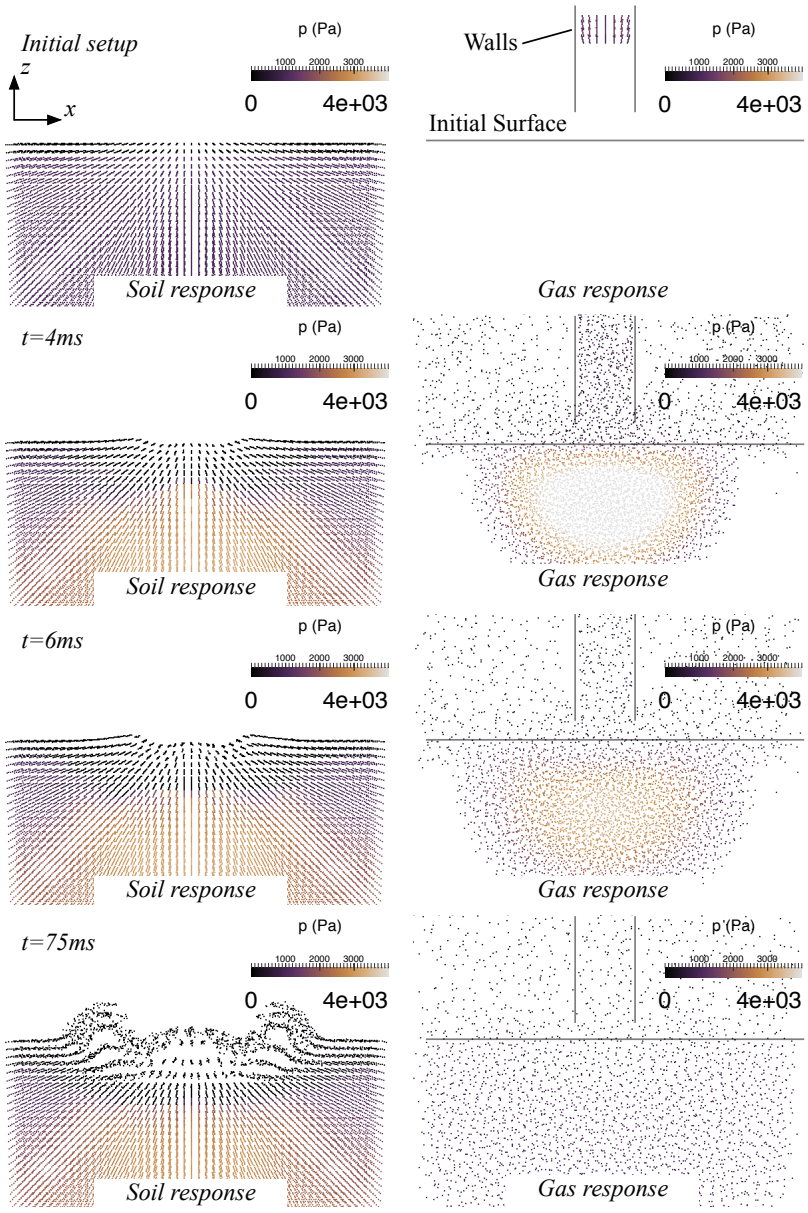

Figure 6.2: Qualitative example of gas-driven soil erosion modeled using the SPH framework. The left column of figures illustrates the sand response only in the first 75 ms of the gas impingement event. The right column of images illustrates the gas response only.

Bibliography

[1] E. Azéma and F. Radjaï, "Internal structure of inertial granular flows," *Physical Review Letters*, vol. 112, no. 7, p. 078001, 2014.

[2] Y. Forterre and O. Pouliquen, "Flows of dense granular media," *Annual Review of Fluid Mechanics*, vol. 40, pp. 1–24, 2008.

[3] S. Savage and M. Sayed, "Stresses developed by dry cohesionless granular materials sheared in an annular shear cell," *Journal of Fluid Mechanics*, vol. 142, pp. 391–430, 1984.

[4] P. Jop, F. Yoel, and O. Pouliquen, "A constitutive law for dense granular flows," *Nature*, vol. 441, pp. 727–730, 2006.

[5] N. Balmforth and R. Kerswell, "Granular collapse in two dimensions," *Journal of Fluid Mechanics*, vol. 538, pp. 399–428, 2005.

[6] A. Mangeney, O. Roche, O. Hungr, N. Mangold, G. Faccanoni, and A. Lucas, "Erosion and mobility in granular collapse over sloping beds," *Journal of Geophysical Research: Earth Surface (2003–2012)*, vol. 115, no. F3, 2010.

[7] P. G. de Gennes, "Granular matter: a tentative view," *Reviews of Modern Physics*, vol. 71, pp. S374–S382, Mar 1999.

[8] H. M. Jaeger, S. R. Nagel, and R. P. Behringer, "Granular solids, liquids, and gases," *Reviews of Modern Physics*, vol. 68, no. 4, p. 1259, 1996.

[9] I. S. Aranson and L. S. Tsimring, "Patterns and collective behavior in granular media: Theoretical concepts," *Reviews of Modern Physics*, vol. 78, no. 2, p. 641, 2006.

[10] R. C. Hurley and J. E. Andrade, "Friction in inertial granular flows: competition between dilation and grain-scale dissipation rates," *Granular Matter*, vol. 17, no. 3, pp. 287–295, 2015.

[11] F. da Cruz, S. Emam, M. Prochnow, J.-N. Roux, and F. Chevoir, "Rheophysics of dense granular materials: Discrete simulation of plane shear flows," *Physical Review E*, vol. 72, no. 2, p. 021309, 2005.

[12] L. Rothenburg and R. J. Bathurst, "Analytical study of induced anistropy in idealized granular materials," *Géotechnique*, vol. 39, no. 4, pp. 601–614, 1989.

[13] R. Hurley, E. Marteau, G. Ravichandran, and J. E. Andrade, "Extracting inter-particle forces in opaque granular materials: Beyond photoelasticity," *Journal of the Mechanics and Physics of Solids*, vol. 63, pp. 154–166, 2014.

[14] R. Hurley, K. Lim, G. Ravichandran, and J. Andrade, "Dynamic inter-particle force inference in granular materials: Method and application," *Experimental Mechanics*, 2015.

[15] R. C. Hurley and J. E. Andrade, "Strength of granular materials in transient and steady state rapid shear," *Procedia Engineering*, vol. 103, pp. 237–245, 2015.

[16] M. Oda, "Initial fabrics and their relations to mechanical properties of granular material," *Soils and Foundations*, vol. 12, no. 1, pp. 17–36, 1972.

[17] J. Christoffersen, M. M. Mehrabadi, and S. Nemat-Nasser, "A micromechanical description of granular material behavior," *Journal of Applied Mechanics*, vol. 48, no. 2, pp. 339–344, 1981.

[18] R. J. Bathurst and L. Rothenburg, "Observations on stress-force-fabric relationships in idealized granular materials," *Mechanics of Materials*, vol. 9, no. 1, pp. 65–80, 1990.

[19] M. E. Cates, J. P. Wittmer, J.-P. Bouchaud, and P. Claudin, "Jamming, force chains, and fragile matter," *Physical Review Letters*, vol. 81, pp. 1841–1844, Aug 1998.

[20] J. F. Peters, M. Muthuswamy, J. Wibowo, and A. Tordesillas, "Characterization of force chains in granular material," *Physical Review E.*, vol. 72, p. 041307, Oct 2005.

[21] T. S. Majmudar and R. P. Behringer, "Contact force measurements and stress-induced anisotropy in granular materials," *Nature*, vol. 435, pp. 1079–1082, 06 2005.

[22] S. N. Coppersmith, C. h. Liu, S. Majumdar, O. Narayan, and T. A. Witten, "Model for force fluctuations in bead packs," *Physical Review E.*, vol. 53, pp. 4673–4685, 1996.

[23] N. Guo and J. Zhao, "The signature of shear-induced anisotropy in granular media," *Computers and Geotechnics*, vol. 47, no. 0, pp. 1 – 15, 2013.

[24] C.-h. Liu, S. R. Nagel, D. A. Schecter, S. N. Coppersmith, S. Majumdar, O. Narayan, and T. A. Witten, "Force fluctuations in bead packs," *Science*, vol. 269, no. 5223, pp. 513–515, 1995.

[25] S. Ostojic, E. Somfai, and B. Nienhuis, "Scale invariance and universality of force networks in static granular matter," *Nature*, vol. 439, pp. 828–830, 02 2006.

[26] F. Radjai, M. Jean, J. J. Moreau, and S. Roux, "Force distributions in dense two-dimensional granular systems," *Physical Review Letters*, vol. 77, pp. 274–277, Jul 1996.

[27] F. Radjai, D. E. Wolf, M. Jean, and J. J. Moreau, "Bimodal character of stress transmission in granular packings," *Physical Review Letters*, vol. 80, no. 1, pp. 61–64, 1998.

[28] M. Satake, "Fabric tensor in granular materials," in *Deformation and Failure of Granular Materials* (P. Vermeer and H. J. Luger, eds.), pp. 63–68, 1982.

[29] P. Claudin, J.-P. Bouchaud, M. E. Cates, and J. P. Wittmer, "Models of stress fluctuations in granular media," *Physical Review E.*, vol. 57, pp. 4441–4457, Apr 1998.

[30] J.-P. Bouchaud, P. Claudin, D. Levine, and M. Otto, "Force chain splitting in granular materials: A mechanism for large-scale pseudo-elastic behaviour," *The European Physical Journal E*, vol. 4, no. 4, pp. 451–457, 2001.

[31] D. M. Mueth, H. M. Jaeger, and S. R. Nagel, "Force distribution in a granular medium," *Physical Review E*, vol. 57, no. 3, p. 3164, 1998.

[32] M. P. Ciamarra, A. H. Lara, A. T. Lee, D. I. Goldman, I. Vishik, and H. L. Swinney, "Dynamics of drag and force distributions for projectile impact in a granular medium," *Physical Review Letters*, vol. 92, no. 19, p. 194301, 2004.

[33] P. A. Cundall and O. D. L. Strack, "A discrete numerical model for granular assemblies," *Géotechnique*, vol. 29, no. 1, pp. 47–65, 1979.

[34] M. Jean, "The non-smooth contact dynamics method," *Computer Methods in Applied Mechanics and Engineering*, vol. 177, no. 3, pp. 235–257, 1999.

[35] J. J. Moreau, "Unilateral contact and dry friction in finite freedom dynamics," in *Nonsmooth Mechanics and Applications*, pp. 1–82, Springer, 1988.

[36] A. Taboada, K.-J. Chang, F. Radjaï, and F. Bouchette, "Rheology, force transmission, and shear instabilities in frictional granular media from biaxial numerical tests using the contact dynamics method," *Journal of Geophysical Research: Solid Earth (1978–2012)*, vol. 110, no. B9, 2005.

[37] E. Azéma, F. Radjai, R. Peyroux, and G. Saussine, "Force transmission in a packing of pentagonal particles," *Physical Review E*, vol. 76, no. 1, p. 011301, 2007.

[38] X. Garcia, J.-P. Latham, J. Xiang, and J. Harrison, "A clustered overlapping sphere algorithm to represent real particles in discrete element modelling," *Geotechnique*, vol. 59, no. 9, pp. 779–784, 2009.

[39] A. A. Peña, P. G. Lind, and H. J. Herrmann, "Modeling slow deformation of polygonal particles using dem," *Particuology*, vol. 6, no. 6, pp. 506–514, 2008.

[40] A. Drescher and G. de Josselin de Jong, "Photoelastic verification of a mechanical model for the flow of a granular material," *Journal of Mechanics and Physics of Solids*, vol. 20, pp. 337–340, 1972.

[41] D. Howell, R. P. Behringer, and C. Veje, "Stress fluctuations in a 2d granular couette experiment: A continuous transition," *Physical Review Letters*, vol. 82, pp. 5241–5244, Jun 1999.

[42] A. H. Clark, L. Kondic, and R. P. Behringer, "Particle scale dynamics in granular impact," *Physical Review Letters*, vol. 109, p. 238302, Dec 2012.

[43] A. H. Clark, A. J. Petersen, and R. P. Behringer, "Collisional model for granular impact dynamics," *Physical Review E*, vol. 89, no. 1, p. 012201, 2014.

[44] A. Shukla, M. H. Sadd, R. Singh, Q. Tai, and S. Vishwanathan, "Role of particle shape and contact profile on the dynamic response of particulate materials," *Optics and Lasers in Engineering*, vol. 19, no. 1, pp. 99–119, 1993.

[45] J. Zhou, S. Long, Q. Wang, and A. D. Dinsmore, "Measurement of forces inside a three-dimensional pile of frictionless droplets," *Science*, vol. 312, no. 5780, pp. 1631–1633, 2006.

[46] M. Saadatfar, A. P. Sheppard, T. J. Senden, and A. J. Kabla, "Mapping forces in a 3d elastic assembly of grains," *Journal of the Mechanics and Physics of Solids*, vol. 60, no. 1, pp. 55 – 66, 2012.

[47] N. Brodu, J. A. Dijksman, and R. P. Behringer, "Spanning the scales of granular materials through microscopic force imaging," *Nature Communications*, vol. 6, 2015.

[48] J. Andrade and C. Avila, "Granular element method (gem): linking inter-particle forces with macroscopic loading," *Granular Matter*, vol. 14, pp. 51–61, 2012.

[49] S. Hall, J. Wright, T. Pirling, E. Andò, D. Hughes, and G. Viggiani, "Can intergranular force transmission be identified in sand?," *Granular Matter*, vol. 13, pp. 251–254, 2011.

[50] R. V. Martins, L. Margulies, S. Schmidt, H. F. Poulsen, and T. Leffers, "Simultaneous measurement of the strain tensor of 10 individual grains embedded in an al tensile sample," *Materials Science and Engineering: A*, vol. 387–389, no. 0, pp. 84 – 88, 2004.

[51] H. F. Poulsen, X. Fu, E. Knudsen, E. M. Lauridsen, K. Margulies, and S. Schmidt, "3dxrd - mapping grains and their dynamics in 3 dimensions," *Materials Science Forum*, vol. Recrystallization and Grain Growth, pp. 1363–1372, 2004.

[52] K. A. Alshibli and A. H. Reed, *Applications of X-ray Microtomography to Geomaterials*. Wiley-ISTE, 1st ed., 2010.

[53] J. Desrues, G. Viggiani, and P. Bésuelle, eds., *Advances in X-ray Tomography for Geomaterials*. Wiley-ISTE, 2006.

[54] J. Y. Wang, L. Park and Y. Fu, "Representation of real particles for dem simulation using x-ray tomography," *Construction and Building Materials*, vol. 21, no. 2, pp. 338–346, 2007.

[55] M. A. Sutton, J. J. Orteu, and H. Schreier, *Image Correlation for Shape, Motion and Deformation Measurements: Basic concepts, theory and applications*. Springer, 2009.

[56] I. Vlahinic, E. Andò, G. Viggiani, and J. E. Andrade, "Towards a more accurate characterization of granular media: extracting quantitative descriptors from grain-scale images," *Granular Matter*, 2012. Under review.

[57] Correlated Solutions, *Vic-2D, Reference Manual*.

[58] Correlated Solutions, *Vic-2D, Testing Guide*.

[59] B. Pan, K. Qian, H. Xie, and A. Asundi, "Two-dimensional digital image correlation for in-plane displacement and strain measurement: a review," *Measurement Science and Technology*, vol. 20, no. 6, p. 062001, 2009.

[60] D. H. Ballard, "Generalizing the Hough transform to detect arbitrary shapes," *Pattern Recognition*, vol. 13, pp. 111–122, Jan. 1981.

[61] T. Peng, "Detect circles with various radii in grayscale image via hough transform." http://www.mathworks.com/matlabcentral/fileexchange, 2010.

[62] M. Kass, A. Witkin, and D. Terzopoulos, "Snakes: Active contour models," *International Journal of Computer Vision*, vol. 1, pp. 321–331, Jan. 1988.

[63] D.-J. Kroon, "Snake: Active contour." http://www.mathworks.com/matlabcentral/fileexchan
2011.

[64] J. C. Santamarina, K. A. Klein, and M. A. Fam, *Soils and Waves*. J. Wiley & Sons, 2001.

[65] M. Bornert, F. Brémand, P. Doumalin, J.-C. Dupré, M. Fazzini, M. Grédiac, F. Hild, S. Mistou, J. Molimard, J.-J. Orteu, L. Robert, Y. Surrel, P. Vacher, and B. Wattrisse, "Assessment of digital image correlation measurement errors: Methodology and results," *Experimental Mechanics*, vol. 49, pp. 353–370, 2009.

[66] P. Lötstedt, "Perturbation bounds for the linear least squares problem subject to linear inequality constraints," *BIT Numerical Mathematics*, vol. 23, pp. 500–519, 1983.

[67] C. Hansen, *Rank-Deficient and Discrete Ill-Posed Problems*. Society for Industrial and Applied Mathematics, 1995.

[68] V. C. R., *Computational Methods for Inverse Problems*. Society for Industrial and Applied Mathematics, 2002.

[69] F. Bauer and M. A. Lukas, "Comparing parameter choice methods for regularization of ill-posed problems," *Mathematics and Computers in Simulation*, vol. 81, no. 9, pp. 1795 – 1841, 2011.

[70] J. F. Sturm, "Using sedumi 1.02, a MATLAB toolbox for optimization over symmetric cones," *Optimization Methods and Software*, vol. 11–12, pp. 625–653, 1999.

[71] M. Grant and S. Boyd, "CVX: Matlab software for disciplined convex programming, version 1.21," Apr. 2011.

[72] J. Lofberg, "Yalmip : a toolbox for modeling and optimization in matlab," in *Computer Aided Control Systems Design, 2004 IEEE International Symposium on*, pp. 284 –289, 2004.

[73] J. Oddershede, S. Schmidt, H. F. Poulsen, H. O. Sørensen, J. Wright, and W. Reimers, "Determining grain resolved stresses in polycrystalline materials using three-dimensional X-ray diffraction," *Journal of Applied Crystallography*, vol. 43, pp. 539–549, Jun 2010.

[74] S. Boyd and L. Vandenberghe, *Convex Optimization*. New York, NY, USA: Cambridge University Press, 2004.

[75] *Abaqus, Version 6.11*. D S Simulia, Dassault Systèmes.

[76] M. Bornert, F. Brémand, P. Doumalin, J.-C. Dupré, M. Fazzini, M. Grédiac, F. Hild, S. Mistou, J. Molimard, J.-J. Orteu, *et al.*, "Assessment of digital image correlation measurement errors: methodology and results," *Experimental Mechanics*, vol. 49, no. 3, pp. 353–370, 2009.

[77] MATLAB, *version 8.1.0 (R2013a)*. Natick, Massachusetts: The MathWorks Inc., 2013.

[78] E. R. Davies, *Machine vision: theory, algorithms, practicalities*. Elsevier, 2004.

[79] T. J. Atherton and D. J. Kerbyson, "Size invariant circle detection," *Image and Vision Computing*, vol. 17, no. 11, pp. 795–803, 1999.

[80] S. Coppersmith, C.-h. Liu, S. Majumdar, O. Narayan, and T. Witten, "Model for force fluctuations in bead packs," *Physical Review E*, vol. 53, no. 5, p. 4673, 1996.

[81] S. A. Hall and J. Wright, "Characterisation of 3d force transmission in real granular media." Presented at the International Conference on Experimental Mechanics, July 2014.

[82] S. Dwivedi, R. Teeter, C. Felice, and Y. Gupta, "Two dimensional mesoscale simulations of projectile instability during penetration in dry sand," *Journal of Applied Physics*, vol. 104, no. 8, pp. 083502–083502, 2008.

[83] L. Tsimring and D. Volfson, "Modeling of impact cratering in granular media," in *Powders and Grains 2005* (R. Garca-Rojo, H. J. Herrmann, and S. McNamara, eds.), vol. 2, pp. 1215–1223, A. A. Balkema, Rotterdam, 2005.

[84] H. M. Jaeger and S. R. Nagel, "Physics of the granular state," *Science*, vol. 255, no. 5051, pp. 1523–1531, 1992.

[85] D. M. Wood, *Soil behaviour and critical state soil mechanics*. Cambridge university press, 1990.

[86] C. S. Campbell, "Rapid granular flows," *Annual Review of Fluid Mechanics*, vol. 22, no. 1, pp. 57–90, 1990.

[87] I. Goldhirsch, "Rapid granular flows," *Annual Review of Fluid Mechanics*, vol. 35, no. 1, pp. 267–293, 2003.

[88] G. MiDi, "On dense granular flows," *The European Physical Journal E*, vol. 14, no. 4, pp. 341–365, 2004.

[89] M. Jutzi and E. Asphaug, "Forming the lunar farside highlands by accretion of a companion moon," *Nature*, vol. 476, no. 7358, pp. 69–72, 2011.

[90] K. Kamrin and G. Koval, "Nonlocal constitutive relation for steady granular flow," *Physical Review Letters*, vol. 108, no. 17, p. 178301, 2012.

[91] M. Tankeo, P. Richard, and C. Édouard, "Analytical solution of the μ(i)-rheology for fully developed granular flows in simple configurations," *Granular Matter*, vol. 15, no. 6, pp. 881–891, 2013.

[92] L. Rothenburg and R. J. Bathurst, "Analytical study of induced anistropy in idealized granular materials," *Géotechnique*, vol. 4, no. 1, pp. 601–614, 1989.

[93] T. Hatano and O. Kuwano, "Origin of the velocity-strengthening nature of granular friction," *Pure and Applied Geophysics*, vol. 170, no. 1-2, pp. 3–11, 2013.

[94] J. T. Jenkins, "Dense inclined flows of inelastic spheres," *Granular Matter*, vol. 10, no. 1, pp. 47–52, 2007.

[95] Q. Sun, F. Jin, and G. G. Zhou, "Energy characteristics of simple shear granular flows," *Granular Matter*, vol. 15, no. 1, pp. 119–128, 2013.

[96] M. Babic, H. H. Shen, and H. T. Shen, "The stress tensor in granular shear flows of uniform, deformable disks at high solids concentrations," *Journal of Fluid Mechanics*, vol. 219, no. 10, pp. 81–118, 1990.

[97] S. Plimpton, "Lammps."

[98] S. Plimpton, "Fast parallel algorithms for short-range molecular dynamics," *Journal of Computational Physics*, vol. 117, no. 1, pp. 1–19, 1995.

[99] H. Zhang and H. Makse, "Jamming transition in emulsions and granular materials," *Physical Review E*, vol. 72, no. 1, p. 011301, 2005.

[100] A. D. Renzo and F. P. D. Maio, "Comparison of contact-force models for the simulation of collisions in dem-based granular flow codes," *Chemical Engineering Science*, vol. 59, no. 3, pp. 525–541, 2004.

[101] F. G. Bridges, A. Hatzes, and D. N. C. Lin, "Structure, stability and evolution of saturn's rings," *Nature*, vol. 309, pp. 333–335, 1984.

[102] N. V. Brilliantov, F. Spahn, J.-M. Hertzsch, and T. Pöschel, "Model for collisions in granular gases," *Physical Review E*, vol. 53, no. 5, p. 5382, 1996.

[103] K. Senetakis, M. R. Coop, and M. C. Todisco, "The inter-particle coefficient of friction at the contacts of leighton buzzard sand quartz minerals," *Soils and Foundations*, vol. 53, no. 5, pp. 746–755, 2013.

[104] K. Bagi, "Stress and strain in granular assemblies," *Mechanics of Materials*, vol. 22, no. 3, pp. 165–177, 1996.

[105] R. A. Bagnold, "Experiments on a gravity-free dispersion of large solid spheres in a newtonian fluid under shear," in *Proceedings of the Royal Society of London A: Mathematical, Physical and Engineering Sciences*, vol. 225, pp. 49–63, The Royal Society, 1954.

[106] O. Pouliquen and Y. Forterre, "Friction law for dense granular flows: application to the motion of a mass down a rough inclined plane," *Journal of Fluid Mechanics*, vol. 453, pp. 133–151, 2002.

[107] J. E. Andrade, Q. Chen, P. H. Le, C. F. Avila, and T. M. Evans, "On the rheology of dilative granular media: Bridging solid-and fluid-like behavior,"

Journal of the Mechanics and Physics of Solids, vol. 60, no. 6, pp. 1122–1136, 2012.

[108] L. Lacaze and R. R. Kerswell, "Axisymmetric granular collapse: a transient 3d flow test of viscoplasticity," *Physical Review Letters*, vol. 102, no. 10, p. 108305, 2009.

[109] A. Lucas, A. Mangeney, and J. P. Ampuero, "Frictional velocity-weakening in landslides on earth and on other planetary bodies," *Nature Communications*, vol. 5, 2014.

[110] J. E. Andrade and R. I. Borja, "Capturing strain localization in dense sands with random density," *International Journal for Numerical Methods in Engineering*, vol. 67, no. 11, pp. 1531–1564, 2006.

[111] I. R. Ionescu, A. Mangeney, F. Bouchut, and O. Roche, "Viscoplastic modeling of granular column collapse with pressure-dependent rheology," *Journal of Non-Newtonian Fluid Mechanics*, vol. 219, pp. 1–18, 2015.

[112] C. M. Mast, P. Arduino, P. Mackenzie-Helnwein, and G. R. Miller, "Simulating granular column collapse using the material point method," *Acta Geotechnica*, vol. 10, no. 1, pp. 101–116, 2014.

[113] H. H. Bui, R. Fukagawa, K. Sako, and S. Ohno, "Lagrangian meshfree particles method (sph) for large deformation and failure flows of geomaterial using elastic-plastic soil constitutive model," *International Journal for Numerical and Analytical Methods in Geomechanics*, vol. 32, no. 12, p. 1537, 2008.

[114] W. Chen and T. Qiu, "Numerical simulations for large deformation of granular materials using smoothed particle hydrodynamics method," *International Journal of Geomechanics*, vol. 12, no. 2, pp. 127–135, 2011.

[115] H. P. Zhang and H. A. Makse, "Jamming transition in emulsions and granular materials," *Physical Review E*, vol. 72, p. 011301, Jul 2005.

[116] D. W. Taylor, "Fundamentals of soil mechanics.," *Soil Science*, vol. 66, no. 2, p. 161, 1948.

[117] J. J. Monaghan, "Smoothed particle hydrodynamics," *Reports on progress in physics*, vol. 68, no. 8, p. 1703, 2005.

[118] G.-R. Liu and M. B. Liu, *Smoothed particle hydrodynamics: a meshfree particle method*. World Scientific, 2003.

[119] M. Liu and G. Liu, "Smoothed particle hydrodynamics (sph): an overview and recent developments," *Archives of Computational Methods in Engineering*, vol. 17, no. 1, pp. 25–76, 2010.

[120] J. J. Monaghan and J. C. Lattanzio, "A refined particle method for astrophysical problems," *Astronomy and Astrophysics*, vol. 149, pp. 135–143, 1985.

[121] J. P. Morris, P. J. Fox, and Y. Zhu, "Modeling low reynolds number incompressible flows using sph," *Journal of Computational Physics*, vol. 136, no. 1, pp. 214–226, 1997.

[122] D. J. Price and J. Monaghan, "Smoothed particle magnetohydrodynamics–ii. variational principles and variable smoothing-length terms," *Monthly Notices of the Royal Astronomical Society*, vol. 348, no. 1, pp. 139–152, 2004.

[123] J. J. Monaghan, "Smoothed particle hydrodynamics," *Annual Review of Astronomy and Astrophysics*, vol. 30, pp. 543–574, 1992.

[124] J. J. Monaghan, "Simulating free surface flows with sph," *Journal of Computational Physics*, vol. 110, no. 2, pp. 399–406, 1994.

[125] J. E. Andrade and X. Tu, "Multiscale framework for behavior prediction in granular media," *Mechanics of Materials*, vol. 41, no. 6, pp. 652–669, 2009.

[126] P. Randles and L. Libersky, "Smoothed particle hydrodynamics: some recent improvements and applications," *Computer Methods in Applied Mechanics and Engineering*, vol. 139, no. 1, pp. 375–408, 1996.

[127] J. Monaghan, "On the problem of penetration in particle methods," *Journal of Computational physics*, vol. 82, no. 1, pp. 1–15, 1989.

[128] K. Terzaghi, *Theoretical soil mechanics*. Wiley, 1943.

[129] O. Pouliquen and Y. Forterre, "A non-local rheology for dense granular flows," *Philosophical Transactions of the Royal Society of London A: Mathematical, Physical and Engineering Sciences*, vol. 367, no. 1909, pp. 5091–5107, 2009.

[130] L. E. Silbert, D. Ertaş, G. S. Grest, T. C. Halsey, D. Levine, and S. J. Plimpton, "Granular flow down an inclined plane: Bagnold scaling and rheology," *Physical Review E*, vol. 64, no. 5, p. 051302, 2001.

[131] G. Lube, H. E. Huppert, R. S. J. Sparks, and M. A. Hallworth, "Axisymmetric collapses of granular columns," *Journal of Fluid Mechanics*, vol. 508, pp. 175–199, 2004.

[132] G. Lube, H. E. Huppert, R. S. J. Sparks, and A. Freundt, "Collapses of two-dimensional granular columns," *Physical Review E*, vol. 72, no. 4, p. 041301, 2005.

[133] R. Kerswell, "Dam break with coulomb friction: A model for granular slumping?," *Physics of Fluids (1994-present)*, vol. 17, no. 5, p. 057101, 2005.

[134] L. Staron and E. Hinch, "Study of the collapse of granular columns using two-dimensional discrete-grain simulation," *Journal of Fluid Mechanics*, vol. 545, pp. 1–27, 2005.

[135] P.-Y. Lagrée, L. Staron, and S. Popinet, "The granular column collapse as a continuum: validity of a two-dimensional navier–stokes model with a μ (i)-rheology," *Journal of Fluid Mechanics*, vol. 686, pp. 378–408, 2011.

[136] M. Farin, A. Mangeney, and O. Roche, "Fundamental changes of granular flow dynamics, deposition, and erosion processes at high slope angles: Insights

from laboratory experiments," *Journal of Geophysical Research: Earth Surface*, vol. 119, no. 3, pp. 504–532, 2014.

[137] P. Jop, Y. Forterre, and O. Pouliquen, "Crucial role of sidewalls in granular surface flows: consequences for the rheology," *Journal of Fluid Mechanics*, vol. 541, pp. 167–192, 2005.

[138] J. J. Monaghan, "Sph without a tensile instability," *Journal of Computational Physics*, vol. 159, no. 2, pp. 290–311, 2000.

[139] R. M. Iverson, "The physics of debris flows," *Reviews of Geophysics*, vol. 35, no. 3, pp. 245–296, 1997.

[140] H.-Y. Ko and R. Scott, "Transient rocket-engine gas flow in soil.," *AIAA Journal*, vol. 6, no. 2, pp. 258–264, 1968.

[141] L. Roberts, "The interaction of a rocket exhaust with the lunar surface.," 1966.

[142] P. T. Metzger, J. E. Lane, and C. D. Immer, "Modification of roberts' theory for rocket exhaust plumes eroding lunar soil," *Earth and Space*, pp. 1–8, 2008.

[143] P. T. Metzger, J. Smith, and J. E. Lane, "Phenomenology of soil erosion due to rocket exhaust on the moon and the mauna kea lunar test site," *Journal of Geophysical Research: Planets (1991–2012)*, vol. 116, no. E6, 2011.

[144] O. C. Zienkiewicz, A. Chan, M. Pastor, B. Schrefler, and T. Shiomi, *Computational geomechanics*. Wiley Chichester, 1999.

[145] G. Laibe and D. J. Price, "Dusty gas with smoothed particle hydrodynamics–i. algorithm and test suite," *Monthly Notices of the Royal Astronomical Society*, vol. 420, no. 3, pp. 2345–2364, 2012.